PREDICTING FLOW PROPERTIES USING GEOPHYSICAL DATA: IMPROVING AQUIFER CHARACTERIZATION

A DISSERTATION

SUBMITTED TO THE DEPARTMENT OF GEOPHYSICS

AND THE COMMITTEE ON GRADUATE STUDIES

OF STANFORD UNIVERSITY

IN PARTIAL FULFILLMENT OF THE REQUIREMENTS FOR THE DEGREE OF

DOCTOR OF PHILOSOPHY

Wendy Lynn Wempe

June, 2000

© Copyright 2000
by Wendy Lynn Wempe
All Rights Reserved

Abstract

Protecting ground water from permanent depletion and potential contamination has become a priority in the U.S. According to the 1999 Safe Drinking Water Act[1], "In 1994, the National Academy of Sciences[2] estimated that over a trillion dollars, or approximately $4,000 per person in the U.S., will be spent in the next thirty years on clean-up of contaminated soil and ground water". Other significant statistics are: "Ninety-six percent of all fresh water on earth is ground water[3]" and "About 77.5 billion gallons of ground water are withdrawn daily for use in this country". In order to protect fresh ground water and to clean up contaminated ground water, first, aquifer systems need to be characterized, then, ground water flow modeled.

The objective of this research has been to improve aquifer characterization. This objective was met by focusing on using rock physics theory and geophysical data to predict flow properties, such as porosity, permeability and clay content. The advantage of using geophysical data to predict these properties stems from the fact that geophysical data are less expensive and more spatially-abundant than lab- or field-measured, flow-property data. This research contributes three newly-developed relationships that significantly improve aquifer characterization: (1) a general relationship between total and channel porosities, (2) a general relationship between electrical resistivity and channel porosity, and (3) bounds on the electrical resistivity – seismic velocity relationship. Even though the objectives of this research have been environmentally

---

[1] U.S. Environmental Protection Agency, 1999. *Safe Drinking Water Act, Section 1429*, *Ground Water Report to Congress*. Office of Water, Washington, D.C. EPA 816-R-99-016

[2] National Research Council, 1994. *Alternatives for Ground Water Cleanup*. Committee on Ground Water Cleanup Alternatives, Water Science and Technology Board, Commission on Geoscience, Environment, and Resources, National Research Coucil. National Academy Press, Washington, D.C.

[3] U.S. Environmental Protection Agency, 1998. *National Water Quality Inventory: 1996 Report to Congress, Ground Water Chapters*. Office of Water, Washington, D.C., EPA 816-R-98-011.

focused, the resulting developments can also be used to significantly improve petroleum reservoir characterization.

The objective of aquifer characterization is to create hydrogeologic maps of the geometries of aquifers and aquitards and their flow properties, such as porosity and permeability. Without characteristic hydrogeologic maps, hydraulic flow and contaminant transport cannot be accurately modeled. Historically, hydrogeologic maps have been created by *qualitatively* interpolating flow properties between wells using hydraulic, chemistry and lithologic well data. However, over the past few decades, geostatistical techniques and geophysical data have been used in addition to traditional data analysis techniques to *quantitatively* interpolate flow properties throughout the well columns and away from wells where data do not exist. These innovative techniques have proven to be more cost-efficient and less subjective than traditional ones.

As you will see, this research is all focused on my interest in developing better techniques for characterizing aquifer environments, a much-needed area of research. In a sense, the sequence of the following chapters tells the story of how my interests and research progressed from characterizing aquifers using techniques from the petroleum industry, to developing new techniques for predicting porosity. Chapters 1 and 2 discuss case studies where petroleum-developed tools were used to solve groundwater problems, whereas Chapters 3, 4 and 5 discuss new, physically- and theoretically-based developments for constraining porosity estimates using resistivity and seismic data. These developments are not only new and applicable to groundwater investigations, but also to petroleum-related investigations.

My research began by tackling a common, yet extremely complex, problem of developing a 3-D model of aquifers and aquitards so that the complex heterogeneity of the fluvial aquifer system could be incorporated in flow modeling. Because of the complexity of the fluvial depositional environment, traditional mapping techniques proved to be inadequate for characterizing the aquifer system. The *exact* geometry of such systems is nearly impossible to characterize with 1-D data, regardless of the

mapping technique. I chose to work on this project not only because of its complexity, but also because the dataset available at the site represented the most common data collected for large-scale groundwater investigation projects: water chemistry data, lithologic descriptions from drill cuttings, gamma-ray logs and resistivity logs. Working closely with Komex International, the environmental company hired to characterize the aquifer system and model contaminant transport, proved to be invaluable for gaining insight into some of the practical problems encountered during environmental investigation. Chapter 1 outlines the steps used to three-dimensionally characterize the complexity of a fluvial aquifer system. I used indicator geostatistics to interpolate between well log interpretations of sand aquifers and clay aquitards. These interpretations were made by hand-picking sand and clay units using 90 gamma-ray, resistivity and lithologic logs, a laborious yet necessary step in defining the geometries of the aquifers and aquitards. By working on this project, I gained an appreciation for the need for more efficient and comprehensive use of available data for site characterization. Perhaps the most significant contribution of this work is the final transcript itself, which was written as a tutorial that earth scientists could follow to solve similar 3-D characterization problems.

The work outlined in Chapter 2 is based upon the need for more quantitative approaches for interpreting gamma-ray and resistivity logs, the most commonly-collected geophysical data available for large-scale groundwater investigation problems. The site for investigation was the Oak Ridges Moraine (ORM), the largest groundwater source for Canada. The overall objective of work on the ORM by the Geological Survey of Canada (GSC) was to map the geometries and flow properties of regional aquifers and aquitards. However, the part of the puzzle that I was interested in solving was figuring out how to quantitatively interpret the geophysical data. Like in the first chapter, I borrowed tools from the petroleum industry to accomplish this, but unlike the first site, core was available in the ORM. My approach was to measure the clay content and porosity in several dozen core samples and use the measurements to develop empirical relationships

between (1) gamma-ray values and clay volume and (2) resistivity and porosity and clay volume. These relationships served as a means for identifying aquifers and aquitards and predicting clay volume, porosity and permeability throughout the well columns where core measurements were not made. By working on this project, I gained an appreciation for the need for more theoretical and less empirical methods for interpreting flow properties using geophysical data. The most significant contributions of this work are (1) the empirical relationships between geophysical data and flow properties in shallow, unconsolidated sediments, and (2) like the first chapter, the final transcript itself, which was written as a tutorial that earth scientists could use to solve similar problems.

Chapter 3, like Chapters 4 and 5, discuss new developments for constraining porosity estimates. In particular, this chapter focuses on developing the relationship between channel and total porosities and discussing how porosity is defined physically, hydraulically, electrically and seismically. Channel porosity is the fraction of the total pore volume fraction of a composite that is available for hydraulic and electrical flow. The total porosity is the total pore volume fraction of a composite; a controlling factor for the response of seismic waves. It turns out that a composite's channel porosity can be related to its total porosity by its porous percolation threshold, critical porosity, and a pore space parameter. The percolation threshold and critical porosity define three distinct porosity regions physically, hydraulically, electrically and seismically. Region I is defined for porosities less than the porous percolation threshold, Region II is defined for porosities between the porous percolation threshold and critical porosity, and Region III is defined for porosities greater than the critical porosity. The channel porosity – total porosity relationship is valuable for converting from channel to total porosity or vise versa when (1) comparing lab-measured and estimated porosities with hydraulic permeability, formation resistivity factor, or seismic velocity data, and (2) relating seismic velocity data to resistivity or permeability data. The most significant contributions of this work are (1) the development of the total porosity – channel porosity relationship, and (2) insight into the relationships between channel porosity and

formation factor and between channel porosity and permeability. Topics in this chapter provide background for the following two chapters on electrical resistivity and seismic velocity.

Chapter 4 focuses on theoretically and empirically exploring the influence of a composite's pore space characteristics and electrical properties on resistivity. There are three significant contributions of this work, each based on the following observations of (1) the absence of electrical flow through pore space at porosities less than a composite's porous percolation threshold, and (2) resistivity – porosity data in various sediments and rocks converge towards the theoretical lower Hashin-Shtrikman (HS) bound near the composite's critical porosities. The first significant contribution is the development of a tight empirical upper bound on the resistivity – total porosity relationship, where the upper bound is constrained by the percolation threshold at one end and by the critical porosity at the other. The upper bound is valid within the porosity range defined by the percolation threshold and critical porosity (Region II discussed in Chapter 3). The upper bound greatly reduces the range in possible resistivity values for a given porosity. The second significant contribution of this work is the development of a general equation that relates the internal geometry parameter and cementation exponent; both are empirical parameters in the resistivity – porosity relationship defined within the Region II porosity range. This relationship can be used to estimate one of the empirical parameters when the other can be constrained. The general relationship between the parameters is defined by a composite's critical porosity and the primary constituent's grain sphericity. The third contribution of this work is insight into predicting a formation's pore space characteristics using resistivity – porosity data. Discussion on the influence of various pore space characteristics is based upon decades of published observations. Each of these contributions is valuable to both the environmental and petroleum industries for improving the characterization of aquifers and reservoirs, respectively.

Electrical resistivity measurements are controlled by the formation's channel porosity, whereas seismic velocity measurements are controlled by the formation's total

porosity; thus the formation's channel porosity – total porosity relationship provides a link between resistivity and velocity. However, to date, minimal research has focused on relating resistivity and velocity. Work discussed in this final chapter focuses on theoretically and empirically exploring the relationship between electrical resistivity and seismic velocity. There are two significant contributions of this research. The first contribution is the development of upper and lower bounds on the electrical resistivity – seismic velocity relationship through their dependence on porosity. The resistivity – velocity bounds are simply created by combining resistivity and elastic moduli bounds at equal total porosities. These bounds can be used to constrain possible resistivity – velocity data pairs or to constrain the possible porosity range for a given data pair. The second contribution of this work is insight into constraining a formation's pore space characteristics using resistivity – velocity data. The real significance of these results is the potential for using known empirical relationships between resistivity and pore space characteristics to explain velocity trends and vice versa. With these results, electrical logs can be used to better constrain seismic interpretations and develop more accurate maps of flow properties; a benefit to both the petroleum and environmental industries.

Acknowledgments

The past six years have been a struggle, academically and personally. As a result, I've learned as much about life during my stay at Stanford as I have about geophysics. Without all of the wonderful people in my life, I wouldn't have had the strength to finish the program.

First and foremost, I'd like to express my sincere appreciation to my advisor Gary Mavko for having so much faith in me, treating me with so much respect, providing an endless number of motivating comments, always finding time to meet, and being so patient. I couldn't ask for a better advisor. Thank you Gary.

I'd also like to thank my loving parents, who have become two of my closest friends; I thank my mom for giving me the freedom to explore as a child and my father for always challenging my discoveries. Also, I thank my life-long friends at Stanford that always kept me moving forward; I will never forget all of the good times spent with them. In particular, the evenings kicking Andrea's butt in Thai boxing, the nights dancing with Sandra, Per, Andreas and Oscar, days spent at the lake with Ron, and lunches with the boreholes and GPS'ers; you all showed me more than fun times, you taught me the meaning of true friendship. I also appreciate the fabulous vacations with Ken and his continued friendship.

Finally, I thank the rest of my committee, Keith Loague, Amos Nur and Jack Dvorkin for their support. I also thank Mark Zoback for encouraging me to explore research in environmental geophysics and both he and Andre Journel for advising me during the first part of my research. I am also thankful for time spent with my friends in SRB; in particular, Tapan Mukerji, Manika Prasad, Youngseuk Keehm and Margaret Muir, who always seemed to be able to answer just about any question I had about rock physics, lab work, computers or administration. I would also like to thank Paul Bauman and James Armstrong of Komex International and Dave Sharpe, Susan Pullan and Jim Hunter of the

Geological Survey of Canada for providing data that I based the first two chapters of my thesis on, and Jon Nimmo and Kim Perkins at the USGS for the use of their lab equipment.

Table of Contents

List of tables

Number Page

List of figures

Number Page

CHAPTER 1: 3-D Characterization of the Complexity of an Alluvial Aquifer System: a case study using indicator geostatistics and gamma-ray and resistivity log interpretations

1.1 Introduction

The three-dimensional heterogeneity found within alluvial aquifer systems makes geologic characterization very challenging. In such an environment, it is difficult to determine the hydrogeologic connectivity between wells in three-dimensions using standard cross sections and geologic interpretations. However, geostatistics can be used to three-dimensionally analyze structural trends within the data and statistically interpolate between data values. Using geostatistics to build 3-D geologic models, the heterogeneities found within alluvial aquifer systems can be implemented in fluid flow and chemical transport modeling.

We used indicator geostatistics to three-dimensionally characterize a complex, alluvial aquifer system in the West Alberta Plains. To begin with, we analyzed ninety gamma-ray logs, induction logs, and lithology determined from cuttings, and assigned indicators (categories) of sandstone and till aquifers, and mudstone/siltstone aquitards. We used these indicators in the well columns to compute variograms and create a 3-D variogram model. Then, we simulated the sandstone and non-sandstone indicators using a sequential indicator simulation and constrained the simulation by the variogram model and the vertical proportions of sandstone and non-sandstone. We simulated the thickness of the till using sequential gaussian simulation and then we added the till to the sandstone and non-sandstone models. The resulting 3-D geologic models will provide the framework for groundwater flow and chemical transport modeling.

This paper presents a case study that used geophysical logs to interpret hydraulic units and geostatistical techniques to interpolate the geology between wells in a chemically influenced alluvial aquifer system. It provides a brief introduction to the geostatistical techniques that were used in this project and presents the results of the application of indicator geostatistics to a chemically influenced alluvial aquifer system.

For a comparable study using borehole indicators and kriging to characterize an alluvial depositional environment see N. M. Johnson and S. J. Dreiss (1989). For a detailed introduction to geostatistics see E. H. Isaaks and R. M. Srivastava (1989), P. Goovaerts (1997), and C. V. Deutsch and A. G. Journel (1997). For an overview of potential heterogeneities found within alluvial depositional environments see C. S. Bristow and J. L. Best (1993) and B. R. Rust (1978). For an introduction to geophysical well log analysis see M. H. Rider (1991) and Schlumberger (1989).

1.2 Background

Operations at a gas plant over the past thirty years led to sulfolane, a plant process chemical, affecting the local alluvial aquifer system at the site. There is a need to understand the potential for further spreading of sulfolane in the deep aquifers, which are tapped by nearby residential wells. The objective of the project was to develop 3-D geologic models of the chemically influenced alluvial aquifer system, which will be used for the groundwater flow and chemical transport modeling.

The gas plant is located on a topographic high within the gently rolling West Alberta Plains (see Figure 1.1). For the most part, the local topography was created by glacial scouring of the sedimentary bedrock. Unconsolidated clayey to sandy till, 0.5 to 10 m thick, disconformably overlies interbedded sandstone, siltstone and mudstone bedrock of the Paskapoo Formation. The Paskapoo was deposited to the east of the Rockies in the Alberta Basin as a result of erosion during orogenic events in the Lower Paleocene to Middle Eocene (J. R. McLean and T. Jerzykiewicz, 1978). The Paskapoo sequence is dominated by horizontal to slightly dipping facies of the mid to distal alluvial fan (T. Jerzykiewicz, 1997). The area of study is thought to be within the Lacombe member of

the Paskapoo Formation, which is believed to be the majority of bedrock in this area of the Alberta Foothills (T.D. Demchuk and L.V. Hills, 1991).

Within the area of the gas plant, the till and the Paskapoo sandstones are interpreted to be the primary aquifer units. Over seven aquifers have been identified in the Paskapoo, and five primary shallow aquifer units were named the A, B1, B2, C, and D aquifers (Komex International Ltd., 1996a, 1996b). Since most nearby residential wells are completed within the D unit and deeper, the potential for further spreading of plant process chemicals in the deep sandstone units is of concern. Therefore, understanding the potential vertical and horizontal connectivity of the aquifers is necessary for assessing the likelihood that other residential wells completed in the Paskapoo could become influenced by the sulfolane plume.

Sulfolane is a water-miscible organic compound that was disposed of at several locations around the gas plant (Figure 1.1). Influence from sulfolane has been detected as far as 2.5 km laterally and 120 m vertically from the source locations. Of the 30 nearby private water wells, six have been influenced by the plant operations (Komex International Ltd., 1997). The most likely vertical and lateral transport pathways for chemically influenced groundwater flow are by way of (1) intermediate sandstones that connect the major sulfolane-containing sandstone aquifer units, (2) the 13 un-cased and partly-cased water wells (now abandoned) near the landfills, (3) surface runoff from the plant and surface springs from sulfolane-influenced aquifers, and (4) near-surface pipeline trenches.

Since 1986, a large data set has been collected to characterize the distribution and migration of chemically influenced groundwater within the aquifer system. Hydraulic head has been recorded in 150 piezometers. Pumping tests were conducted in three of the wells (Komex International Ltd., 1996a). Water samples have been chemically analyzed in over 220 locations. And geophysical logs were collected in 90 wells.

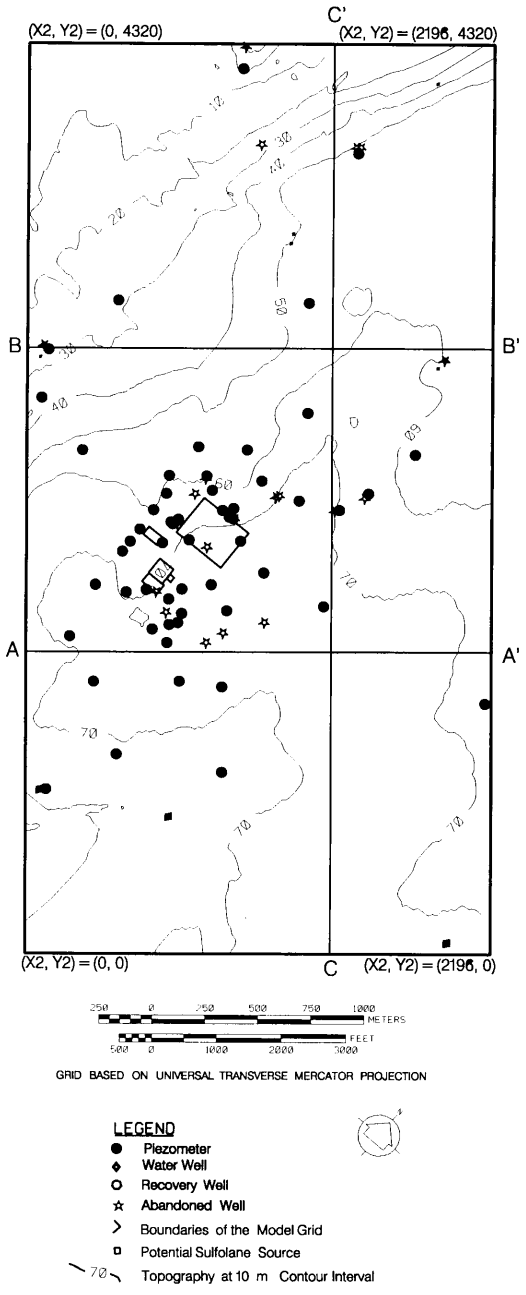

Figure 1.1: Well Log Locations: Locations of wells with interpreted geophysical logs and schematic of model grid coordinates.

1.3 Methodology

1.3.1 Well Log Analysis

In conjunction with lithology derived from cuttings, we analyzed 90 gamma-ray and induction logs (see Figure 1.1 for locations) and interpreted three categories: sandstone, non-sandstone and till (Figure 1.2). We used these three categories since data suggest that the sandstone units are the primary aquifers, the till units are the secondary aquifers, and the siltstone and mudstone units are the aquitards. We assigned each category an indicator, (an integer code) so that we could statistically analyze the data.

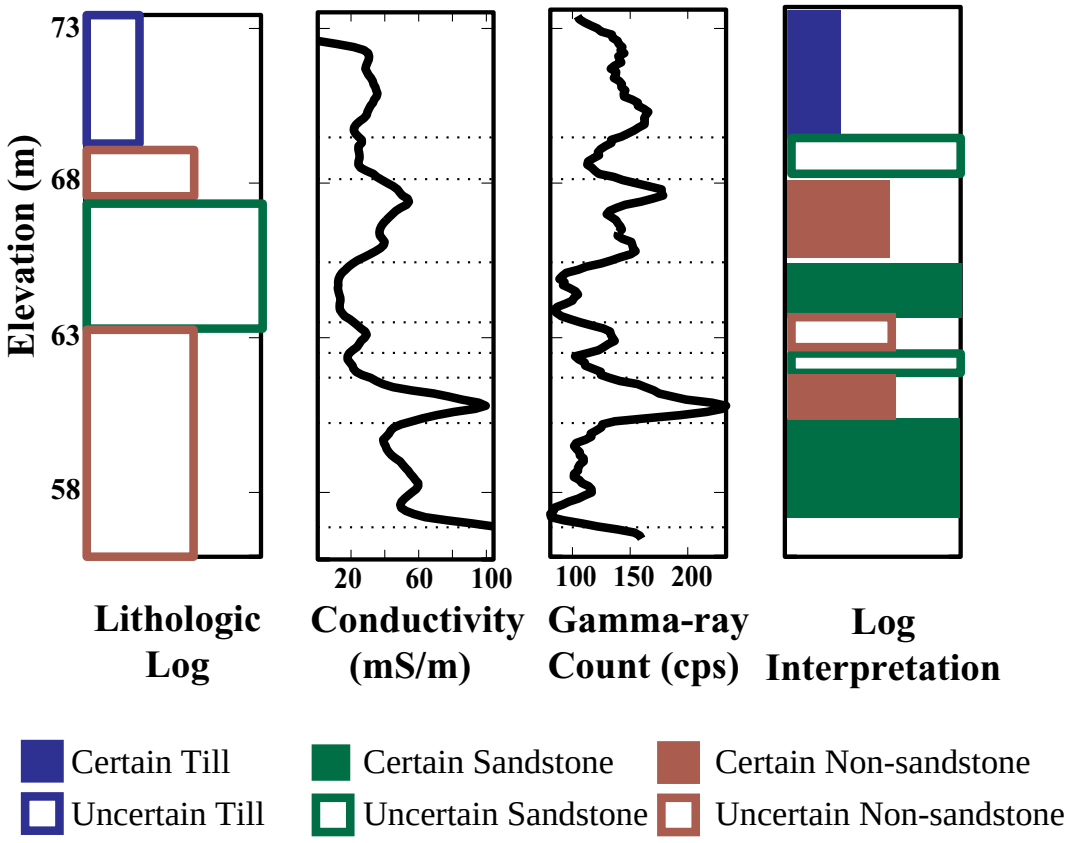

Figure 1.2: Example well log interpretation. Example of our interpretation of a good set of well logs where the lithologic log correlates very well with the gamma-ray and induction logs. TI = till; SS = Sandstone; NSS = non-sandstone. Elevation is with respect to the base of the simulated grid.

Because the interface between the till and the Paskapoo bedrock is easily recognizable during drilling, we trusted the portion of the lithologic log that described the depth and thickness of the till. However, the interfaces between sandstone and non-sandstone units are not easily recognizable during drilling. Consequently, the depths and thickness' of the sandstone and non-sandstone units in most wells appeared to be inaccurate when compared to the geophysical logs. Also, significant sandstone and non-sandstone units were not described in many of the lithologic logs when obvious signatures of the units were present in both the gamma-ray and conductivity logs. There were, however, some exceptionally well recorded lithologic logs (Figure 1.2). Therefore, we primarily used the geophysical logs and secondarily used the lithologic logs to interpret the sandstone and non-sandstone units. The interpretations of the well logs are quite subjective since we could not quantitatively interpret the existing well log data. While interpreting the logs, we kept track of our certain and uncertain interpretations of the hydraulic units. The certain and uncertain interpretations then became the data for the geostatistical simulation of the till and sandstone aquifers and the non-sandstone aquitards. When we refer to certain and uncertain indicators throughout this paper, we are referring to a confidence in our log interpretations.

1.3.2 Vertical Analysis

The vertical proportion curve shown in Figure 1.3.a is a display of the vertical distribution of sandstone averaged across the entire aquifer system. To construct the vertical proportion curve, we calculated the average fraction of sandstone found every quarter meter vertically across the entire site (solid line in Figure 1.3.a). In the analysis, only the certain sandstone and non-sandstone well log interpretations (excluding till) were averaged. Thus, the figure represents the vertical fraction of sandstone, and it can also be interpreted as one minus the fraction of non-sandstone across the entire site. Distinct vertical intervals of sandstone (see Figure 1.3a) directly correlate with the A, B1, B2, C and D aquifers that were previously identified. The existence of distinct non-sandstone units is equally important since they are likely to act as partial vertical barriers

to flow. Additionally, note that a significant amount of sandstone lies below the D aquifer, and sulfolane is found at 0 m, the base of the grid; therefore, residential wells that tap the D aquifer unit might be at risk of becoming contaminated, depending on the directions of flow. The results of this analysis were used to constrain the amount of sandstone in each vertical interval during the geostatistical simulation (pluses in Figure 1.3.a).

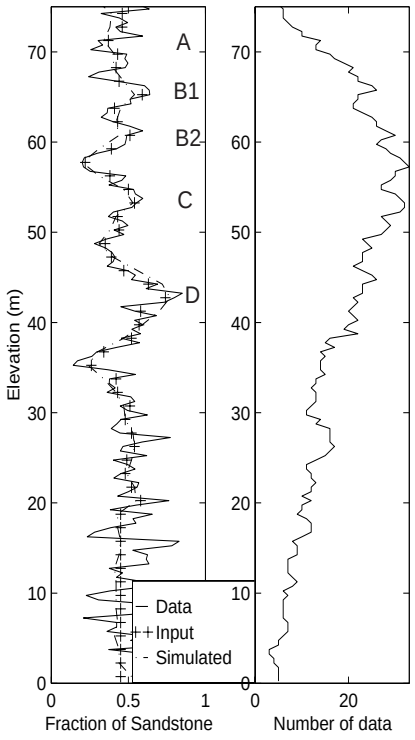

Figure 1.3: Vertical proportion curve. (a) the vertical proportion of sandstone that is: data averaged 0.25 m vertically across site (solid line), input sandstone proportion averaged 1.5 m vertically (pluses), and simulated on 1.5 m vertical interval (dashed line); (b) the amount of data that contributed to the input vertical proportion curve (pluses in (a)). The simulated vertical proportion of sandstone (dash-dot line in (a)) obeys the input sandstone proportion (pluses in (a)).

The number of the certain log interpretations at each quarter meter vertical interval across the entire site is displayed in Figure 1.3.b. Most of the wells extend between 70 and 40 meters above the base of the grid. From 80 - 20 m, we constrained the

geostatistical simulation by the vertical proportion curve, and below 20 m we constrained it by a constant proportion of 45% sandstone, the global proportion of sandstone.

1.3.3 Variogram Analysis

A variogram is a statistical measure of 3-D spatial variability of the data. In geologic terms, the variogram gives the directions of maximum and minimum continuity of geologic structures, the regional dip of structures, and the weight of nearby data values. As one expects, in an alluvial depositional environment there will be a greater correlation of sandstones in the general direction of channel flow than in the direction perpendicular, and the lithology at an observation point will be strongly influenced by near lithology and weakly influenced by far lithology.

The variogram is defined as half of the averaged squared difference between two data values. The mathematical expression for the variogram is given in Equation 1.1.

$$\gamma(h) = \frac{1}{2N(h)} \sum_{i=1}^{N(h)} (x_i - y_i)^2 \qquad (1.1)$$

$\gamma(h)$: variability of data pair that are a distance h apart
h: distance between data pair
i: index of the data pair
$N(h)$: number of data pair that are a distance h apart
x_i: one datum in the data pair
y_i: the other datum in the data pair

We used the semi-variogram algorithm named gam from GSLIB2, a geostatistical library developed within the Stanford Center for Reservoir Forecasting (C. V. Deutsch and A. G. Journel, 1997, p 44), to compute the variograms for the indicator of sandstone versus non-sandstone. Using the variograms, we concluded that the geologic structure is horizontal, the direction of maximum continuity (general direction of channel flow) is approximately NS, and the direction of minimum continuity is approximately EW. These results are supported by paleocurrent data presented in J.R. McLean and T. Jerzykiewicz (1978).

After computing the variograms, we modeled them in the three principal directions: the directions of maximum and minimum continuity, and vertically. The reason for modeling the variograms is to develop a mathematical expression valid for all 3-D separation vectors, *h*. The range of data influence is represented by an ellipsoid with a major axis of 185 m NS, an intermediate axis of 60m EW, and a minor axis of 3.4 m vertically as shown in Figures 1.4 a, b, and c.

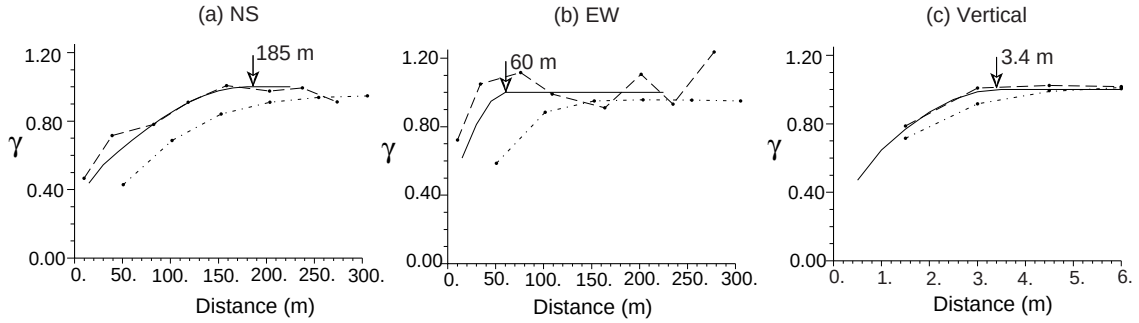

Figure 1.4: Variograms and variogram model. The model variogram (solid line) , the data variogram (large dashes), and the smoothed simulation variogram (small dashes) for (a) the direction of maximum continuity (NS), (b) the direction of minimum continuity (EW), and (c) the vertical. The modeled distances of continuity (ranges) are shown.

1.3.4 3-D Geostatistical Simulation

At some point, one must make a decision of spatial stationarity to interpolate between data points. The decision of stationarity is a decision that allows the spatial grouping of data for statistical inference within the sampled area. At this site, there is a blanket of till of varying thickness over the horizontally bedded, alluvial sandstones, siltstones, and mudstones of the Paskapoo Formation. Therefore, we simulated the till differently than the sandstones and non-sandstones.

To simulate the sandstones and non-sandstones, we used a sequential indicator simulation algorithm named sisim_lm from GSLIB2. Only two categories populated the grid: sandstone and non-sandstone. At each grid node, the category was simulated according to its conditional cumulative distribution function. In this case, the conditioning data was the certain and uncertain indicators of sandstone and non-

sandstone and all previously simulated values found within a neighborhood of the node being simulated. For every grid node that was geostatistically simulated, the variability defined in Equation 1.1, γ(h), determined the weight of conditional data found within the range (ellipsoid) of each unknown node. We ran three simulations of sandstone and non-sandstone on a 2196x4320x79.5 m grid using a 36x36x1.5 m grid cell size.

The mathematical expression used in sisim_lm is given in Equation 1.2. Equation 1.2 tells us that the probability of a categorical variable (i.e. sandstone or non-sandstone) at a location is equal to the overall proportion of that categorical variable plus a correction term accounting for the surrounding observed indicator data (C. V. Deutsch and A. G. Journel, 1997, p. 151).

$$\Pr ob\{I(u;s_k)=1\,|\,(n)\} = p_k + \sum_{\alpha=1}^{n} \lambda_\alpha [I(u_\alpha;s_k) - p_k] \qquad (1.2)$$

u: location
n: number of data
α: index in the number of data
k: number of categories
p_k: global proportion of the k^{th} category
λ: weight of data
s_k: k^{th} category ID
$I(u; s_k)$: indicator random function model at u, for s_k
Prob: probability of the $I(u; s_k)$ for all n data

In the three resulting realizations, there are isolated cells of sandstone and non-sandstone because the range of minimum horizontal continuity, 60 m, is not much larger than the horizontal grid size, 36 m. Also, the results from pumping tests suggest that the variogram ranges may be conservative, though the connectivity from hydraulic tests and continuity of sandstones are not equivalent variables. Therefore we slightly smoothed the realizations using an algorithm named trans from GSLIB2 to group isolated sandstone and non-sandstone cells with nearby large sandstone and non-sandstone bodies, respectively. As a result of the smoothing, the range of the smoothed variogram is greater than the range of the modeled input variogram (Figure 1.4). The vertical proportion curve of the smoothed simulation fits the input vertical proportion curve very well (Figure 1.3). Both sets of the un-smoothed and smoothed realizations will be used in the flow simulation to determine the most representative geologic model.

To simulate the thickness of the till and the topographic elevations, we used the sequential gaussian simulation algorithm named sgsim from GSLIB2. When simulating the thickness of the till, the conditioning data were the thicknesses of the till from the log interpretations and all previously simulated values found within a neighborhood of the location being simulated. When simulating the topography, the conditioning data were the elevations from the digital elevation model and all previously simulated values within a neighborhood of the location being simulated. 2-D sections of one of the final 3-D simulations are shown in Figures 1.5 and 1.6.

The mathematical expression used in sgsim is given in Equation 1.3. Equation 1.3 tells us that the expected value of a variable (i.e., thickness or elevation) at an unsampled location is equal to the sample mean of the variable plus a correction term accounting for the surrounding observed data (C. V. Deutsch and A. G. Journel, 1997, p. 140).

$$E\{Y(u_o)|y(u_\alpha) = y_\alpha, \alpha = 1,\ldots,n\} = m + \sum_{\alpha=1}^{n} \lambda_\alpha [y_\alpha - m] \qquad (1.3)$$

u: location
n: number of data
α: index in the number of data
m: sample mean
y: variable (data value)
λ: weight of data value
Y: random function model at u
E: conditional expected Y value

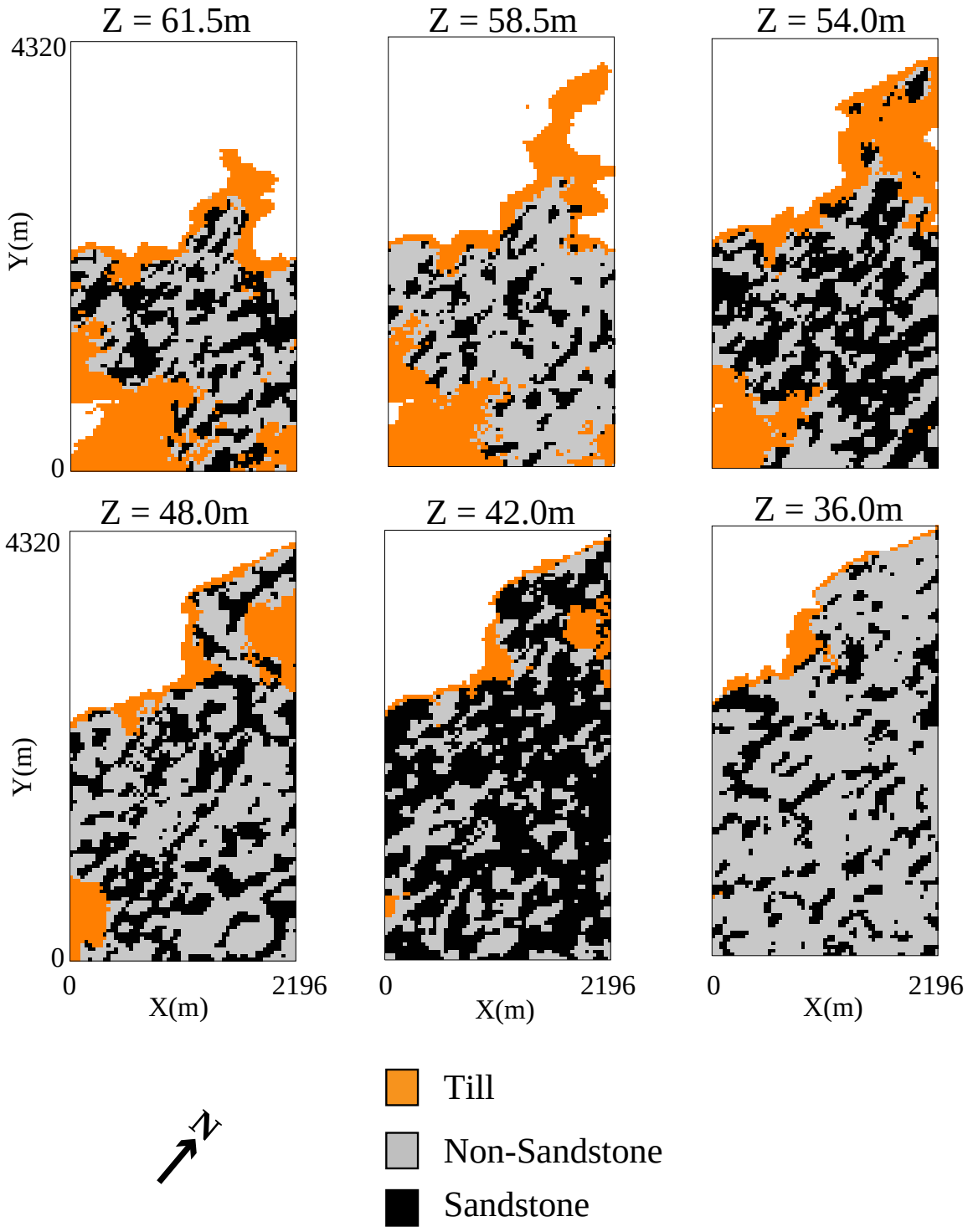

Figure 1.5: Smoothed elevation slices. Elevation slices of a smoothed model in the X2Z2 plane at (a) Z2 = 61.5 m, (b) Z2 = 58.5 m, (c) Z2 = 54.0 m, (d) Z2 = 48.0 m, (e) Z2 = 42.0 m, (f) Z2 = 36.0 m, where Z2 is measured up from the base of the grid. White = no simulated value (in the air).

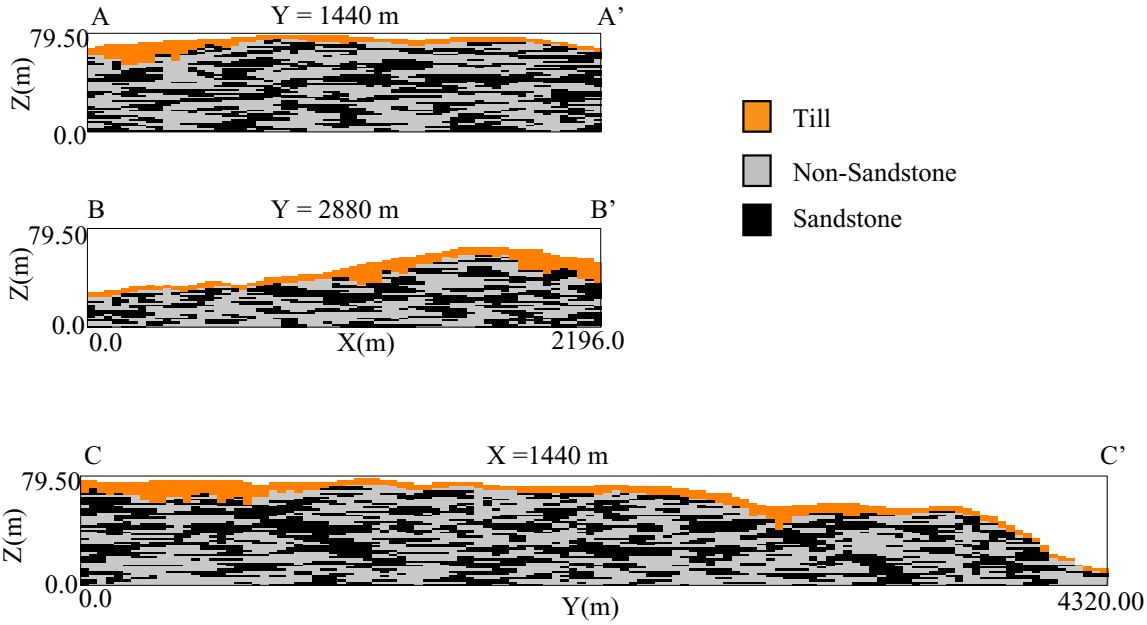

Figure 1.6: Smoothed cross-sections. Cross-sections of a smoothed model in the X2Z2 plane at (a) Y2 = 1440 m and (b) Y2 = 2880 m, and in the Y2Z2 plane at (c) X2 = 1440 m. See Figure 1 for cross-section locations. White = no simulated value (in the air).

1.4 Discussion

The objective of this project was to three dimensionally characterize the complexity of an fluvial aquifer system. Interpretation of 3-D structure using only well data requires one to make decisions about potential structural geometries. Considering the complexity of the aquifer system and the limited amount of data at this site, it would be extremely difficult to objectively interpolate hydrogeologic continuity between wells three-dimensionally using standard cross sections and geologic interpretations. In this project, geostatistical techniques were used to three-dimensionally analyze the well data and statistically simulate between data values. The simulations were constrained by the certain and uncertain data values, the potential structural continuity of sandstones and non-sandstones, and the vertical proportion of sandstone and non-sandstone. The geostatistical simulation techniques, however, are not entirely objective since one must always make decisions about which input parameters are appropriate for each simulation.

There are distinct vertical intervals of sandstone that correlate extremely well with the intervals of the A, B1, B2, C and D aquifer units. It is promising to see that the vertical intervals of sandstones identified in the vertical proportion curve matched the previously determined aquifer units. In our well log analysis, we interpreted sandstone, non-sandstone and till units throughout the entire column of each well log and we did not use previous interpretations of aquifer units to influence our log interpretations. The results support the assumption that the sandstone units are the aquifers and the non-sandstone units are the aquitards.

There are distinct vertical intervals where there are large proportions of non-sandstone, as well as intervals with large portions of sandstone. The large non-sandstone units may provide partial barriers to vertical groundwater flow and retard the spreading of sulfolane vertically. However, until the groundwater flow is modeled, it will not be clear if there is potential for other residential wells to become influenced by the sulfolane plume.

When evaluating each of the geologic models, it is important to keep in mind where the data-poor regions of the site are located. For example, horizontally, most of the wells are clustered near the plant, and vertically, most wells pass between 70 and 40 m above the base of the grid. The geostatistical models display high uncertainty since the well data are horizontally sparse relative to the short ranges in continuity of the sandstone and non-sandstone units. In these data-poor regions of models, the geostatistical simulation is extrapolating rather than interpolating between data values, leading uncertain estimations.

There are differences between each of the three realizations, however each represents equally likely geologic conditions, given the current data at the site. Again, the objective of this project was to develop 3-D models that represent the geology, not to determine the exact geometry of the aquifers and aquitards for exploration. There are several ways to improve the geologic model if the hydraulic conditions at this site cannot be matched during the flow simulation, one of which includes collecting additional data to better constrain the geostatistical simulation.

If core had been available at this site, lab-measured porosity and clay content data could have been used to calibrate the gamma-ray and conductivity logs so that porosity and clay content could have been predicted where lab data was not available. Additionally, this project may have benefited from 2-D geophysical data to better interpret the horizontal continuity of structure. In the next chapter, we took a more quantitative approach to interpreting the gamma-ray and resistivity logs at a site where core data was available for calibration.

1.5 References

C.S. Bristow and J.L. Best. 1993. Braided rivers: perspectives and problems. *Braided Rivers*. Eds. J.L. Best and C.S. Bristow. Geological Society Special Publication: No. 75. P. 13 - 71.

T.D. Demchuk and L.V. Hills. 1991. A re-examination of the Paskapoo Formation in the central Alberta Plains: the designation of three new members. *Bulletin of Canadian Petroleum Geology*. Vol. 39, No. 3, P. 270 - 282.

C.V. Deutsch and A.G. Journel. 1997. *GSLIB: Geostatistical Software Library and User's Guide*; Second Edition. Oxford University Press.

P. Goovaerts. 1997. *Geostatistics of Natural Resources Evaluation*. Oxford University Press.

E.H. Isaaks and R.M. Srivastava. 1989. *An Introduction to Applied Geostatistics*. Oxford University Press.

T. Jerzykiewicz. 1997. Stratigraphic Framework of the Uppermost Cretaceous to Paleocene Strata of the Alberta Basin. *Geological Survey of Canada*: Bulletin 510.

N.M. Johnson and S.J. Dreiss. 1989. Hydrostratigraphic Interpretation Using Indicator Geostatistics. *Water Resources Research*. Vol. 25, No. 12, P. 2501-2510.

Komex International Ltd. 1996a. Harmattan Aquifer Test Program. Unpublished report to Mobil Oil Canada, January 1996. File No. KI95-3710-3.

Komex International Ltd. 1996b. Piezometer Installation Program: Harmattan Gas Plant. Unpublished report to Mobil Oil Canada, April 1996. File No. KI96-3710-4.

Komex International Ltd. 1995. 1995 Groundwater Quality Monitoring Program at the Harmattan Sour Gas Plant. Unpublished report to Mobil Oil Canada, January 1996. File No. KI95-3710-3.

J.R. McLean and T. Jerzykiewicz. 1978. Cyclicity, tectonics and coal: some aspects of fluvial sedimentology in the Brazeau-Paskapoo Formations, Coal Valley area, Alberta, Canada. *Fluvial Sedimentology*. Ed. Andrew D. Miall. Canadian Society of Petroleum Geologists. P. 441 - 468.

M.H. Rider. 1991. *The Geological Interpretation of Well Logs*; Revised Edition. Whittles Publishing.

B.R. Rust. 1978. Depositional Models for Braided Alluvium. *Fluvial Sedimentology*. Ed. A. D. Miall. Canadian Society of Petroleum Geologists. P. 605 - 625.

Schlumberger. 1989. *Log Interpretation Principles/Applications*. Fourth Printing.

CHAPTER 2: Predicting Clay Content, Porosity and Permeability from Well Logs: a case study quantitatively interpreting gamma-ray and resistivity logs

2.1 Introduction

The objective of aquifer characterization is not only to develop maps representative of the geometries of aquifers and aquitards (as in Chapter 1), but also to map the characteristic flow properties, such as porosity and permeability. Often, the permeabilities of a few selected aquifers are measured by way of pumping tests, and the porosities are assumed. Porosity and permeability, however, can be quantified using a combination of conductivity logs, gamma-ray logs, and empirical and theoretical relationships that are typically used for petroleum reservoir characterization. This chapter focuses on predicting flow properties in shallow aquifers using geophysical data. In order to predict the flow properties using gamma-ray and resistivity logs, we needed lab-measured core data to calibrate the relationships used in this chapter. Since core data was not available at the site described in Chapter 1, we worked with a data set in this chapter where core was available.

In the Aurora well in the Oak Ridges Moraine complex (ORM), Ontario, we used the gamma-ray log to predict clay volume and used the conductivity log to predict porosity and permeability. To begin with, we derived empirical relations between the gamma-ray count and lab-measured clay volume, then predicted clay volume throughout the entire Aurora well. Next, we used a modified Archie's equation with a clay correction to calculate formation resistivity factor. We derived empirical relations between lab-

measured porosity and log-predicted formation factor, then predicted porosity throughout the entire well. Finally, we estimated permeability throughout the Aurora well using a statistical relationship between permeability and formation factor, grain size and sorting.

We had to make two common assumptions about the formation factor – porosity relationship, whose influence on the porosity predictions is likely important. Because the lab-measured porosity data is sparse within each formation, we had to assume one empirical parameter a is constant in the formation factor - porosity relationship. Additionally, we assumed that the lab-measured channel porosity equaled the total porosity since we did not have a way of converting between the two in these formations. This common assumption likely leads to underestimates of the total porosity using the resistivity data. Solutions to these common problems are discussed in Chapters 3 and 4.

2.2 Site and Data Background

The Oak Ridges Moraine (ORM) is located in the Greater Toronto Area, Ontario, and is one of the most heavily used groundwater sources in Canada. The ORM is up to 150 km long EW and 20 km wide NS and 150 m thick in some locations (Sharpe et al, 1996). Depletion and potential contamination of the ORM Quaternary glacial aquifers has led to an effort by the Geological Survey of Canada (GSC) and others to develop a regional hydrostratigraphic model for land-use planning and for identifying valley-channel aquifers, and recharge and discharge areas (Hunter et al, 1998; Pullan et al, 1997; Russell et al, 1996). Four major hydrostratigraphic units have been identified in the ORM area, from the youngest units downwards (Sharpe et al, 1996): the Halton/Kettleby drift local aquitards and aquifers, ORM regional aquifer, Newmarket Till regional aquitard, and lower drift regional aquifers and local aquitards.

The Aurora lithologic column (Figure 2.1) is characterized by thick gravelly to medium sand (ID =1, Table 2.1), fine to very fine silt (ID = 2), sandy gravel (ID = 5), poorly sorted, clayey silt till (ID = 4) and silt/clay rythmite sequence (ID = 3) glacial deposits. The water table is at approximately 22 m depth in a medium sand unit characterized by fining upward sets 0.5 – 1.5 m thick, underlain by a 3 m thick sandy

gravel unit. The aquitard below is a very dense, poorly sorted, clayey silt till and dense silt/clay rythmites. The aquifer 56 – 98 m is characterized by fining upward sequences ~ 0.5 m thick of very slightly calcite-cemented, medium sand to fine silt, with a 4 m thick fine to very fine silt bed at 52 m. Below 98 m is characterized by interbedded coarse sand and gravelly sand aquifers, and silty, sandy gravels, with cobbles.

The Aurora gamma-ray, conductivity, velocity and lithologic logs (Figure 2.1) and access to the core were provided by the GSC. At the GSC, we drilled 42 plugs and gathered 33 grab samples from the air-dried core, almost uniformly sampling the well. We measured the grain size distribution (Table 2.1; Figure 2.2) of 46 samples using a Coulter LS230 laser particle size analyzer at the USGS, Menlo Park, and calculated the geometric mean grain size, standard deviation of grain sizes, and clay volume. At the Stanford Rock Physics (SRB) laboratory, we measured the effective porosity (Table 2.1; Figure 2.2) of 24 plugs (dried at 42° C) using a Coberly-Stevens gas porosimeter.

Lithologic		Lab V_{cl}			Lab ϕ			Lab grain size		
ID	class	mean	SD	N	mean	SD	N	d(mm)	σ	N
1	sand	0.043	0.024	21	0.360	0.023	11	0.1926	2.0352ϕ	21
2	silt	0.063	0.018	4	0.380	0.001*	2	0.0365	1.6850 ϕ	4
3	silt/clay	0.485	0.025	6	0.300	0.018*	2	0.0045	1.9417 ϕ	6
4	clayey silt	0.261	0.044	8	0.209	0.006	6	0.0181	3.0288 ϕ	8
5	gravel	0.011	0.008	7	0.308	0.013*	3	6.5844	2.3057 ϕ	7

Table 2.1: Lab-measured properties in five distinctly different lithologies. SD is the standard deviation of the lab measured values; N is the number of samples; V_{cl} is the clay volume; ϕ is the porosity; d is the geometric mean grain size, σ is the standard deviation of the $\log_2$ grain size (phi scale). * sparse data.

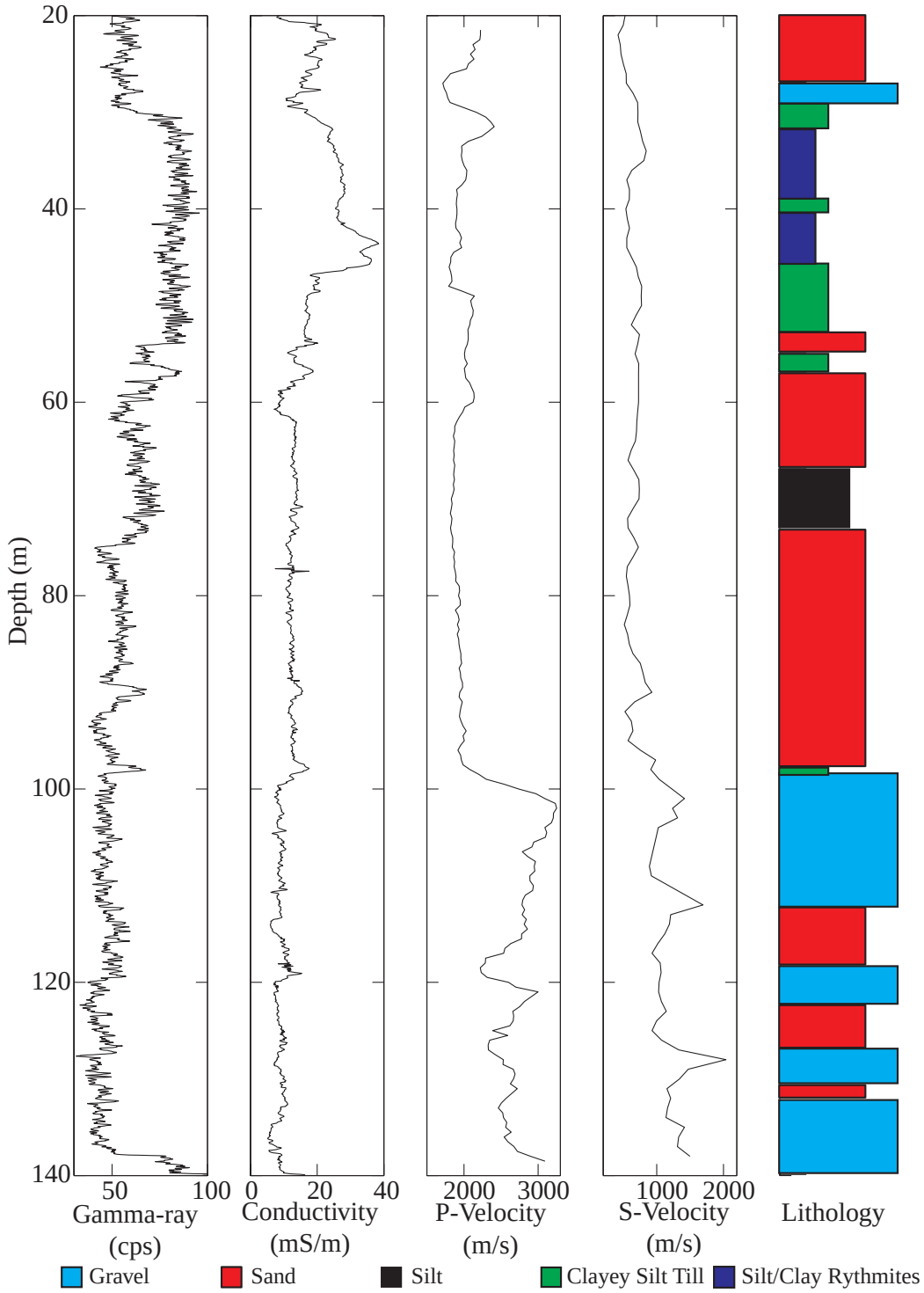

Figure 2.1: Aurora well logs. Gamma-ray, conductivity, P-wave velocity, S-wave velocity and lithologic logs.

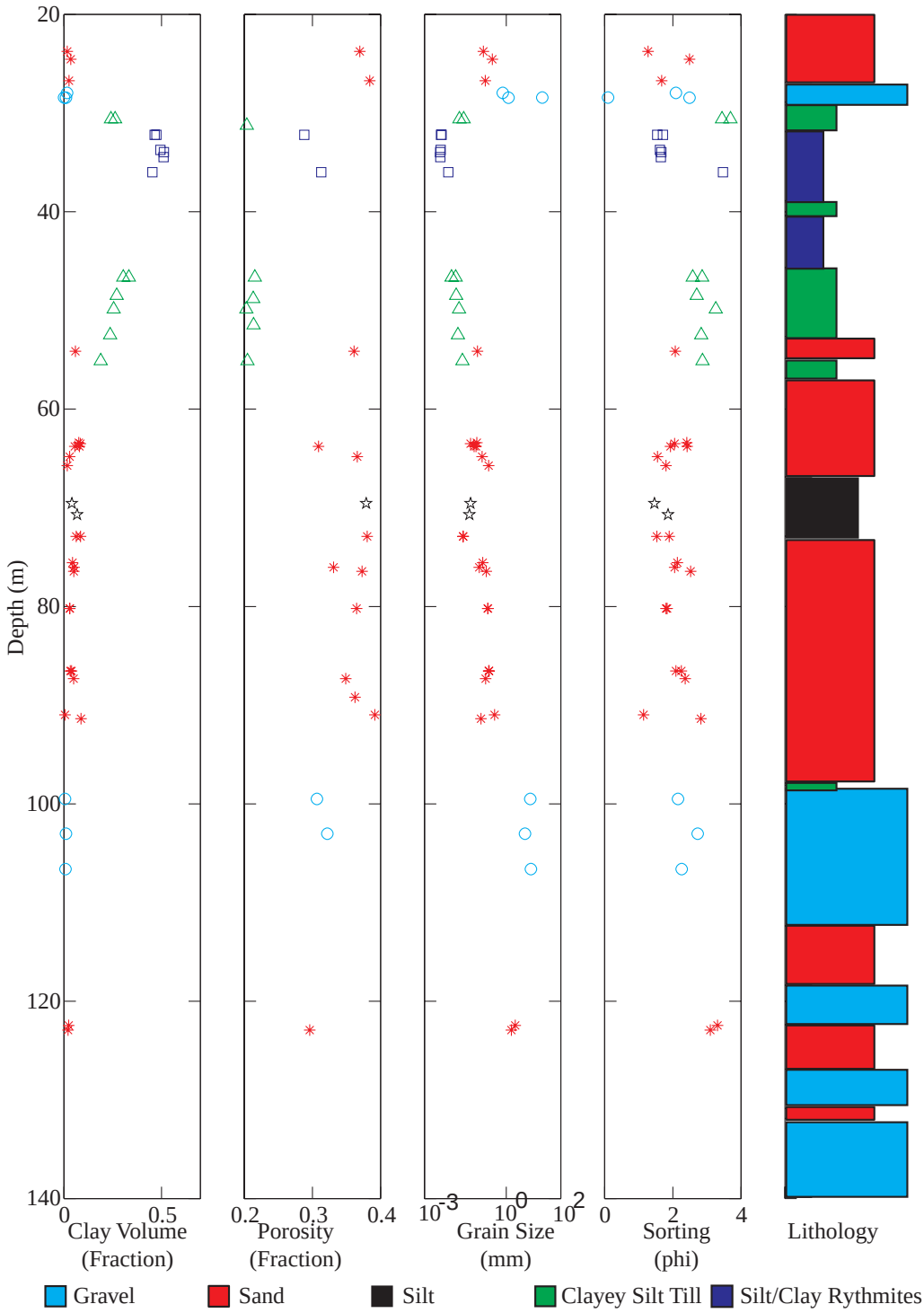

Figure 2.2: Aurora lab data. Clay volume, porosity, grain-size and sorting (standard deviation of the $\log_2$ grain sizes)

2.3 Methodology

2.3.1 Predicting Clay Volume

Clay content strongly influences both porosity and permeability. For example, because clays are highly compressible they can have porosities from 10 to 80 percent. Even the highest porosity clays will have low permeabilities because of small pore sizes and high capillary forces. Because of these characteristics, even a small amount of clay can clog pore space and pore throats, influencing both porosity and permeability.

We took two steps in predicting clay volume fraction in the Aurora well. First we derived empirical relations between the gamma-ray count and lab-measured clay volume for each lithologic ID index (Table 2.1). Second, we predicted clay volume throughout the entire well using the empirical relationships and the gamma-ray log.

Step 1: Derive Empirical Relationship

We derived the empirical constant A2 from the following empirical relation between the lab-measured clay volume fraction and co-located gamma-ray log value (Tiab and Donaldson, 1996).

$$V_{cl}^{i,j} = A_1(2^{A_2^j I^i} - 1) \tag{2.1}$$

where:

$$I^i = \frac{\gamma^i - \gamma_{sa}}{\gamma_{cl} - \gamma_{sa}} \tag{2.2}$$

V_{cl}: predicted clay volume fraction
I: radioactive index
A_1: lithology-related constant 1
A_2: lithology-related constant 2
γ: gamma-ray value
γ_{sa}: sandgamma-ray value
γ_{cl}: clay gamma-ray value
i: depth index
j: lithologic ID index

Suggested values of A_1 and A_2 (Schlumberger, 1991; Tiab and Donaldson, 1996) are (1) $A_1 = 0.083$ and $A_2 = 3.7$ for Tertiary clastic sediments (at depths < 4000 ft), and (2) $A_1 = 0.33$ and $A_2 = 2$ for Pre-Tertiary rocks (at depths 4000 – 8000 ft). First, we tried the published values $A_1 = 0.083$ and $A_2 = 3.7$; however, the fit to the lab V_{cl} values was ± 4.3% clay volume fraction. Next, for each of the five lithologic classes in Table 2.1, we assumed $A_1 = 0.083$ and derived a best fit $A_2 > 0$, where the error squared e (Eqn. 2.3) between the log-predicted and lab-measured clay fraction was minimized (results in Table 2.2).

$$min(e^j) = \sum_{k=1}^{N^j} (V_{log}^{k,j} - V_{lab}^{k,j})^2 \qquad (2.3)$$

e: squared error
V_{log}: log-predicted value
V_{lab}: lab-measured value
N: number of lab samples
j: lithologic ID index
k: sample number index

Constraining A_1 to the published value 0.083 allowed us simplify the calibration. Using these derived A_2 values in Eqn. 2.1, we calculated the total error (± 2.1% clay volume) as the overall standard deviation of the absolute residuals between log-predicted and lab-measured clay volume fractions for all lithologies.

As is often done in Eqn. 2.2, we assumed that the maximum gamma-ray log value is representative of pure clay (γ_{cl}) and the minimum gamma-ray value is representative of clay-free formations (γ_{sa}). This is only true if nearly pure clay and clay-free formations exist along the well column. Gamma-ray counts can vary enormously between clays; however, they tend to remain nearly constant at any one site (M. H. Rider, 1986).

It is common practice to use Eqn. 2.2 to calculate clay volume fraction ($I \approx V_{cl}$) rather than Eqn. 2.1. Both Eqns. 2.1 and 2.2 are empirical and equally useful. The difference between using Eqn. 2.1 and Eqn. 2.2 (with the assumption $I \approx V_{cl}$) is that Eqn. 2.1 assumes a non-linear relationship between gamma-ray count and clay volume, whereas Eqn. 2.2 assumes a linear relationship. By using Eqn. 2.2, the empirical parameters that fit the data are absorbed into the γ_{cl} and γ_{sa} parameters, which strictly speaking should not

be empirical. In Eqn. 2.1, however, the empirical parameters that fit the data are adsorbed into the empirical parameters A_1 and A_2.

Step 2: Predict Clay Volume

We used the lithologic log (ID indices with depth; Figure 2.1) to select the derived A_2 values (Table 2.2), then used the empirical Eqn. 2.1 to predict the volume of clay V_{cl} throughout the Aurora well below the water table. The predicted and lab-measured volume of clay and total error are plotted with depth in Figure 2.3.

Discussion

The log-predicted clay volume in the Aurora well fits the lab-measured clay volume data and the lithologic log very well. The scatter in the predicted volume of clay between 30 and 40 m depth (Figure 2.3) may be a response to either the clay and silt rythmite sequences or noise in the gamma-ray log. The spike in the predicted clay volume at 97 m depth is a response to a thin bed of clayey silt, shown in the lithologic log. The presence of potassium feldspar minerals likely increases the gamma-ray response and causes scatter in the relationship between clay volume fraction and gamma-ray count in the sands. The predicted V_{cl} mean is significantly lower and the standard deviation is higher (Table 2.2) than the lab-measured sample statistics (Table 2.1), especially for lithologic ID 3 and 4. This discrepancy may be due to insufficient sampling in the well or noise in the gamma-ray log.

Since the gamma-ray logger was not calibrated, the gamma-ray values are dependent on the size and type of gamma-ray logger crystal, borehole completion, and the clay type. However, Eqn. 2.1 is independent of the tool type and well completion if one can assume $\gamma_{sa} = \gamma_{min}$ and $\gamma_{cl} = \gamma_{max}$. This is true since there is a linear correction for the well completion and logging tool type, and the radioactive index is simply normalized by the range in gamma-ray values (Eqn. 2.2). The derived A_2 values can be used to predict clay volume most accurately in the Oak Ridges Moraine where the same logging tool was used in similarly completed wells as the Aurora well. The Aurora well was completed

with 2 inch PVC casing as was logged using a Geonics GAMMA39 (25 mm diameter, 65 mm long Sodium Iodide crystal).

		Predicted V_{cl}		Predicted F			Predicted ϕ		Predicted k (Darcy)	
ID	A_2	mean	SD	mean	SD	m	mean	SD	mean	SD
1	1.6	0.032	0.020	5.3	1.4	1.6	0.364	0.057	1.326	1.128
2	1.5	0.033	0.019	4.9	0.3	1.6	0.369	0.011	$2.120\text{x}10^{-3}$	$2.821\text{x}10^{-3}$
3	3.5	0.124	0.182	7.5	3.1	1.8	0.354	0.090	$3.786\text{x}10^{-5}$	$4.383\text{x}10^{-5}$
4	3.0	0.088	0.115	7.5	2.5	1.3	0.229	0.058	$1.915\text{x}10^{-4}$	$1.562\text{x}10^{-4}$
5	0.5	0.011	0.011	6.5	1.3	1.6	0.319	0.044	$7.326\text{x}10^{3}$	$5.864\text{x}10^{3}$

Table 2.2: Log-predicted properties. SD is the standard deviation of the log-predicted values for each lithologic class.

2.3.2 Calculating Formation Resistivity Factor

The formation resistivity factor F is a sediment property (independent of fluid) that determines the ability for an electrical current to flow through pore space (discussed in more detail in Chapter 4). F can be predicted in clay-rich sediments using a modified Archie's equation (Tiab and Donaldson, 1996).

$$C_t^i = \frac{1}{R_t^i} = \frac{1}{F^i R_w (1 - V_{cl}^i)} S_w^2 + \frac{V_{cl}^i}{R_{cl}} S_w \qquad (2.4)$$

C_t: total conductivity value from log
R_t: total resistivity value
R_w: resistivity of water
R_{cl}: resistivity of pure clay
V_{cl}: clay volume
S_w: water saturation
F: formation factor
i: depth index

As input to Eqn. 4, we used the V_{cl} predicted from the gamma-ray log (Eqn. 2.1). Since we are only investigating sediments in the saturated zone, $S_w = 1$. We calculated R_w ˜ 18 Ω -m using the maximum total dissolved solids TDS (Hunter and Associates,1996) in Schlumberger chart equations (Schlumberger, 1991b, p. 5). The typical range in resistivities of clay is $1 \le R_{cl} \le 1000$ Ω-m; we found $R_{cl;}$ = 34 Ω -m was able to give us reasonable estimates of porosity (next section). The computed formation factor is plotted with depth below the water table in Figure 2.3. F is typically between 5 and 500 (M. H. Rider, 1986) in deep rocks, higher values indicating lower permeability.

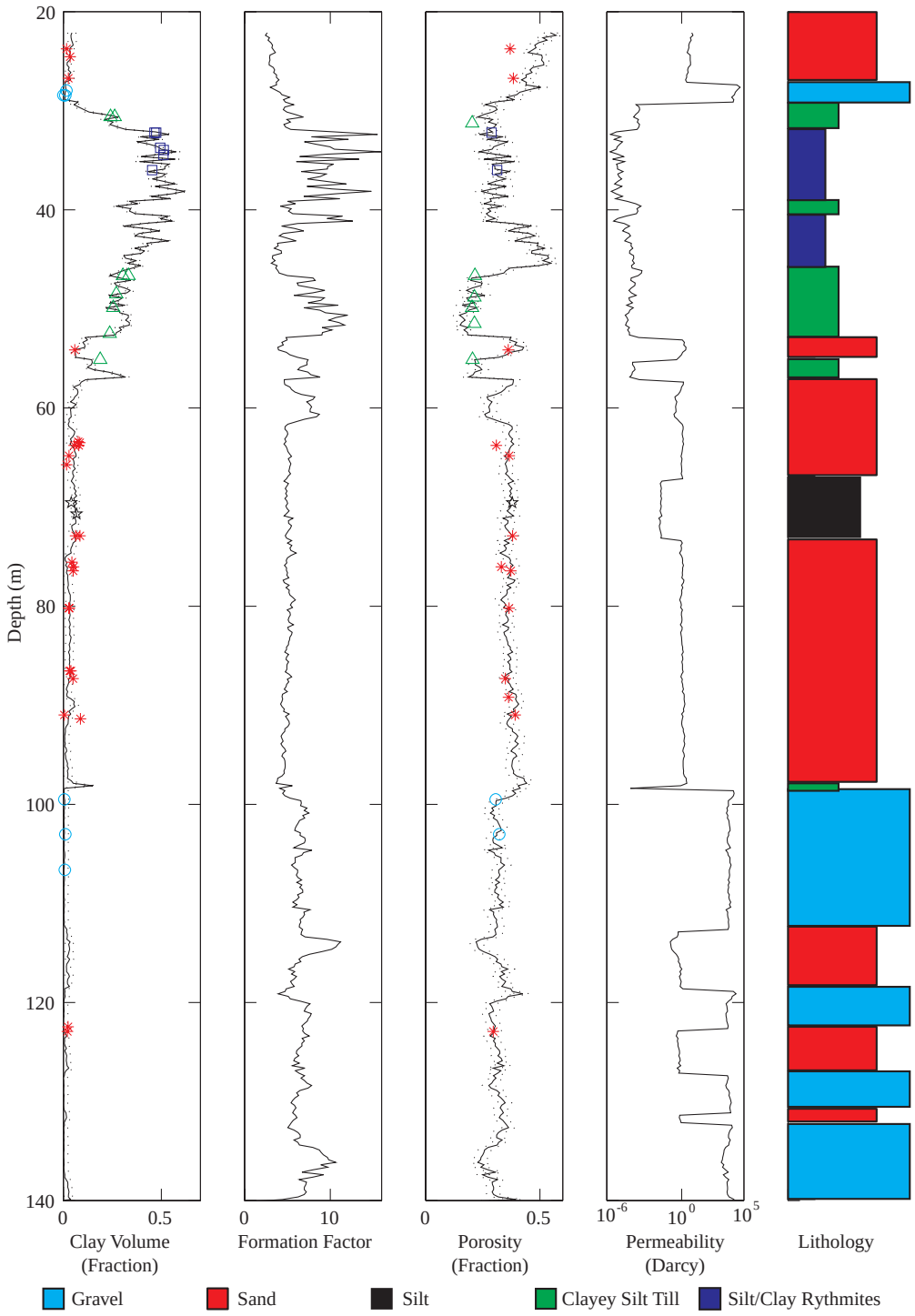

Figure 2.3: Predicted properties and lithology in the Aurora well, ORM. Symbols are the lab-measured values.

Eqn. 2.4 has been shown to work well (Schlumberger, 1989) for many clay-rich formations, independent of the distribution of the clays (dispersed, laminated or structural). When the clay fraction is zero, Eqn. 2.4 reduces to Archie's water saturation equation for clean sands, however, Eqn. 2.4 is not defined when $V_{cl} = 1$. Other resistivity models exist. However, we selected this model based upon its application to a variety of clay-content lithologies. The influences of clay on resistivity and formation factor are discussed in more detail in Chapter 4, Section 4.3.1.

The computed formation resistivity factor F values are within the range suggested by Schlumberger (1991a). Since F is related to pore structure, it is able to fairly clearly identify aquifers and aquitards in the Aurora well. For example, the clean sand aquifers in Figure 2.3 have lower F than the poorly sorted, silty, clay tills (Table 2.2). Since the conductivity reading is influenced by surrounding formations, the computed F very near the lithologic boundaries (as defined by the lithologic log) may be "smoothed".

The formation factor F values are dependent on the conductivity logger type, selected resistivity model, borehole completion, and clay type. Therefore, the Aurora F values can be compared to F values in similarly completed wells in the Oak Ridges Moraine where the same equation and logging tool (Geonics EM39) was used.

2.3.3 Predicting Porosity

Porosity is dependent on pore space characteristics, such as sorting, clay content, cementation and compaction. In the Aurora well, the well sorted sands and silts have high porosities (see Table 2.1), the silt/clay rythmites and gravels have medium porosities and the poorly sorted clayey/silt tills have low porosities.

To predict porosity from formation factor in the Aurora well, we took two steps. First we derived cementation factors for each lithologic ID index (Table 2.1) that relate the formation factor and lab-measured porosity. Second, we predicted porosity throughout the entire well using the cementation factors and the formation factor pseudo-log.

Step 1: Derive Cementation Factors

For each lithologic ID index, we derived the cementation factor m in the generalized Humble equation (Winsauer et al, 1952) theoretical relationship between total porosity and formation factor:

$$\phi^{i,j} = \left(\frac{a^j}{F^i} \right)^{\frac{1}{m^j}} \tag{2.5}$$

F: formation resistivity factor
ϕ: total porosity fraction
m: cementation factor
a: internal geometry parameter
i: depth index
j: lithologic ID index

Some suggested values for a and m are (1) $a = 0.62$ and $m = 2.15$ for sands and sucrosic rocks, (2) $a = 1$ and $2.2 \leq m \leq 3$ in ooliclastic rocks, (3) $a = 1$ and $1.4 \leq m \leq 2.8$ for compacted sediments, siliciclastic rocks and chalky rocks (Schlumberger, 1991a; Schlumberger,1991b), and (4) $a = 1.13$ and $m = 1.73$ in sandstone (Tiab and Donaldson, 1996). Archie's equation ($\phi = 1/F^{1/m}$) is a special case of Eqn. 2.5 where $a = 1$.

We began by trying the empirical Humble formula ($\phi = 0.62/F^{2.15}$), however it did not predict the lab-measured porosities well (total error = ± 5.1% total porosity). Then we used Archie's formula and selected $m \geq 1$ that minimized the error e (Eqn. 2.3) between the log-predicted and lab-measured porosities (results in Table 2.2). Using this derived m value in Eqn. 2.5, we computed the total error (± 2.9% total porosity) as the standard deviation of the absolute residuals between log-predicted and lab-measured porosity. From Eqn. 2.5, we assumed the effective porosity (from the lab) and the total porosity (from the log) are nearly equal since we didn't have a way for converting between the two.

Step 2: Predict Porosity

We used the lithologic log (ID indices with depth) to select the derived cementation factor m (Table 2.2), then used the empirical Eqn. 2.5 to predict the porosity ϕ throughout the Aurora well below the water table. The predicted and lab-measured porosities and the total error are plotted with depth in Figure 2.3.

Discussion

The derived cementation factor values *m* (Table 2.2) are within the expected range for unconsolidated sediments. The sands, silts and gravels are all very loosely consolidated and share the same derived cementation factor, yet the values are higher than those in the very densely compacted tills. This discrepancy my be explained by (1) the effective porosity (lab-measured) and total porosity (Eqn. 2.5) not being equal in the compacted tills, (2) poorly constrained cementation factors (too few lab-measured porosities for each lithology), or (3) the influence of other properties on the cementation factor (grain shape, sorting, compaction, pore size, tortuosity, and the locations of clay).

The log-predicted porosity fits the lab-measured porosity data and the lithologic log (Figure 2.3) very well, which is expected since the empirical parameters were calibrated using the lab-measured porosity data. Because of anomalously high conductivity values, the porosity is over-predicted in the upper sand aquifer (22 – 28 m) and in part of the silt/clay rythmite series (42- 47 m). These anomalously high conductivities may be due changes in the water conductivity or in the borehole condition. The scatter between 30 and 40 m depth in the porosity pseudo-log is a response to either the clay and silt rythmite series or scatter in the clay volume from noise in the gamma-ray log. Contrary to some porosity models, the lab-measured porosity is not influenced by the decrease in the clay fraction with depth in the poorly sorted, clayey, silt till from (47 – 53 m); this may occur if sorting is controlling porosity in these units. The log-predicted porosity mean and standard deviation (Table 2.2) match the lab-measured sample statistics (Table 2.1) very well for each lithology except for the clay/silt rythmite series.

2.3.4 Calculating Permeability

Permeability is a function of the amount, size and type of interconnected pore space of a material. In the ORM complex, well sorted sands and gravels (see Table 2.1) are aquifers and poorly-sorted clayey silt tills and silt/clay rythmites are aquitards,which suggests that sorting and clay content strongly influence permeability in the ORM. Since

the formation factor is a measure of the inability for a electrical current to flow through pore space, it can be used together with grain size information to predict permeability.

We used a statistical relationship between permeability and formation factor, grain size and sorting (Hutchinson et al, 1961) to calculate permeability in the Aurora well.

$$k^{i,j} = B_1 \left(\frac{d^j}{F^i e^{0.6\sigma^j}} \right)^{B_2} \qquad (2.6)$$

k: permeability (Darcy)	B_1: empirical constant
F: resistivity formation factor	B_2: empirical constant
σ: standard deviation $\log_2$ grain sizes	i: depth index
d: grain size (mm)	j: lithologic ID index

We assumed $B_1 = 2.53 \times 10^5$ and $B_2 = 2.75$, as was derived in unconsolidated sands (Hutchinson et al, 1961). For each lithologic class, we used the average lab-measured grain size and sorting (Table 2.1) and the formation factor pseudo-log to calculate permeability throughout the entire Aurora well column (Figure 2.3).

The predicted permeabilities (Table 2.2) are within the range of published permeabilities (Figure 2.4) for each of the different lithologies (Freeze and Cherry, 1979), however, we do not have lab-measured permeabilities to compare with the predicted at this time. High permeabilities were predicted in the sand and gravel aquifers (Figure 2.3) and very low permeabilities were predicted in the till and rythmite aquitards.

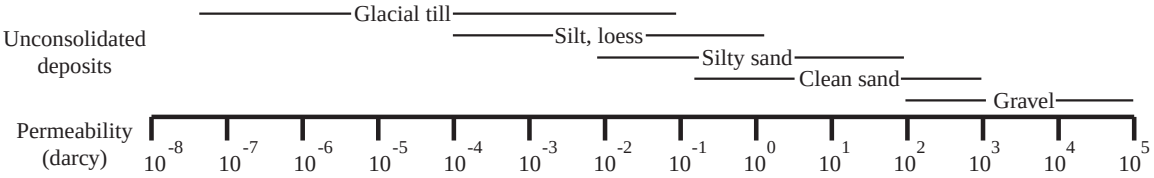

Figure 2.4: Published permeability ranges. Re-created from Freeze and Cherry (1979).

Permeability may be controlled by grain size and sorting in shallow unconsolidated aquifer environments where cementation and fracturing do not occur. This method of predicting permeability based on grain size data and formation factor could prove to be extremely valuable in shallow unconsolidated aquifer environments.

2.4 Results

- Clay volume (± 2.1%) and porosity (± 2.9%) were predicted very well and aquifers identified in the Aurora well.

- Known aquifers and aquitards were clearly identified.

- The cementation factors of each lithology were: m = 1.6 in the sands, silts and gravels; m = 1.8 in the silt/clay rythmite series; and m = 1.3 in the poorly sorted, clayey silt tills.

2.5 References

Freeze, R. A. and Cherry, J. A., 1979, *Groundwater*, Prentice-Hall, Inc, Englewood Cliffs.

Hunter and Associates and Raven Beck Environmental Ltd., 1996, Hydrogeologic evaluation of the Oak Ridges Moraine area, *Executive Summary*, Background Report No. 3 for the Oak Ridges Moraine Planning Study.

Hunter, J.A., Pullan, S.E., Burns, R.A., Good, R.L., Harris, J.B., Pugin, A., Skvortsov, A., and Gorianinov, N.N., 1998, Downhole seismic logging for high resolution reflection surveying in unconsolidated overburden, *Geophys.*, Vol. 63, No. 4, p. 1371-1384.

Hutchinson, C. A., Dodge, C. F. and Polasek, T. L., 1961, Identification and prediction of reservoir nonuniformities affecting production operations, *Soc. Petrol. Engr. JPT*, March.

Pullan, S. E., Pugin, A., and Sharpe, D. R., 1997, Seismic facies and regional architecture of the Oak Ridges Moraine area, *Water Resources Investigations of the Oak Ridges Moraine: Geology and Hydrogeology*, Russell, H. A. J., Sharpe, D. R., Hinton, M. J., and Johnson, F., Eds., Geological Survey of Canada Open File 3540, p. 32.

Rider, M. H., 1986, *The Geological Interpretation of Well Logs*, Revised Edition, Whittles Publishing, Caithness.

Russell, H. A. J., Logan, C., Brennand, T. A., Hinton, M. J., and Sharpe, D. R., 1996, Regional geoscience database for the Oak Ridges Moraine project (southern Ontario), *Current Research* 1996-E, Geological Survey of Canada, p. 191 - 200.

Schlumberger,1991a, *Log Interpretation Principles/Applications*, Schlumberger Educational Services, Houston.

Schlumberger,1991b, *Log Interpretation Charts*, Schlumberger Educational Services, Houston.

Sharpe, D. R., Dyke, L. D., Hinton, M. J., Pullan, S. E., Russell, H. A. J., Brennand, T. A., Barnett, P. J., and Pugin, A., 1996, Groundwater prospects in the Oak Ridges Moraine area, southern Ontario: applications of regional geological models, *Current Research* 1996-E, Geological Survey of Canada, p. 181 - 190.

Tiab, D. and Donaldson, E. C., 1996, *Petrophysics: Theory and Practice of Measuring Reservoir Rock and Fluid Transport Properties*, Gulf Publishing Co., Houston, Texas.

Winsauer, W.O., Shearin, H.M. Jr., Masson, P.H., and Williams, M., 1952. Resistivity of Brine-Saturated Sands in Relation to Pore Geometry. *Bull., AAPG*, 36, 2, 253-277.

CHAPTER 3: The Channel Porosity – Total Porosity Relationship Defined Physically, Hydraulically, Electrically, and Elastically

3.1 Introduction

A crucial prerequisite to modeling groundwater flow and contaminant transport is the development of characteristic porosity and permeability maps, which is the primary goal of aquifer and reservoir characterization. A formation's permeability, the ability for fluid to flow through the formation, depends on the amount of pore space that is available for flow; this portion of the pore space is called the channel porosity, also known as effective, free and flowing porosity. In natural rocks and sediments, the channel porosity is less than the total porosity since dead-end traps exist in the pore space; this portion of the pore space is called the trapped porosity. The amount of trapped porosity in a formation depends on the formation's pore space characteristics; i.e. sorting, compaction, dispersed clay volume and cementation. Since the total porosity is the sum of the channel and trapped porosities, total and channel porosities can be related by the formation's pore space characteristics.

As discussed in Chapter 2, a common problem encountered when comparing lab-measured channel porosity data with resistivity data is that the most commonly used resistivity – porosity relationship, Archie's equation, is a function of total porosity, not channel porosity. Therefore, the lab-measured channel porosity is commonly assumed equal to the total porosity, a poor assumption in many materials. The channel – total porosity relationship developed within this chapter can be particularly useful for converting between channel and total porosities in such cases.

We found that (1) there are three total porosity regions that are distinctly different physically, hydraulically, electrically and elastically, (2) these three porosity regions are defined by the formation's porous percolation threshold and critical porosity, (3) the total porosity - channel porosity relationship is different in each porosity region, and (4) Archie's exponent *m* defines the amount of trapped porosity in a formation for porosities between the percolation threshold and critical porosity. Topics in this chapter provide background for the following two chapters on electrical resistivity and seismic velocity.

3.2 Background

3.2.1 Background on Defining Porosity Type

The total (or absolute) porosity ϕ is the sum of the channel ϕ_{ch} (or effective, or flowing, or free), trapped ϕ_{tr} (or stagnant, or residual) and isolated ϕ_i (or vuggy) porosities (Figure 3.1.a).

$$\phi = \phi_{ch} + \phi_{tr} + \phi_i \tag{3.1}$$

Total porosity can be measured in the lab using granular density data or estimated in the field using sonic or density logs. The channel porosity, the pore volume available for electrical and hydraulic flows, can be measured in the lab using helium or mercury injection or estimated in the field using electrical techniques. Trapped and isolated porosities are very difficult to measure directly, but can be estimated in the lab using grain density and channel porosity data. Isolated porosity, however, is insignificant in most clastic sediments ($\phi_i \approx 0$), with the exception of those with shale fragments or basalt-derived grains.

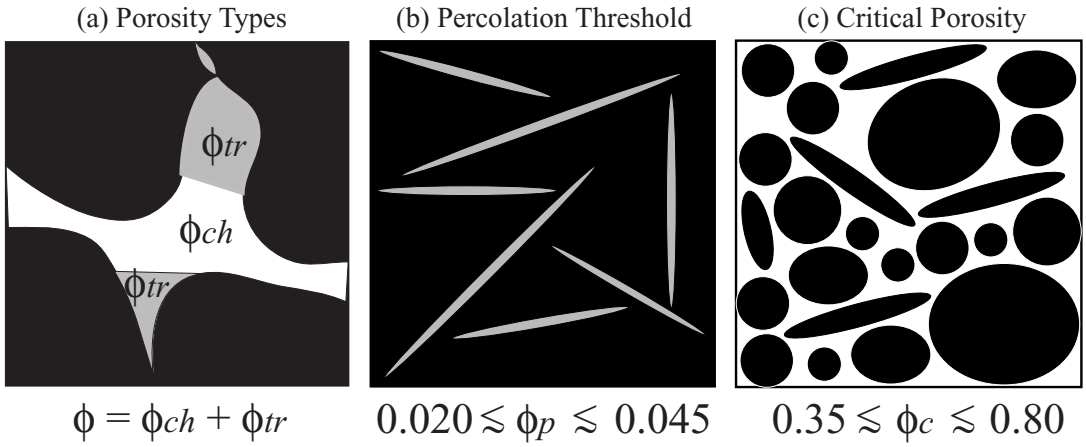

Figure 3.1: Pore space schematics. Schematic of (a) porosity type, (b) porosity percolation threshold and (b) granular critical porosity. Channel (white), trapped (gray) and isolated (gray) porosities. Granular region is shown in black.

As demonstrated in Figure 3.2, there is an apparent dependence of a clastic sediment's total porosity range on grain size; i.e. gravels have a narrower and lower porosity range than clays. The high porosity limit of a sediment's total porosity range, also known as critical porosity (discussed in the next section), occurs when the grains are randomly-oriented and loose. The low porosity limit, on the other hand, occurs when the same grains are packed as tightly as physically possible.

In nature, different grains weather differently depending on their mineralogy, thus have different characteristic shapes and sizes. Grain shape can be defined by its sphericity, roundness and texture. The sphericity of sand-size and smaller grains is mainly a function of the original mineral form, whereas the sphericity of pebble-size and larger grains is mainly a function of the transport process and duration (Boggs, 1987). The roundness of sand-size and smaller grains is primarily a function of mineralogy; i.e. hard quartz sand grains are rounded less readily than soft feldspar sand grains during transport. And, pebble-size and larger grains tend to be more easily rounded than smaller ones (Boggs, 1987). Regardless of mineralogy, however, small grains have larger specific surface areas, thus greater cohesive forces (Gueguen and Palciauskas, 1994) than large grains.

In summary, in a system of randomly-oriented loose grains, small platy grains (i.e. clays) have a higher porosity limit than a system of larger more spherical ones (i.e. eolian sands). In a system of well-sorted grain pack, platy grains have greater available grain-to-grain contact area, therefore can reach tighter packing than a system of more spherical grains.

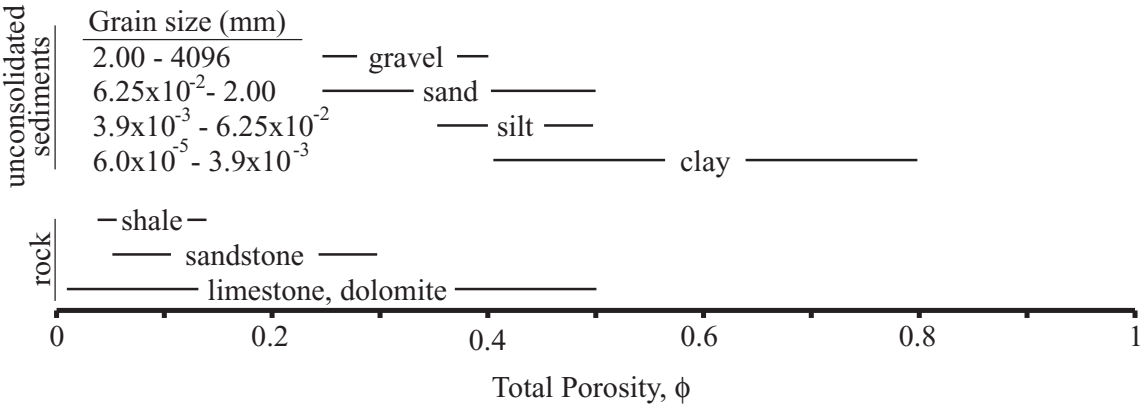

Figure 3.2: Observed total porosity ranges and grain size classes. Observed total porosity ranges for unconsolidated sediments and sedimentary rocks (Freeze and Cherry, 1979). Also shown are the ranges in grain sizes for gravel, sand, silt and clay grain-size classes (Boggs, 1987).

3.2.2 Percolation Threshold Theory Background

Extensive theory has been developed to define the inclusion volume fraction at which randomly oriented inclusions, whether pores or grains, are no longer connected; this volume fraction is known as the inclusion percolation threshold f_p (Webman et al, 1976, 1977; Straley, 1978; discussed in Gueguen and Palciauskas, 1994). The porous percolation threshold ϕ_p is defined by the porosity at which the pores are no longer connected; at $\phi < \phi_p$, $\phi = \phi_{tr}$ and $\phi_{ch} = 0$. The granular percolation threshold ϕ_c, also known as critical porosity, is the porosity at which grains are in suspension; at $\phi > \phi_c$, $\phi = \phi_{ch}$ and $\phi_{tr} = 0$.

The inclusion percolation threshold can be defined solely in terms of the inclusion depolarizing factor L_i of each principal axes i of the ellipsoidal inclusion. The

depolarizing factors are functions of the ellipsoid length ratios between the principal axes (Landau and Lifshitz, 1960; Mendelson and Cohen, 1982), but they are not functions of the inclusion size itself. The depolarizing factors are constrained by

$$0 \le L_j \le 1 \qquad (3.2)$$
$$L_1 + L_2 + L_3 = 1$$

For the special case of spheroidal inclusions (L_2=L_3) (Landau and Lifshitz, 1960) the depolarizing factors can be simplified to a general depolarizing factor term L where

$$L = L_1 \text{ and } L_2 = L_3 = \tfrac{1}{2}(1 - L) \qquad (3.3)$$

Landau and Lifshitz (1960) showed that the general depolarizing factor L is a function of the inclusion eccentricity e, where $e = \left|1 - \alpha^2\right|^{1/2}$. The inclusion aspect ratio α is equal to the ratio of the axis of symmetry b_2/b_1 where b_1 and b_2 are lengths in x_1 and x_2 directions. For prolate spheroids, $\alpha < 1$ (approaching disk-shape) and

$$L = \frac{1 - e^2}{2e^3}\left(\ln\frac{1+e}{1-e} - 2e\right) \qquad (3.4)$$

For oblate spheroids, $\alpha > 1$ (approaching needle-shape) and

$$L = \frac{1 - e^2}{e^3}\left(e - \tan^{-1} e\right) \qquad (3.5)$$

For spheres, α = 1 and L = 1/3. Norris et al (1984) showed that the percolation threshold of spheroids can be expressed as

$$f_p = 1 - \frac{(1+L)(1+3L)}{1+9L} \qquad (3.6)$$

The inclusion percolation threshold f_p, the inclusion volume fraction at which inclusions become disconnected, is 1/3 for spherical, 1/5 for disk-shaped, and 0 for needle-shaped inclusions. Both the porous percolation threshold ($\phi_p = f_p$) and the granular percolation threshold (ϕ_c = 1 - f_p) can be determined experimentally using electrical techniques.

The porous percolation threshold ϕ_p is defined in a system of insulating grains and conductive fluid by the porosity at which an electrical current does not transmit through

the pore space. The hydraulic percolation threshold occurs at very low porosity fractions in natural rocks; 0.025 in Fontainebleau sandstone, 0.035 in fused glass beads, and 0.045 in hot-pressed calcite (Mavko and Nur, 1997). According to percolation theory, these results suggest that pores are nearly needle-shaped at very low porosities. Sen et al (1981) and Webman et al (1975) found $0.135 \leq \phi_c \leq 0.250$ using a modified Archie's equation (Eqn. 4.13) and numerical modeling.

The granular percolation threshold ϕ_c is defined in a system of conductive inclusions (representing grains) and insulating fluid by the granular volume fraction at which the grains become suspended and an electrical current does not transmit through the granular system. Nur et al (1995) demonstrated the influence of ϕ_c on elastic properties; acoustically derived ϕ_c values range between 0.40 and 0.65 for various unconsolidated materials (Mavko et al, 1998). ϕ_c likely decreases in a material as a result of increased grain sphericity and grain smoothness. Even though sediments are grain-supported in static environments, not suspended, the ϕ_c of a material provides *tremendous* insight into the electrical resistivity – porosity (Chapter 4) and acoustic velocity – porosity relationships (Chapter 5).

3.2.3 Background on Channel Porosity – Total Porosity Relationships

Since hydraulic permeability is a function of channel porosity, several authors have developed relationships to convert between total and channel porosities. Gal et al (1998) used lab-measured total and trapped porosity data (Figure 3.3) in the Fontainebleau sandstone (Bourbie and Zinszner, 1985) to derive the following empirical relationship

$$\phi_{ch} = 1.3486(\phi - 0.021)^{1.4} \tag{3.7}$$

As seen in Figure3.3, according to Eqn. 3.7, $\phi_{ch} \approx 0$ for $\phi < 0.021$ and $\phi_{ch} \approx \phi$ at $\phi \approx 0.54$. Perez-Rosales (1982), however, discussed the relationship between total and channel porosities in terms of the total porosity term in Archie's equation (Eqn. 4.13).

$$\phi_{ch} = \phi^m \tag{3.8}$$

The cementation exponent m (discussed in Section 3.2.3) is high in composites where the pore space is discontinuous and disconnected, which translates to high amounts of ϕ_{tr}, where $\phi_{tr} = \phi - \phi_{ch}$. According to Eqn. 3.8, however, channel porosity should exist at porosities less than the composite's percolation threshold ϕ_p (Figure 3.3) and trapped porosity should exist even when grains are in suspension ($\phi > \phi_c$) (Figure 3.4), neither of which is observed.

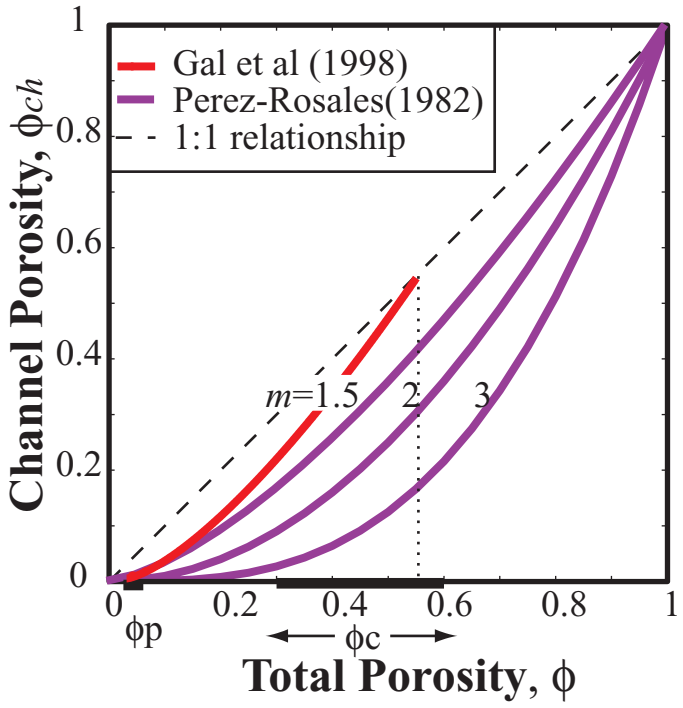

Figure 3.3: Channel and total porosities from previous work. Channel and total porosities according to Perez-Rosales (1982) (Eqn. 3.8)and Gal et al (1998) (Eqn. 3.7).

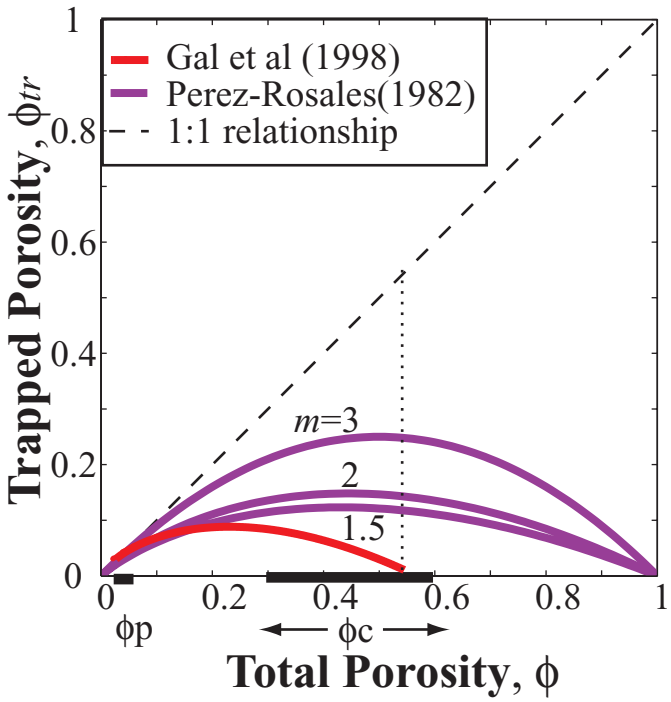

Figure 3.4: Trapped and total porosities from previous work. Trapped and total porosities according to Perez-Rosales (1982) (Eqn. 3.8) and Gal et al (1998) (Eqn. 3.7).

Sen et al (1979) suggested modifying the porosity term in Archie's equation to account for the percolation threshold by $(\phi - \phi_p)^m$ (Chapter 4, Section 4.2.3). If the porosity term in Archie's equation is equal to the channel porosity like Perez-Rosales (1982) suggested, then the channel porosity could be expressed as

$$\phi_{ch} = (\phi - \phi_p)^m \tag{3.9}$$

The modification of the porosity term made by subtracting the percolation threshold is similar to the modification in the Kozeny-Carman equation for permeability by Mavko and Nur (1997), which is of the form $(\phi - \phi_p)^x$. The percolation threshold term in Eqn. 3.9 has a minimal effect on ϕ_{ch} at high ϕ values.

3.3 New Results on the Channel Porosity – Total Porosity Relationship

3.3.1 Three Distinct Porosity Regions Defined Physically, Hydraulically, Electrically and Acoustically

The granular and porous percolation thresholds (Section 3.2.2) together define three distinct porosity regions physically, hydraulically, electrically and elastically. Physically, these three porosity regions are defined by the amounts of channel porosity ϕ_{ch} and trapped porosity ϕ_{tr}. Hydraulically and electrically, the regions are defined by the ability for fluid and currents to flow through the pore space. Acoustically, the regions are defined by the pore space stiffness and rigidity that contributes to the system as a whole.

Region I is defined for porosities less than the porosity percolation threshold ($\phi < \phi_p$), where the pore space is no longer connected ($\phi_{ch} = 0$); all of the porosity is trapped ($\phi = \phi_{tr}$ from Eqn. 3.1). Electrical currents and fluids cannot flow through a system's pore space if porosities are lower than the percolation threshold since the pores aren't connected; in other words the system's formation resistivity factor immediately approaches infinity and the hydraulic permeability equals zero. Since fluids cannot escape from the pore space when an acoustic wave travels through the system (the system's pore pressure gradients are "unrelaxed"), the pore space is relatively stiff; the moduli of such low porosity materials are approximately equal those of the mineral constituent.

Region II is defined for porosities in between the porous percolation threshold and the critical porosity ($\phi_p \leq \phi \leq \phi_c$), where the total porosity is connected but trapped porosity exists ($\phi = \phi_{ch} + \phi_{tr}$ from Eqn. 3.1). Since not all of the porosity is available for flow in this region, the abilities for electrical currents and fluids to flow depend on the amount of trapped porosity. The amount of trapped porosity depends on the formation's pore space characteristics; i.e. sorting, cementation, compaction and dispersed clay content. These same pore space characteristics control the empirical, formation-specific parameters B in

the Kozeny-Carman relation for permeability (Mavko and Nur, 1998) and a_H and m in the Humble equation (Eqn. 4.13) for formation factor (Table 3.1). These pore space characteristics also influence the system's stiffness K, rigidity μ and density ρ; hence they influence the system's acoustic velocities (Table 3.1). The influences of these pore space characteristics on the ϕ_{ch} - ϕ relationship are discussed in Section 3.3.4.

Region III is defined for porosities greater than the critical porosity where grains are in suspension and all of the pore space is not only connected, but is also available for flow ($\phi_{tr} = 0$, so $\phi = \phi_{ch}$ from Eqn. 3.1). Since all of the porosity is available for flow, the permeability is infinite and the formation factor only depends on the total porosity (Table 2.1), not on other properties such as sorting, clay content, or grain shape. A system of suspended grains lacks rigidity ($\mu = 0$) and is highly compressible (low K), therefore in this region, the effective bulk modulus K is dominated by the fluid modulus K_w.

Region	Porosity Range	Permeability	Resistivity	P-wave Velocity
I	$0 \le \phi < \phi_p$	0	$f(R_m)$	$f(V_{p\text{-}m})$
II	$\phi_p \le \phi \le \phi_c$	$f(\phi, B)$	$f(\phi, a_H, m)$	$f(\phi, K_i, \mu_i, \rho_i)$
III	$\phi_c < \phi \le 1$	$f(\phi, B)$	$f(\phi, R_i)$	$f(\phi, K_i)$

Table 3.1: Three distinct porosity regions defined hydraulically, electrically and elastically. Defined by the percolation threshold ϕ_p and critical porosity ϕ_c.

3.3.2 New Channel Porosity – Total Porosity Relationship

As discussed in Section 3.2.2 above, the percolation threshold ϕ_p and critical porosity ϕ_c define three distinct $\phi_{ch} - \phi_{tr}$ porosity regions (Table 2); $\phi_{ch} = 0$ in Region I, $\phi_{tr} = 0$ in Region III, and both ϕ_{ch} and ϕ_{tr} exist in Region II. This section focuses on developing a relationship that describes how ϕ_{ch} and ϕ_{tr} are controlled in the Region II ($\phi_p \le \phi \le \phi_c$), the porosity range of most rocks and sediments. In Region II, a composite's characteristic hydraulic permeability k and formation resistivity factor F are functions of the composite's channel porosity ϕ_{ch}, whereas its characteristic elastic moduli K and μ are functions of the composite's total porosity ϕ. The total porosity is the sum of channel and

trapped porosities (Eqn. 3.1), assuming isolated porosity is negligible (ϕ_i = 0). A composite's trapped porosity is a function of the pore space characteristics and can be described by Archie's exponent *m* (discussed in Section 3.3.4 below and in Chapter 4, Section 4.2.3). The $\phi_{ch} - \phi$ relationship, which is based upon the pore space characteristics, provides the link between *k*, *F*, *K* and μ, an extremely valuable link for groundwater, petroleum and geotechnical engineers.

From Section 3.3.1 above, we know that the channel porosity is zero at the percolation threshold (the low porosity limit) and equal to the total porosity at the critical porosity (the high porosity limit). The porosity term proposed by Sen et al (1979) accounts for the low porosity limit, but as seen in Figure 3.4, it suggests that significant trapped porosity exists when the composite is a suspension, which does not meet the high porosity limit. The high porosity limit can be account for by multiplying Eqn. 3.9 by a formation-specific parameter *A*, which is defined by the composite's percolation threshold ϕ_p and critical porosity ϕ_c.

$$\phi_{ch} = A\left(\phi - \phi_p\right)^m \tag{3.10}$$

$$A = \frac{\phi_c}{(\phi_c - \phi_p)^m} \tag{3.11}$$

As seen in Figure 3.5, *A* significantly influences the ϕ - ϕ_{ch} relationship, especially at high porosities. Eqn. 3.10 is of the same form as that empirically derived by Gal et al (1998) (Eqn. 3.7). The ϕ_p, ϕ_c and *m* values characteristic of the Fontainebleau sandstone can be solved for in Eqn. 3.7 by Eqn. 3.10; ϕ_p = 0.021, ϕ_c = 0.54, and *m* =1.4 (Figure 3.5).

Region	Porosity Range	Channel Porosity, ϕ_{ch}	Trapped Porosity, ϕ_{tr}
I	$0 \le \phi < \phi_p$	0	ϕ
II	$\phi_p \le \phi \le \phi_c$	$A\left(\phi - \phi_p\right)^m$	$\phi - A\left(\phi - \phi_p\right)^m$
III	$\phi_c < \phi \le 1$	ϕ	0

Table 3.2: Three porosity regions defined physically. Defined by the percolation threshold ϕ_p and critical porosity ϕ_c in terms of channel and trapped porosities.

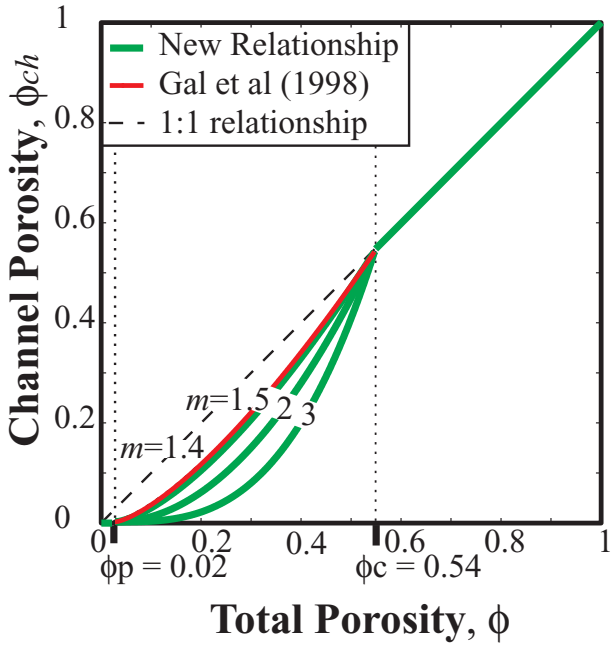

Figure 3.5: Channel and total porosities using new relationship. Channel and total porosities according to Eqns. 3.10 and 3.11 and Gal et al (1998) (Eqn. 3.7).

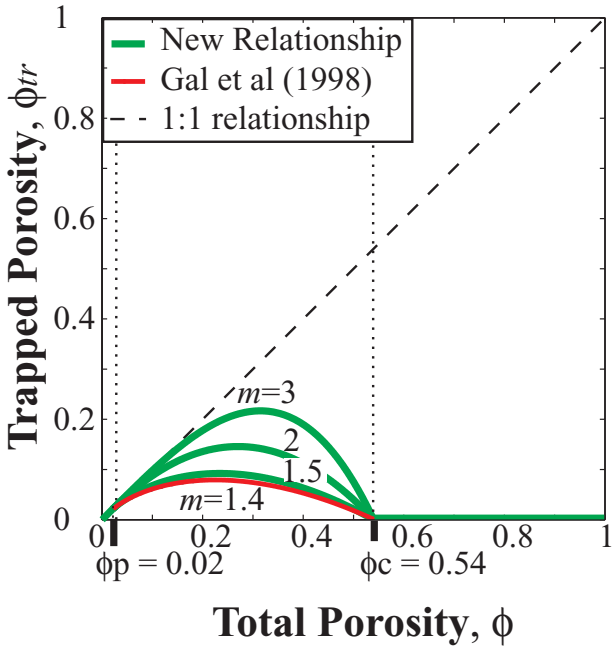

Figure 3.6: Trapped and total porosities using new relationship. Trapped and total porosities according to Eqns. 3.10 and 3.11 and Gal et al (1998) (Eqn. 3.7).

3.3.3 Insight into Empirical Parameters in Formation Factor and Permeability Equations

As discussed earlier in this chapter, both formation resistivity factor F and hydraulic permeability k are controlled by the ability for electrical currents and fluids, respectively, to flow through a formation's pore space; the formation's channel porosity ϕ_{ch} defines the pore space available for flow. Forms of both the Humble (Winsauer et al, 1952) and the Kozeny-Carman (Kozeny, 1927 and Carman, 1937) equations are by far the most widely used empirical $F - \phi$ and $k - \phi$ relationships, respectively. Each relationship has formation-specific empirical parameters and a formation-specific exponential porosity term of the form of Eqn. 3.10.

Equation 3.10 suggests that the formation-specific A term is absorbed into the empirical, formation-specific a_H term in the Humble equation (Eqn. 4.14) modified by Sen et al (1979). In fact, in Section 4.3.3 of Chapter 4, we show just that; a_H can be expressed as a function of A (Eqn. 4.19).

Mavko and Nur (1997) modified the porosity term in the Kozeny-Carman equation for permeability by subtracting the percolation threshold from the total porosity. The modification is of the form $\left(\phi - \phi_p\right)^x$, where $x \approx 3$ in cemented rocks. If it is assumed that $x \approx m$ in Eqn. 3.10, then the A term is likely adsorbed into the empirical, formation-specific parameter B in the Kozeny-Carman equation.

3.3.4 The Influence of Pore Space Characteristics on Channel and Trapped Porosities

In the porosity region $\phi_p \leq \phi \leq \phi_c$ (Region II), the channel porosity ϕ_{ch} and total porosity ϕ can be influenced by several pore space characteristics such as sorting, cementation, compaction, and dispersed clay volume. When a material of a given volume fills the pore space of a composite, the composite's total porosity decreases by an amount equal to the volume of the pore-filling material. The degree of influence of the

pore-filling material on trapped and channel porosities, however, is defined by the parameter *m* in Eqn. 3.10. For example, in two different composites with the same total porosity, the trapped porosity of a poorly sorted composite will be less (low *m* value) than that in a cemented one (high *m* value) where pore throats become sealed and trapped. Decades of observations show that *m* tends to be largest when porosity decreases from cementation, smallest when it decreases from sorting and somewhere in between when it decreases from compaction and increased volume of pore-filling, dispersed clay (See Chapter 4, Section 4.2.3). The influences of the pore space characteristics on the $\phi_{ch} - \phi$ relationship are shown in Figure 3.7.

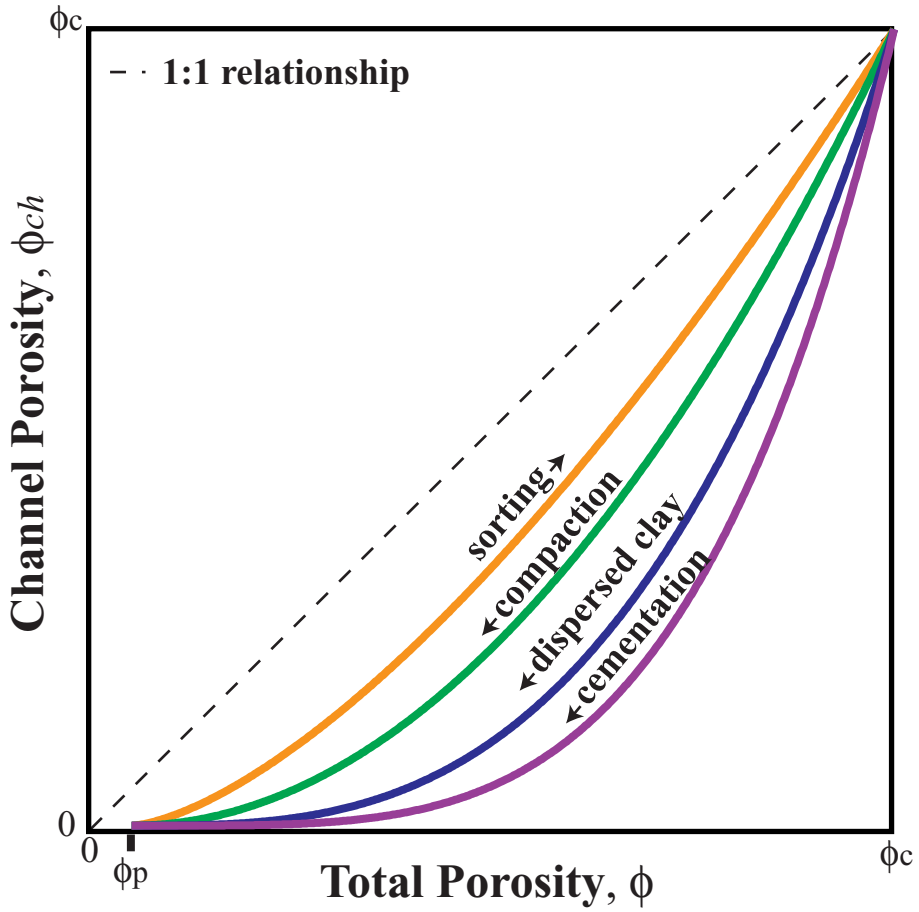

Figure 3.7: The influence of pore space characteristics on channel porosity. Arrows indicate increased sorting (reduced grain size distribution), compaction, pore-filling dispersed clay volume, and cementation.

3.4 Conclusions

- A formation's percolation threshold ϕ_p and critical porosity ϕ_c define three distinct porosity regions physically, hydraulically, electrically and elastically: $0 \leq \phi \leq \phi_p$ in Region I, $\phi_p < \phi < \phi_c$ in Region II, and $\phi_c \leq \phi \leq 1$ in Region III.

- A formation's trapped porosity ϕ_{tr} is controlled by the formation's pore space characteristics through Archie's exponent m.

- The $\phi_{ch} - \phi$ relationship for a formation is defined by the formation's characteristic ϕ_p, ϕ_c and m values.

- The formation-specific A term in the $\phi_{ch} - \phi$ relationship can be expressed solely as a function of ϕ_p, ϕ_c and m.

- The A term is adsorbed into the empirical, formation-specific parameters a_H and B in the Humble and Kozeny-Carman equations

3.5 References

Archie, G.E., 1942. The electrical resistivity log as an aid in determining some reservoir characteristics. *Trans. Am. Inst. Mech. Eng.,* 146, 54-62.

Bourbie, T., and Zinszner, B., 1985. Hydraulic and acoustic properties as a function of porosity in Fontainbleau sandstone. *J. Geophys. Res*., v. 90, 11,524 – 11, 532.

Boggs, S. Jr., 1987. *Principles of Sedimentology and Stratigraphy*. Merrill Publishing Company, Columbus, Ohio.

Carman, P.C., 1937. Fluid Flow through a granular bed. Trans. Inst. Chem. Eng. London, 15, 150 – 156.

Freeze, R.A. and Cherry, J.A., 1979. *Groundwater*. Prentice Hall, Englewood Cliffs, N.J.

Gal, D., Dvorkin, J., and Nur, A., 1998. A physical model for the porosity reduction in sandstones. *Geophys*., 63, 454 – 459.

Gueguen, Y., and Palciauskas V., 1994. *Introduction to the Physics of Rocks*. Princeton University Press, Princeton.

Kozeny, J., 1927. Uber kapillare Leitung des Wassers im Boden. Sitzungsber. Akad. Wiss. Wien., v. 136, 271 – 306.

Landau, L.D., and Lifshitz, E.M., 1960. *Electrodynamics of continuous media*. Oxford, Pergamon Press.

Mavko, G., and Nur, A., 1997. The effect of a percolation threshold in the Kozeny-Carman relation. *Geophys*., 1480 – 1482.

Mavko, G., Mukerji, T., and Dvorkin, J., 1998, *The Rock Physics Handbook: tools for seismic analysis in porous media*, Cambrige University Press.

Mendelson, K.S., and Cohen, M.H., 1982. The effect of grain anisotropy on the electrical properties of sedimentary rocks. *Geophys*., 47, 257 – 263.

Norris, A.N., Sheng, P., and Callegari, A.J., 1984. Effective-medium theories for two-phase dielectric media. *J. Appl. Phys*., 57, 1990 – 1996.

Nur, A., Mavko, G., Dvorkin, J., and Gal, D., 1995. Critical Porosity: The key to relating physical properties to porosity in rocks, in *Proc., 65th Ann. Int. Meeting, Soc. Expl. Geophys*., 878.

Perez-Rosales, C., 1982, On the Relationship Between Formation Resistivity Factor and Porosity, *Soc. Pet. Eng. J.*, 531-536.

Sen, P.N., Scala, C., and Cohen, M.H., 1981. A self-similar model for sedimentary rocks with application to the dielectric constant of fused glass beads. *Geophys.*, V. 46, N. 5, 781 – 795.

Straley, J.P., 1978. Critical phenomena in resistor networks. *J. Phys*., v. C9, 783 – 795.

Webman, I., Jortner, J., and Cohen, M.H., 1967. Numerical simulation of continuous percolation conductivity. *Phys. Rev*., V. B14, 4737 – 4740.

Webman, I., Jortner, J., and Cohen, M.H., Numerical simulation of electrical conductivity in microscopically inhomogeneous materials. *Phys. Rev*., v. B11, 2885 – 2892.

Webman, I., Jortner, J., and Cohen, M.H., 1977. Theory of optical and microwave properties of microscopically inhomogeneous materials. *Phys. Rev*., v. B15, 5712 – 5723.

Winsauer, W.O., Shearin, H.M. Jr., Masson, P.H., and Williams, M., 1952. Resistivity of Brine-Saturated Sands in Relation to Pore Geometry. *Bull., AAPG*, 36, 2, 253-277.

CHAPTER 4: Developments in the Electrical Resistivity – Porosity Relationship

4.1 Introduction

Electrical resistivity data are by far the most common geophysical data collected for environmental groundwater investigation. Since electrical currents respond to changes in a formation's electrical properties and pore-space characteristics, resistivity data are typically used to *qualitatively* interpret changes in fluid properties (i.e. freshwater versus contaminated water) and locate clay-rich formations (discussed in Chapter 1). Resistivity data, however, can also be used *quantitatively* to estimate porosity and permeability (discussed in Chapter 2). Channel porosity and permeability control hydraulic flow and are therefore the most important formation properties to estimate in order to characterize flow.

This chapter focuses on theoretically and empirically exploring the influence of a composite's pore space characteristics and electrical properties on resistivity. The most significant contributions of this work are the development of a tight upper bound on the formation factor – total porosity relationship, the generalization of the internal geometry parameter – cementation exponent relationship, and insight into determining formation pore space characteristics using formation factor – porosity data. As discussed in Chapter 2, a common problem encountered when analyzing resistivity – porosity data is determining formation-specific, empirical parameters a and m in the resistivity – porosity relationship. The developments within this chapter can be used to deal with such problems. These developments are valuable to both the environmental and petroleum industries for improving the characterization of aquifers and reservoirs.

A composite's electrical conductivity, the inverse of resistivity, is a measure of the ease for an electrical current to be transmitted (via electrons and ions) through the composite. Varying material properties are responsible for variations up to 20 orders of magnitude in the resistivity of sediments and rocks. The conductivity of a material is influenced by the conductivities of the mineral and fluid constituents and by the composite's formation resistivity factor, the inability for electrical flow through the pore space. Both conductivity and formation factor are influenced by formation anisotropies. The majority of common minerals are insulators (i.e. feldspars and quartz) (Parkhomenko, 1967), however, ore and clay minerals are conductive. Fluids such as oil, freshwater and gas are resistive, whereas brines can be highly conductive. Besides the influence of their electrical properties, liquids may additionally increase the mobility of the surface ions on insulators that have strong adsorption characteristics (Parkhomenko, 1967). Electrically, most sediments can be simplified as one of two mineral-fluid systems: (1) insulating minerals and pore-filling fluid, or (2) insulating minerals, conducting clay minerals, and pore-filling fluid (liquid or gas). Even though the data acquisition frequency and formation anisotropies can significantly influence resistivity measurements, the discussion of these topics is beyond the scope of this work.

Mineral/Fluid	Resistivity (Ω-m)
Water	10^{-2} - 10^{2} (2)
Quartz	$10^{14} – 10^{16}$ (1)
Calcite	$5 \cdot 10^{14}$ (1)
Whetted Clay	$1 – 10^{3}$ (2)

Table 4.1: Resistivities of common sediment constituents. (1) Parkhomenko (1967); (2) Rider (1986)

Theoretical effective medium bounds on resistivity are functions of the constituent's conductivities and volumes, whereas theoretical effective medium approximations additionally require grain geometry information. Theory has not been developed to describe the influence of various pore-space characteristics, such as cementation and tortuosity, on conductivity. For comprehensive discussion of various theories refer to Berryman (1995) and Mavko et al (1998).

Empirical relationships are valuable for determining the relationship between resistivity and porosity when the composite' granular geometries and mineral constituents are unknown. Most empirical relationships require true (measured) conductivity and the conductive constituent's conductivity and volume fraction. The influence of various pore space characteristics is accounted for in empirical parameters. For a review of empirical relationships refer to Tiab and Donaldson (1996), Schlumberger (1989) and Worthington (1985).

4.2 Background

4.2.1 Theoretical Resistivity Background

Hashin-Shtrikman Bounds

The theoretical Hashin-Shtrikman (HS) bounds for electrical conductivity (Hashin and Shtrikman, 1962) provide upper and lower limits for the resistivity-porosity relationship in a multi-constituent media. The upper HS bound on resistivity R_{HS+} is equal to the inverse of lower conductivity HS bound σ_{HS-}^{-1} and is a function of the individual constituent fractions f_i and conductivities σ_i.

$$R_{HS+}^{-1} = \sigma_{HS-} = \sigma_{\min} + A_- / (1 - \alpha_- A_-) \tag{4.1}$$

where

$$A_- = \sum_{i=2}^{N} f_i / \left[(\sigma_i - \sigma_{\min})^{-1} + \alpha_- \right]$$

$$\alpha_- = (3\sigma_{\min})^{-1}$$

and where $\sigma_{\min} = \sigma_1$ is the minimum conductivity ($\sigma_{\min} \le \sigma_i$) and N is the total number of constituents. The lower HS bound on resistivity R_{HS-} is equal to the inverse of the upper conductivity HS bound σ_{HS+}^{-1} and is

$$R_{HS-}^{-1} = \sigma_{HS+} = \sigma_{\max} + A_+ / (1 - \alpha_+ A_+) \tag{4.2}$$

where

$$A_+ = \sum_{i=1}^{N-1} f_i \Big/ \left[(\sigma_i - \sigma_{\max})^{-1} + \alpha_+ \right]$$

$$\alpha_+ = (3\sigma_{\max})^{-1}$$

The liquid component typically has the maximum conductivity where $\sigma_i \leq \sigma_{\max}=\sigma_N$. Both the upper and lower HS bounds satisfy the conditions that the resistivity R_{HS} equals the mineral resistivity R_m when the fluid fraction is zero ($\phi = 0$) and equals the fluid resistivity R_w when the mineral fraction is zero ($\phi = 1$) (Figure 4.1).

The upper HS resistivity bound corresponds to isolated conductive spheres (pores) covered by a resistive shell (mineral) (Mendelson and Cohen, 1982), a likely scenario for pumice and some basalts, but an unlikely one for granular materials. The lower HS resistivity bound corresponds to isolated resistive spheres (mineral) covered by a conductive shell (water and/or clay), a more likely model for sediments. This is schematically shown in Figure 4.1; the black regions represent the resistive constituent and the white region the conductive constituent. Notice that both the upper and lower HS bounds are approximately linear for porosities less than approximately 0.30.

The HS bounds can be used to determine a range in the fluid volume fraction ϕ for a given R/R_w or vice versa. Other bounding models exist, however the HS bounds provide the tightest bounds for an isotropic composite without specifying the geometries of the constituents. As seen in Figure 4.1, the bounds are very wide for constituents with extremely different conductivities (i.e. quartz sand – fluid system) and tight for constituents with very similar conductivities (i.e. clay – fluid system). The upper bound is insignificantly influenced by the fluid resistivity $R_w = \sigma_{max}$. The lower HS bound is essentially unaffected by the mineral resistivity $R_m = \sigma_{min}$ for $\phi > 0.01$ as long as R_m/R_w is approximately greater than 10^3. In fact, Berryman (1995) showed that the lower HS bound can be simplified as a function of the fluid resistivity R_w and volume fraction ϕ in systems of insulating spherical grains saturated by a conductive fluid.

$$\frac{R_{HS-}}{R_w} \approx \frac{3-\phi}{2\phi} = \frac{3}{2}\phi^{-1} - \frac{1}{2} \qquad (4.3)$$

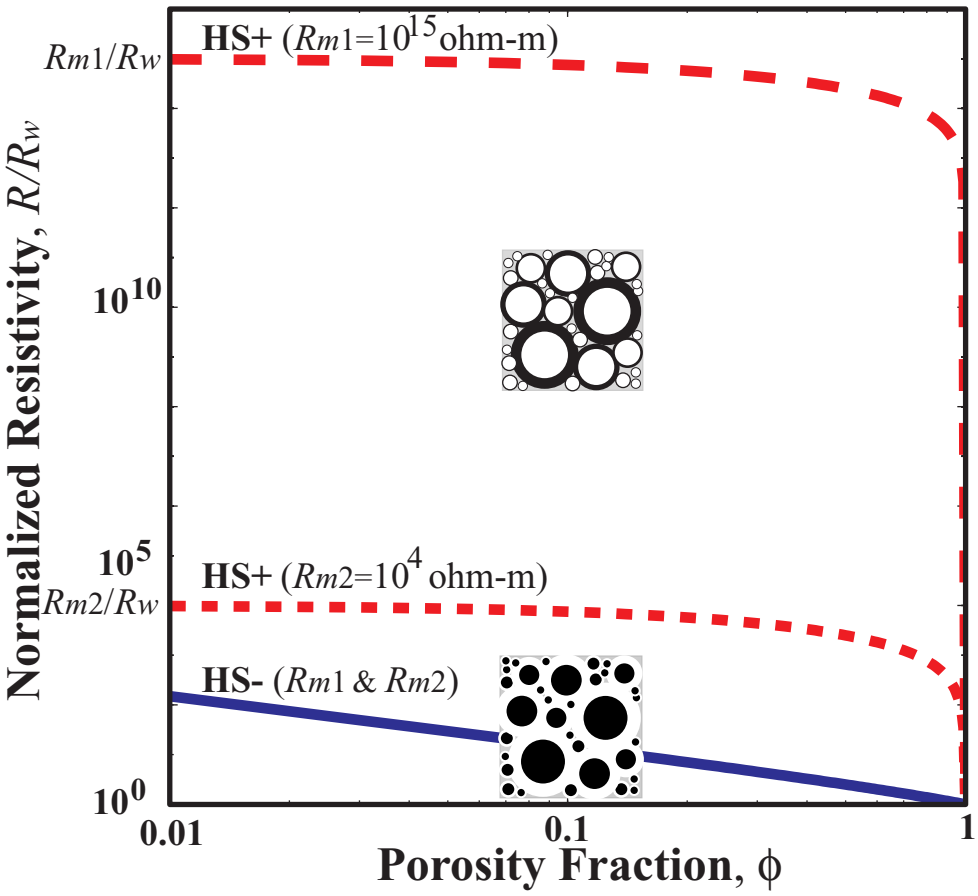

Figure 4.1: The Hashin- Shtrikman resistivity bounds. Example is for two systems saturated by a fluid with $R_w = \sigma_1^{-1} = 1$ Ω-m: $R_{m1} = \sigma_2^{-1} = 10^{15}$ Ω-m (dashed line) and $R_{m2} = \sigma_2^{-1} = 10^4$ Ω-m (short dashed line); the lower HS bound (bold solid line) is essentially the same at $\phi \geq 0.01$ for both systems. The black regions in the schematic sphere pack represent the resistive constituent and the white represents the conductive constituent.

Maxwell-Garnett Approximation

Maxwell (Bergman, 1978) derived a non-self-consistent theory for a system of suspended spheres, also known as the Maxwell-Garnett, Clausius-Mossotti and Lorenz-Lorentz equation. Fricke (1924) generalized the Maxwell-Garnett equation for dispersive systems spheroids. The theory describes the effective electrical conductivity σ_F^* as a function of the host volume fraction f_1, the inclusion shape parameter x, and the conductivity of the host σ_1 and of the spheroidal inclusions σ_2.

$$\frac{\sigma_F^*/\sigma_2 - 1}{\sigma_F^*/\sigma_2 + x} = f_1 \frac{\sigma_2/\sigma_1 - 1}{\sigma_2/\sigma_1 + x} \tag{4.4}$$

The inclusion shape parameter x is a function of the conductivity ratio σ_2/σ_1 and the aspect ratio α (or the depolarizing factors, L_i) (Section 3.2.2). The equations for x are given in Fricke (1924). When modeling a sediment or rock, the host is the fluid constituent and the inclusion is the granular constituent. However, since the MG theory describes systems of spheroids in suspension, it does not necessarily hold for systems where grains are in contact. In a system of resistive spheroidal inclusions ($\sigma_2 \approx 0$) suspended in a conductive fluid, the effective resistivity R_F increases as grain ellipticity.

$$\frac{R_F}{R_w} \approx \frac{(x+1) - \phi}{x\phi} = 1 + a_F \frac{1-\phi}{\phi} = a_F \phi^{-1} + (1 - a_F) \tag{4.5}$$

where

$$a_F = (x+1)/x \tag{4.6}$$

In a system of resistive inclusions, x is only a function of the aspect ratio α since $\sigma_2/\sigma_1 = 0$. Fricke (1924) showed that $x = 2$ for resistive spheres, $x \approx 1.39$ for high-sphericity sands, $x \approx 0.85$ for more angular sands (Figure 4.2), and approaches zero for penny-shaped resistive grains. Assuming that the maximum grain eccentricity is 0.95, Mendelson and Cohen (1982) showed that in a 2-D system of aligned grains the maximum a_H is approximately 10, which corresponds to $x \approx 0.095$.

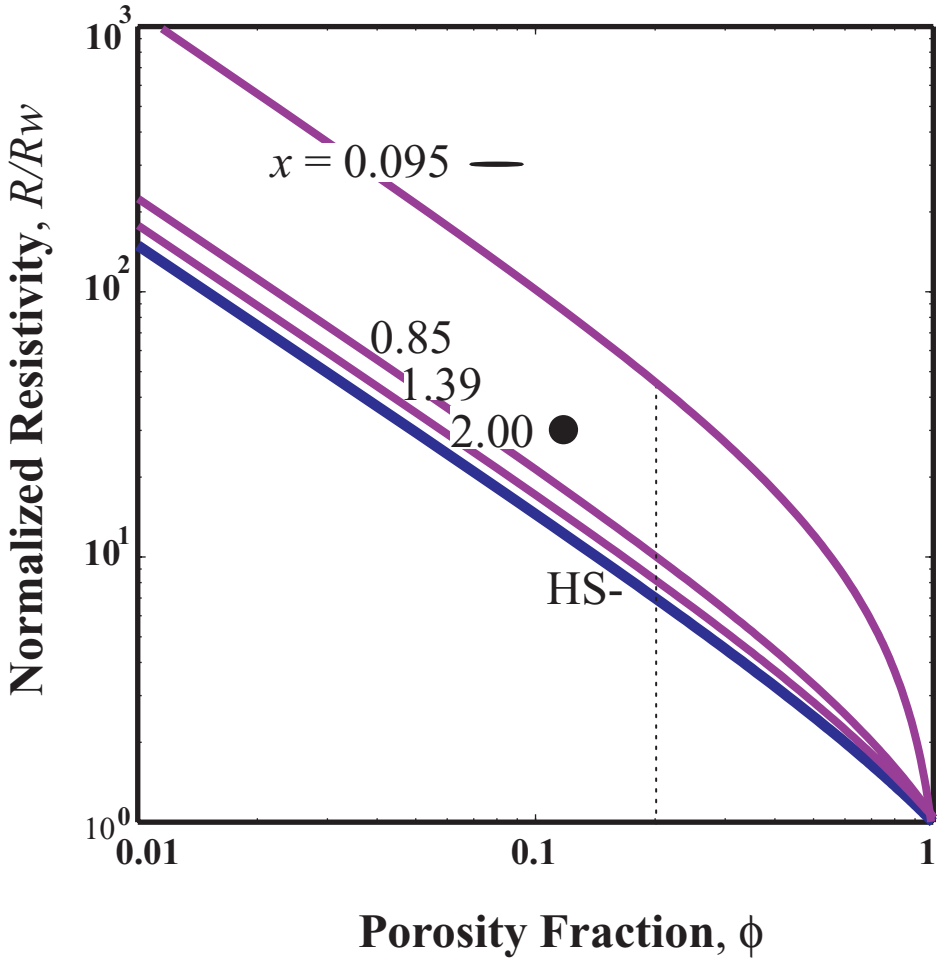

Figure 4.2: Modified Maxwell-Garnett approximation for resistive grains with different shapes. Example is for a system of minerals with $R_m = \sigma_2^{-1} = 10^{15}$ Ω-m and fluid with $R_w = \sigma_1^{-1} = 1$ Ω-m. The bold line for spheres ($x = 2$) corresponds to the lower HS bound. $x \approx 1.39$ in highly spherical sand grains, $x \approx 0.85$ in more angular sand grains, and $x_{max} \approx 0.095$ for platy grains. For $\phi < 0.2$, the ϕ - R/R_w relationship is nearly linear and m ≈ 1.5 and a_H increases with decreasing ellipticity. Schematic grain shapes are not to scale.

For a system of resistive grains suspended in a conducting fluid, like Eqn. 4.5, the effective resistivity R_F of the composite is a function of the fluid's resistivity, not of the mineral resistivity. For the specific case of a system of insulating spherical grains ($x = 2$), Eqn. 4.8 reduces to the lower HS bound (Eqn. 4.5); in other words, the minimum R_F occurs when the grains are spherical. The less spherical the grains, the further the MG curve plots above the lower HS bound. Notice, however, that for approximately $\phi < 0.20$,

m ≈ 1.5 and a_H increases as ellipticity decreases (Figure 4.2); in other words there is a nearly linear relationship between ϕ and R/R_w for $\phi < 0.20$ and a_H and m are independent.

Self-consistent Approximation

The self-consistent estimate of effective conductivity σ^*_{SC} for an isotropic system of ellipsoidal inclusions is a function of the inclusion depolarizing factors L_j, conductivity σ_i and volume fractions f_i (Berryman, 1995)

$$\sum_{i=1}^{N} f_i\left(\sigma_i - \sigma^*_{SC}\right)P^{*i} = 0 \qquad (4.7)$$

$$P^{mi} = \frac{1}{9}\sum_{j=1}^{3}\frac{1}{L_j\sigma_i + (1-L_j)\sigma_m}$$

where N is the number of constituents and L_j is defined in Chapter 3, Section 4.2.1. σ^*_{SC} is solved for through iteration and always satisfies the HS bounds.

SC theory describes a system where the pore space has defined inclusion shapes, unlike the MG theory. Because the pore space has a defined shape, there is a porosity limit below which the pore inclusions are no longer connected and the effective conductivity approaches zero; this porosity limit is known as the porosity percolation threshold ϕ_p (Section 3.2.2). The percolation threshold is a function of pore shape in Eqn. 4.7; spherical pores having the largest ϕ_p and needles having the smallest ϕ_p. In a system of spherical grains and pores of different shapes, the porosity percolation threshold ϕ_p (Figure 4.3) is 1/3 for spherical pores (α=1), 1/5 for disk-shaped pores (α = -∞), and 0 for needle-shaped pores ($\alpha = \infty$) (Norris et al, 1985).

According to SC theory, pore and grain ellipticity have opposing effects on R; R increases from increasing pore ellipticity and decreasing grain ellipticity. SC theory predicts that resistivity data converge at $\phi \approx 0.70$ (Figure 4.2), regardless of the pore shape or constituent resistivities in two-constituent systems. For $\phi > 0.70$, resistivity data falls along a single curve, which is approximately equal to the lower HS bound. For $\phi <$ 0.70, the SC resistivity estimate is greatest for spherical pores and least for disk-shaped pores (Figure 4.2). This is likely a consequence of ellipsoid surface area; spheres have a

minimum surface area per unit volume, therefore less area in contact with other pores. The percolation threshold in natural sediments and rocks is very low (Section 3.2.2), therefore the pore space likely becomes more needle-shaped as porosity decreases.

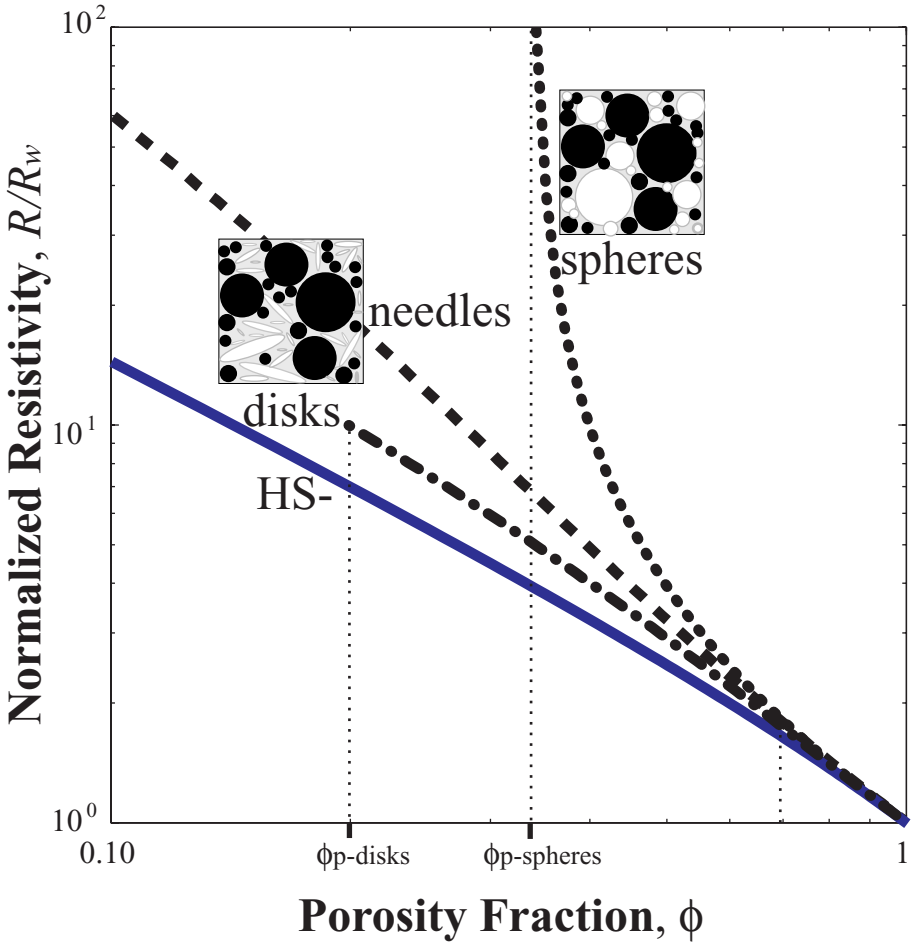

Figure 4.3: Self-consistent approximation for three pore shapes. Self-consistent approximations for spherical grains ($R_m = \sigma_2^{-1} = 10^{15}$ Ω-m) and pores that are spherical (dotted line), needle-shaped (dash-dot line), and disk-shaped (dashed line) ($R_w = \sigma_1^{-1} = 1$ Ω-m). The lower HS bound (bold solid line) is shown for reference. The porosity percolation threshold ϕ_p is 1/3 for spheres, 1/5 for disks, and 0 for needles. The SC curves converge at $\phi \approx 0.70$. The black regions in the schematic sphere pack represent the resistive grain constituent and the white represents the conductive pore constituent. Schematic grain shapes are not to scale.

4.2.2 Empirical Resistivity Background

The *R* – *F* Relationship

Archie (1942) found empirically that the true resistivity R of a fully brine-saturated system of insulating grains increased linearly with varying brine resistivity R_w.

$$R = FR_w \tag{4.8}$$

The proportionality constant that relates the material's true resistivity and brine resistivity is the formation resistivity factor F ($F \geq 1$).

The electrical current solely flows through the conducting liquid in a system of insulating grains with both resistive fluid (i.e. gas) and conducting liquid in the pore space (i.e. brine). In such a system, the ability for the current to flow is strongly influenced by the conducting liquid fraction S_w. Archie's water saturation equation (Archie, 1942)

$$R = FR_w S_w^{-n}, \tag{4.9}$$

is a general form of Eqn. 4.8 that accounts for partial saturation. The saturation exponent n is approximately two (Tiab and Donaldson, 1996). The water saturation equation is typically used to predict brine saturation in systems of insulating grains, such as clean sands.

The effects of clays on R have been studied since the 1950's, however a practical and universal method for accounting for the affect of clay conductivity and particle shape still has not been developed. Two different concepts have been developed to estimate the influences of clays on R (summarized in Worthington, 1985): one is based on the clay volume fraction and the other on ionic double-layer phenomenon. Models based on the clay volume fraction are have little physical basis, however, those based on ionic double-layer phenomenon require destructive core analysis, making them less practical. Both types of models have the general form of

$$R = FR_w + X \tag{4.10}$$

In clean sands, X approaches zero and Eqn. 4.10 reduces to Archie's equation (Eqn. 4.8). X is typically written either as a function of the cation exchange capacity or the distribution of clays, the clay conductivity and volume. The presence of clays leads to a non-linear relationship between R and R_w if R_w is high (Worthington, 1985). The clay conductivity effect is insignificant in a fully brine saturated system when the ratio of the liquid to clay resistivities R_w/R_{cl} is less than 0.10 (Hoyer and Spann, 1975). Interestingly, like the theoretical Eqns. 4.3 and 4.5, the clay-adjusted models are functions of the conductive constituents, not the resistive constituents.

An example of a practical resistivity model based on the clay volume fraction is (Schlumberger, 1989)

$$R = FR_w(1-V_{cl})S_w^{-n} + \frac{R_{cl}}{V_{cl}}S_w^{-n+1} \tag{4.11}$$

Eqn. 4.11 (same as Eqn. 2.4) is typically used to predict brine saturation in clay-rich systems, where R and R_w are measured, the clay volume fraction V_{cl} is estimated, the clay resistivity R_{cl} is assumed, and F is estimated using Eqn. 4.12. A variety of clay-adjusted equations have been developed that satisfy Eqn. 4.8 (Summarized in Worthington, 1985, Tiab and Donaldson, 1996, and Schlumberger, 1989). However, Eqn. 4.11 works well (Schlumberger, 1989) for many clay-rich formations, independent of the distribution of the clays (dispersed, laminated or structural). When the clay fraction is zero, Eqn. 4.11 reduces to Archie's water saturation equation for clean sands (Eqn. 4.8).

The $F - \phi$ Relationship

Much like hydraulic permeability, the formation resistivity factor F is the characteristic flow property of a material; it is a measure of the inability for an electrical current to flow through pore space. Archie derived the empirical relationship $F = \phi^{-m}$, which Winsauer et al (1952) later generalized as

$$F = \frac{a_H}{\phi^m} \tag{4.12}$$

The Humble equation (Eqn. 4.12) is only valid for the formation's porosity range. Since the Humble equation is empirical, it is not required to meet the limiting conditions

$R = R_m$ at $\phi = 0$ nor $R = R_w$ at $\phi = 1$. There isn't a percolation threshold term in the Humble equation, therefore the pore space is assumed connected for all porosities (Webman et al, 1976, 1977; Straley, 1978). Sen et al (1979) suggested modifying the Humble equation to account for the percolation threshold by

$$F = \frac{a_H}{(\phi - \phi_p)^m} \tag{4.13}$$

The modification of the porosity term by subtracting the percolation threshold is similar to the modification in the Kozeny-Carman equation for permeability by Mavko and Nur (1997). The percolation threshold term in Eqn. 4.13 significantly influences high F values, corresponding low ϕ values; therefore a_H and m values derived from Eqn. 4.13 would be significantly influenced by the percolation term in low porosity data.

Eqn. 4.12 was derived based upon the observation of ϕ - F data for a particular formation plotting linearly on a log-log plot. For example, taking the log of both sides of Eqn. 4.12 leads to

$$\ln(F) = \ln(a_H) - m\ln(\phi) \tag{4.14}$$

The internal geometry parameter a_H and cementation exponent m are computed as the y-intercept and negative slope, respectively, of the least-squares fit to ϕ- F data on a log-log plot (Figure 4.4.a). a_H and m define the formation's characteristic properties therefore are computed for individual formations. a_H and m cannot be defined uniquely for a formation if either there are too few porosity data available or the porosity range is too narrow (Figure 4.4.b), a common problem encountered with environmental data sets (discussed in Chapter 2). In such cases, a_H and m can be extrapolated from similar hydrogeologic formations. The uncertainty in the parameters a_H and m, which define the linear relationship, can significantly influence porosity estimates that are outside the range of the porosity data.

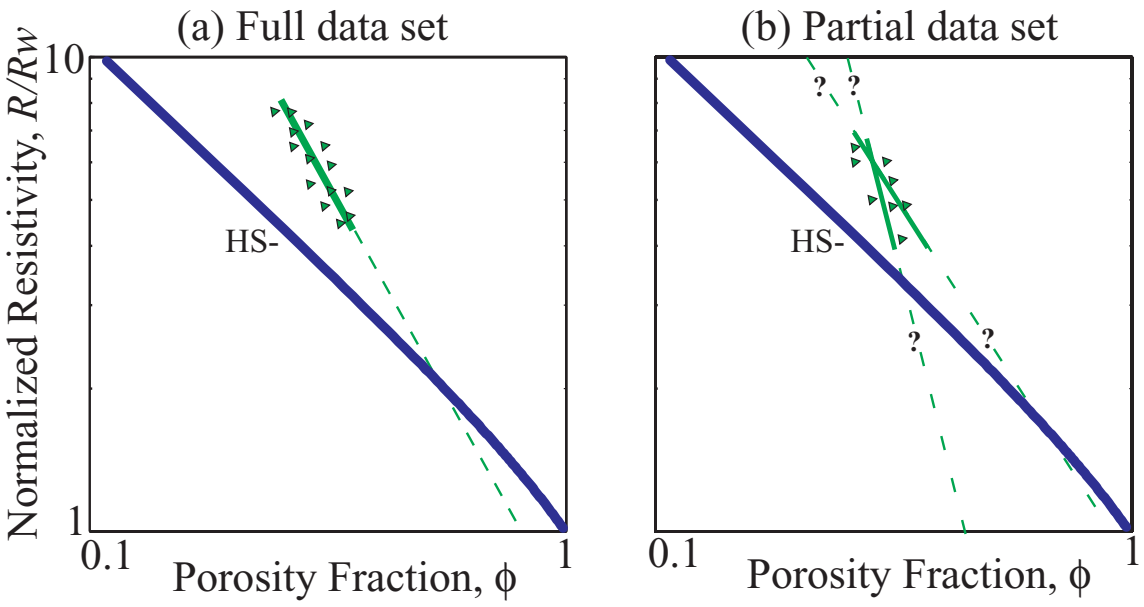

Figure 4.4: Linear relationship between F and ϕ on log-log plot. Example of: (a) full data set where there is a linear relationship and (b) partial data set where there is greater uncertainty in a_H and m.

Both a_H and m are to some degree influenced by pore space and bulk characteristics such as shape, sorting, packing, pore configuration and size, tortuosity, type of pore system (intergranular, intercrystalline, vuggy, fractured), compaction and clay content (Tiab and Donladson, 1996). Gomez-Rivero (1976) derived relationships between a_H and m of the form

$$\ln(a_H) = C_1 + C_2 m \tag{4.15}$$

where C_1 and C_2 values for various materials are listed in Table 4.2. The relationship between m and $\ln(a_H)$ originates from the way a_H and m are derived in Eqn. 4.14. Archie (1942), on the other hand, showed that a $\approx$ 1 and m increases with increased cement in clean sands (Figure 4.5.a), and MG theory suggests that for $\phi < 0.20$, m $\approx$ 1.5 and a_H increases as ellipticity decreases (Figure 4.5.b); both suggest that a_H and m are independent since one is assumed constant. These observations suggest that if either a_H or m can be constrained then the other can be determined; this is especially significant when the porosity data range is too narrow to define a_H and m uniquely.

ID	Formation Description	y-intercept C_1	slope C_2
1	Sandstones	1.04	-0.60
2	Sands	1.40	-0.78
3	Carbonate rocks	2.26	-1.11

Table 4.2: Slopes and intercepts that define the $\ln(a_H) - m$ relationship for various materials (Gomez-Rivero, 1976).

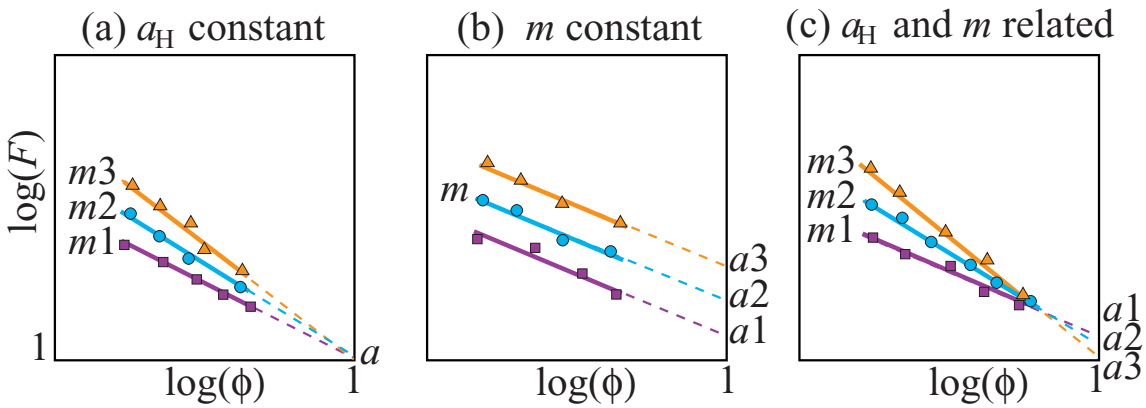

Figure 4.5: Schematic of a_H and m. (a) a_H constant, (b) m constant, and (c) $a_H - m$ related.

The cementation exponent m value is dominated by the presence of cement. m is much larger in cemented materials than in uncemented ones (Wyllie and Gregory, 1953), however, it has not been correlated with the amount of cement. Various authors (Neustaedter, 1968; Gomez-Rivero, 1976; Sethi, 1979) have shown correlations between m and ϕ in rocks. Perez-Rosales (1982) suggested that m is the conversion exponent between channel porosity and total porosity $\phi_{ch} = \phi^m$; the greater the m, the lesser the channel porosity ϕ_{ch} and the greater the trapped porosity ϕ_{tr} (Section 3.2.1). The observed range of m is 1.2 - 4 (Mendelson and Cohen, 1982)

The internal geometry parameter a_H value appears to be dominated by the influence of tortuosity (Wyllie and Gardner, 1958; Herrick, 1988). In most natural composites, a_H doesn't vary much (Schlumberger, 1989). However, as seen in Figure 4.2, a_H is expected to increase significantly as grain ellipticity decreases. The theoretical range of a_H defined by grain ellipticity is 0.25 – 10 (Mendelson and Cohen, 1982).

4.3 New Results on the Resistivity – Porosity Relationship

4.3.1 New Insight into the Influence of Clay on R, F, a_H and m

It is standard practice to use resistivity data to solve for F using Eqn. 4.8 so that $F - \phi$ relationships can be determined for each formation using Eqn. 4.12. However, Eqn. 4.8 is only valid for systems of fully saturated insulating grains; it is not valid for systems of neither partial saturation nor conducting minerals ($F \neq R/R_w$). Therefore, F values published as R/R_w *do not* describe the material's flow characteristics unless in a clay-free and fully saturated systems. Solving for F correctly is particularly important when using F to solve for permeability (Chapter 2). For this reason, R/R_w is referred to as the *normalized resistivity* throughout the rest of this chapter, rather than formation factor.

To better understand the difference between the normalized resistivity R/R_w and formation factor F, consider the following: electrical conductivity is analogous to hydraulic conductivity and formation resistivity factor is analogous to permeability. R/R_w is a function of F and they are only equivalent when $S_w = 1$ and $\sigma_m \approx 0$ (Eqn. 4.11). We suggest that it is more appropriate to solve for F using a clay-adjusted equation like Eqn. 4.11, rather than Eqn. 4.8, in systems of insulating grains with partial saturation and/or conducting minerals (Chapter 2). Solving for F in such a way would "remove" the influence of the conducting minerals so that F would be a function of the pore space, not of the conducting mineral component.

It is important to understand the influence of clays on R and F when interpreting pore space characteristics using ϕ - R/R_w data (Section 4.3.2) and when comparing a_H and m values (Section 3.3.3). Dispersed or structural clay can be added to a system by either replacing pore or granular volumes. The clay influences on F and R depend on the clay distribution and conductivity. Replacing pore space with clay increases F, however, effect of replacing granular volume with clay depends on the clay distribution and compaction; replacing granular volume with structural clay likely has a minimal influence on F and replacing the same granular volume with dispersed clay likely

increases F and the degree of influence depends on the clay compaction. There are two competing effects of clays on R; (1) the conductivity effect: the high conductivity of clays decreases the bulk mineral resistivity, which contributes to a decrease in R, and (2) the tortuosity effect of dispersed clays: the presence of dispersed clays increases F, which contributes to an increase in R.

The influences of clay on F are shown in Figure 4.6.a. Replacing pore space with platy dispersed clays significantly increases F by increasing tortuosity and trapped porosity. This effect is theoretically described by Eqn. 4.4 (Figure 4.2) and empirically accounted for in the internal geometry parameter a_H, a measure of tortuosity (Eqn. 4.12). However, if the same amount of pore space is replaced with structural clays (i.e. shale fragments), then the influence of clay on F is minimal since the tortuosity wouldn't change significantly; it is essentially a sorting effect (Section 3.3.2). Therefore, the slope $-m$ on a log-log ϕ - F plot should be greater for systems of dispersed clays than for systems of structural clays (Figure 4.6.a).

The influences of replacing sand pore space with clay on resistivity are summarized in Table 4.3 and schematically shown in Figure 4.6.b. The influences of clay on R depend on the clay's conductivity, volume and distribution within the sand's pore space (Eqn. 4.11). The clay conductivity effect is insignificant in a fully brine saturated system when the ratio of the liquid to clay resistivities R_w/R_{cl} is less than 0.10 (Hoyer and Spann, 1975). In such systems, the influence of clay is solely through tortuosity, therefore the influence on R/R_w is the same as on F (Figures 4.6.a and 4.6.b). In a saturated freshwater system, the clay tortuosity effect likely dominates when dispersed clay fills the pore space, resulting in a high R, whereas the clay conductivity effect likely dominates when structural clays fill the same amount of pore space, resulting in low R (Figure 4.6.b).

Erickson and Jarrard (1998) used ϕ - R/R_w data in high porosity, clay rich materials to show that muds have higher m and lower a_H values than clay-rich sands. The data they used also shows a transition in the ϕ - R/R_w relationship between clay-rich sands and sandy muds at $\phi \approx 0.55$, which is approximately the critical porosity of sand; in other words, like work by Marion (1990), the critical porosity defines the transition between

clay-dominated and sand-dominated systems. In the sand-dominated system, dispersed clays replace pore space and in the clay-dominated system, dispersed clays essentially replace sand grains. Several other authors (Carothers, 1968; Porter and Carothers, 1971) have observed that ϕ - R/R_w data in clay-rich sands typically have low m and unusually high a_H values, whereas ϕ - R/R_w data in muds and shales have high m and low a_H values (Schlumberger, 1989). The unusually high a_H values in clay-rich sands are likely either a consequence of the non-linear dependence of R on clay volume (Eqn. 4.11) or a grain shape effect; according to MG theory, R is higher for platy grains than spherical ones.

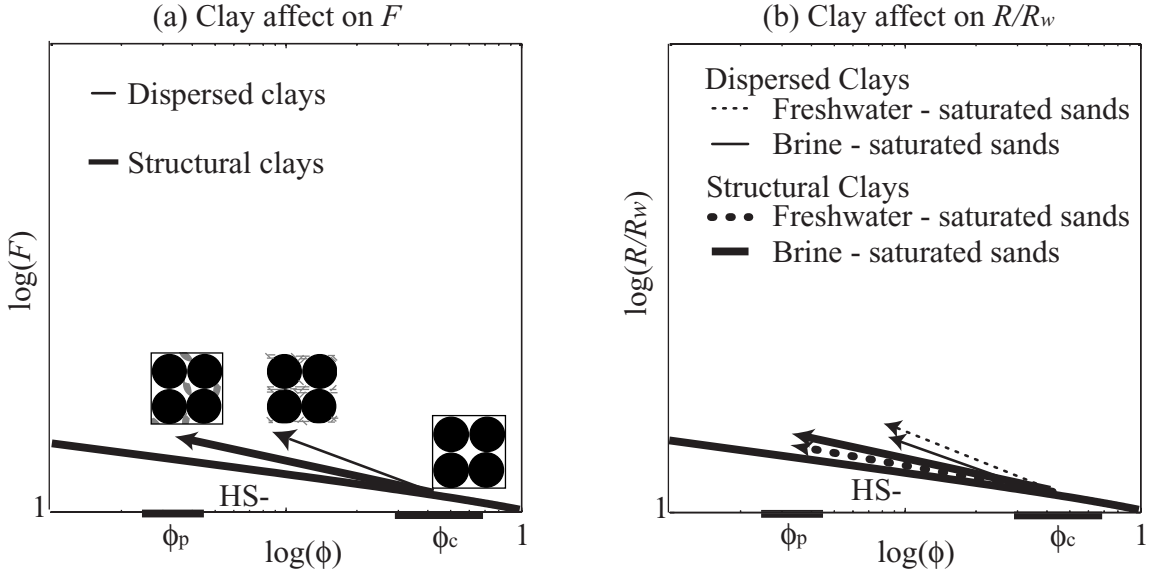

Figure 4.6: The influence of clays on F and R. The influence of adding clay to a sand system: (a) the influence on F of adding dispersed and structural clays to a saturated sand and (b) the influence on R/R_w of adding dispersed and structural clays to brine and freshwater saturated sands.

Adding clay to sand pore space	Conductivity effect	Tortuosity effect
dispersed clays to brine saturated sands	insignificant	increases
dispersed clays to freshwater sands	decreases	increases
structural clays to brine saturated sands	insignificant	slightly increases
structural clays to freshwater sands	decreases	slightly increases

Table 4.3: The proposed influence of dispersed and structural clays in freshwater and brine-saturated sands on resistivity.

4.3.2 Evaluating Pore Space Characteristics using ϕ - R/R_w Data

Changes within a formation can occur from the addition or subtraction of material from the pore or granular volumes. When the granular volume changes, the resistivity might change without a change in porosity, such as replacing resistive sand grains with shale fragments or spherical grains with elliptical ones. However, when the pore volume changes there is a change in both resistivity and porosity. Changes in a composite's pore space characteristics can occur from changes in cementation, compaction, sorting, grain ellipticity and clay volume. Trends of data on an ϕ - R/R_w plot can help identify the varying pore space characteristics within a particular formation and delineate individual formations with different characteristic properties.

R/R_w increases from increased tortuosity and trapped porosity; this occurs from changes in the pore space characteristics such as increased clay volume, cementation (Archie, 1942) and compaction (Tiab and Donaldson, 1996) and decreased sorting (large grain size distribution) (Wyllie and Gregory, 1953) and granular ellipticity (Fricke, 1924) in a system. These same changes in pore space characteristics result in a reduction of the system's total porosity ϕ (Wyllie and Gregory, 1953; Maxwell, 1960; Beard and Weyl, 1973).

The location of data on a ϕ - R/R_w plot can be thought of as a particular stage of evolution in the complexity of a simple system's pore space. For example, let's say the original system is of well-sorted, single constituent, loosely-packed grains and for simplicity of explanation, assume the grains are resistive and spherical (Figures 4.7 a, b and c). In such a system, ϕ - R/R_w data plot at the system's origin, which is defined by the point on the lower HS bound evaluated at the system's critical porosity ϕ_c (Figures 4.7

a, b and c); the lower HS bound coincides with the MG curve for suspended spherical grains (Section 4.2.1). As the system's ϕ decreases from a particular pore space property, R/R_w increases linearly on a log-log plot, resulting in a fan of lines emanating from the system's origin. The slope -m and y-intercept ln(a_H) of the line depends on the pore space property that is changing. For example, increasing the degree of cementation has a more significant affect on R/R_w than ϕ, therefore m is high and a_H is low (Figure 4.7.b). Decreasing the sorting of the sphere pack has a lesser effect than cementation on R/R_w at the same porosity, therefore m is lower and a_H is higher (Figure 4.7.a). As the loose spheres become compacted (Figure 4.7.c), they are arranged into tighter packing, increasing R/R_w and decreasing ϕ.

If instead of spherical grains, the original system is of aspherical, well-sorted, single constituent, loosely-packed, resistive grains, then the system's origin is defined by the point on the MG curve (Eqn. 4.4; dashed line in Figures 4.7 d, e and f) evaluated at the system's critical porosity ϕ_c. For grains of low sphericity, the MG curve plots above the lower HS bound (Figure 4.2) and the system's critical porosity is greater than that of spheres (Section 3.2.1). As explained by MG theory, increased grain ellipticity in grain-supported systems insignificantly influences m, however increases a_H, so the slopes are approximately the same as in Figures 4.7 a, b and c.

In most natural systems, a combination of pore space properties can influence the system's ϕ_c, which could result in linear trends that don't precisely intersect the original system's origin. However as seen in Figure 4.8, for the most part, the hypothesis of lines converging near the lower HS bound at the critical porosities of granular systems is a good approximation in a wide variety of systems. This hypothesis suggests that as m increases, ln(a_H) decreases linearly, and the linear relationship between m and ln(a_H) is defined by the system's origin. The relationship between a_H and m is discussed in Section 4.3.3 below.

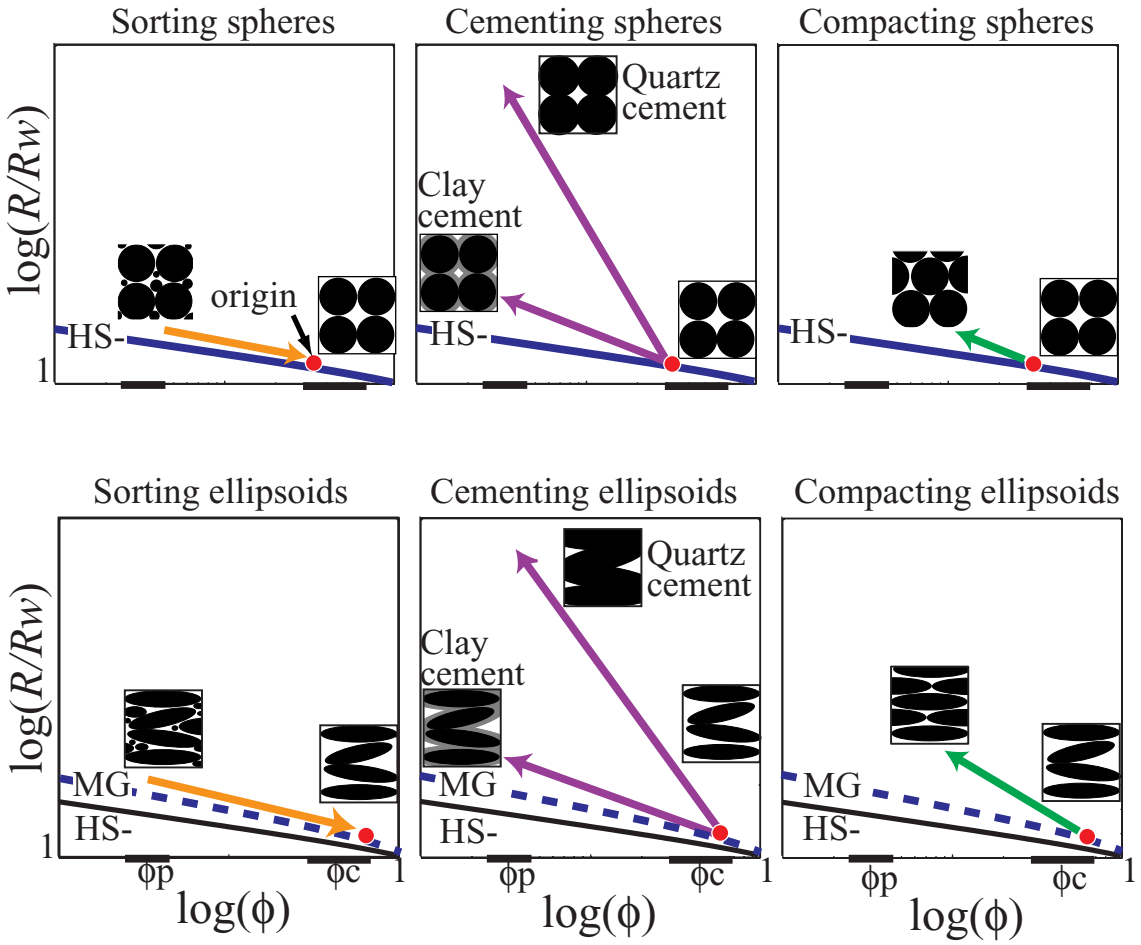

Figure 4.7: Schematic of the influence of ellipticity, sorting, cement and compaction on F and ϕ. The influence of (a,d) sorting, (b,e) cement and (c,f) compaction on F and ϕ in systems of spherical and aspherical grains. The arrows indicate direction of increased change in property. The bold solid line is the lower HS bound (Eqn. 4.2.1) and the bold dashed line in is the MG curve for elliptical grains (Eqn. 4.5).

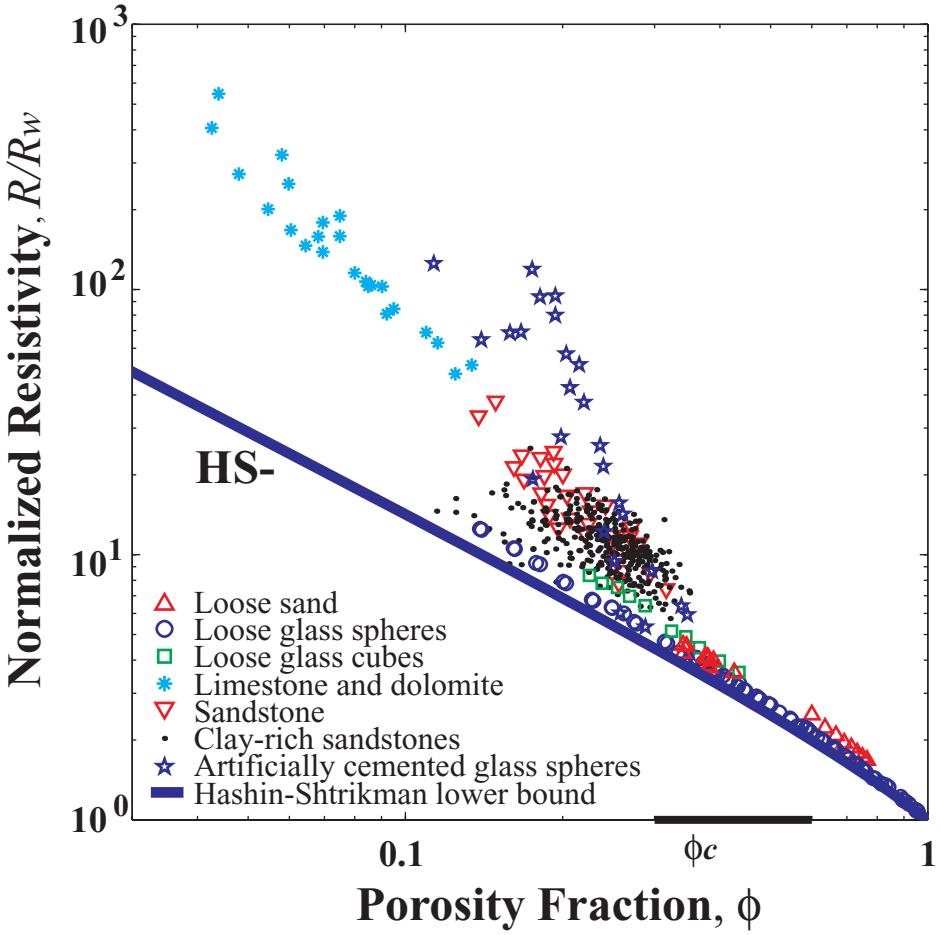

Figure 4.8: R/R_w - ϕ lab and field data. Shown are: loose clean sands (Wyllie and Gregory, 1953; Fricke, 1924), loose glass spheres (Wyllie and Gregory, 1953; Klinkenberg, 1951; Slawinski, 1926; Balderas-Joers, 1975), loose glass cubes (Wyllie and Gregory, 1953), limestones and dolomites (Mendoza-Romero and Perez-Rosales, 1985), sandstone (Winsauer et al, 1952; Wyllie and Spangler, 1952; Sanyal et al, 1973; Wyllie and Rose, 1950), clay-rich sandstone (Porter and Carothers, 1971), and artificially cemented glass spheres (Wyllie and Gregory, 1953); the lower HS bound (solid line) is plotted for reference. Data converges near the HS lower bound at approximately $0.30 \leq \phi \leq 0.4$.

4.3.3 New a_H - m Relationship

Both a_H and m are, to some degree, influenced by the same pore space and bulk characteristics and are likely related. And, as seen in Figure 4.8, ϕ - R/R_w data converge towards the lower HS bound evaluated at porosities near the critical porosities of granular

systems. This suggests that as m increases, $\ln(a_H)$ decreases linearly, and the linear relationship between m and $\ln(a_H)$ is defined by critical porosity and grain shape. The point defined by the MG curve for the primary constituent's shape evaluated at the composite's critical porosity (ϕ_c, R^*_{MG}/R_w) may be a pivot point for linear $R/R_w - \phi$ relationships (Figures 4.7 and 4.6.c). By solving for $\ln(a)$ in Eqn. 4.14 and substituting Eqn. 4.5 in for F evaluated at ϕ_c gives

$$\ln(a_H) = C_1 + C_2 m \tag{4.16}$$

where

$$C_1 = \ln\left(\frac{(x+1)-\phi_c}{x\phi_c}\right) = \ln\left(\frac{a_F}{\phi_c} + 1 - a_F\right) \tag{4.17}$$

$$C_2 = \ln(\phi_c - \phi_p) \tag{4.18}$$

Eqn. 4.16 is of the same form as the empirical relationship derived by Gomez-Rivero (1976), where the y-intercept C_1 and slope C_2 are the formation-specific constants in Eqn. 4.15 and Table 4.2. The ϕ_c and x values in Table 4.4 were found by solving for ϕ_c in Eqn. 4.18 and x in Eqn. 4.17 in terms of the empirically derived C_1 and C_2 values in Table 4.2. These ϕ_c and x values represent the overall values for each formation represented by an $a_H - m$ data pair. As discussed in Section 3.3.2 and defined by Eqn. 4.5, for each formation, the MG curve corresponding to x evaluated at ϕ_c defines the origin from which linear ϕ - F relationships emanate (Figure 4.9).

ID	Formation	calculated ϕ_c	published ϕ_c	calculated x	published x
1	Sandstones	0.33	0.40 (1)	0.83	--
2	Sands	0.46	--	0.63	0.85 (2)
3	Carbonate rocks	0.55	0.60 (1)	0.31	--

Table 4.4: Calculated ϕ_c and x values from C_1 and C_2 values by Gomez-Rivero (1976) in found in Table 4.1; published ϕ_c and x values (1) Mavko et al (1998) & (2) Fricke (1924).

The ϕ_c and x values found using Eqns. 4.17 and 4.18 agree very well with published values (Table 4.2) even though Gomez-Rivero's empirical relationships were derived from $F = R/R_w$ data in partially brine-saturated, clay-rich materials (Section 4.3.1). Eqns.

4.16 – 4.18 are particularly useful when the porosity data range is too narrow to define a_H and m uniquely and either a_H and m can be estimated (Section 4.2.2).

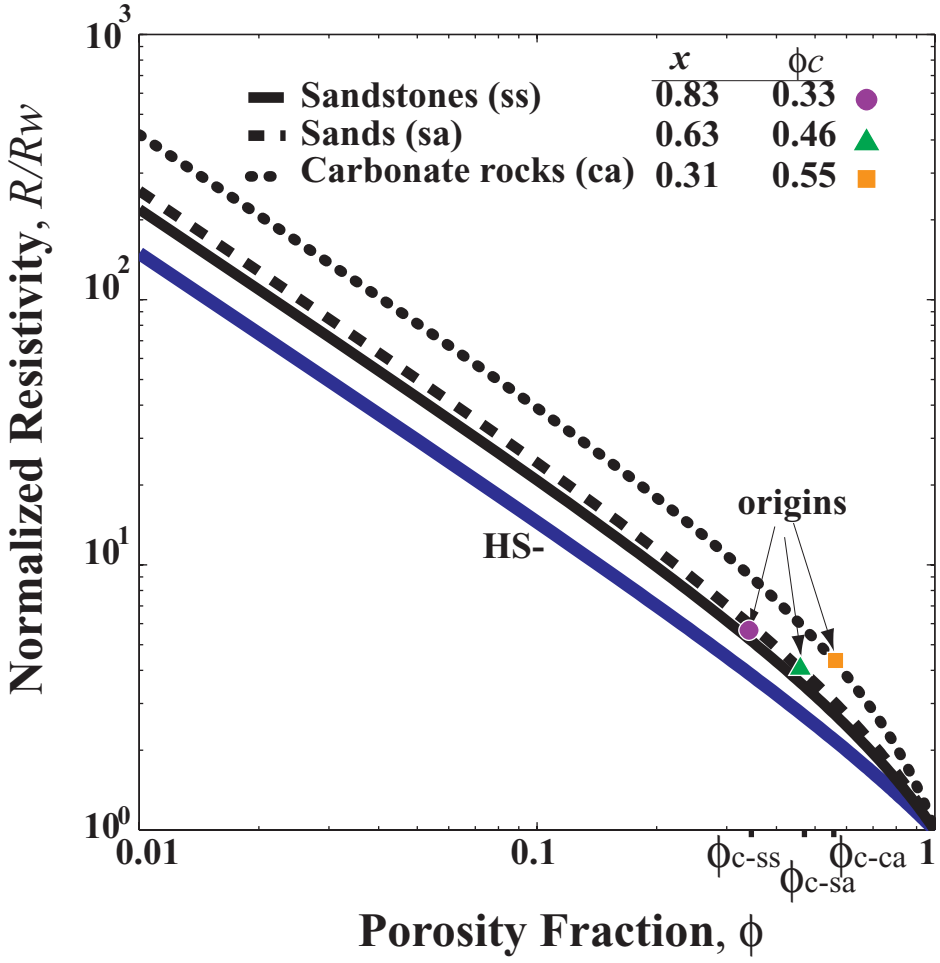

Figure 4.9: The pivot points of linear $R/R_w - \phi$ relationships. The x and ϕ_c values determined from $a_H - m$ relationships for different formations define the pivot points (origins) for linear $R/R_w - \phi$ relationships.

4.3.4 Defining a Generalized Archie's Equation

As discussed in Chapter 3, Section 3.3.2, a formation's total and channel porosities are related by a normalizing factor A (Eqn. 3.11), which is a function of the critical porosity, percolation threshold, and Archie's exponent m. The A factor is essentially

adsorbed into the formation-specific, empirical constant a_H in the Humble equation (Eqn. 4.12). a_H can be expressed in terms of A by solving for a_H in Eqns. 4.16 – 4.18 and assuming a porosity term of the form $(\phi - \phi_p)^m$ in Eqn. 4.13.

$$a_H = \frac{a_F}{A} + \frac{(1 - a_F)}{A}\phi_c \quad = \frac{x + 1 - \phi_c}{Ax} \tag{4.19}$$

Eqn. 4.19 is useful for estimating a_H when too few porosity measurements are available to define a linear relationship between ϕ and R/R_w. From Eqns. 4.13 and 4.19, a general Archie's equation can be expressed in terms of a system's channel porosity, grain shape parameter, and critical porosity by

$$F = \frac{x + 1 - \phi_c}{x\phi_{ch}} \tag{4.20}$$

Eqn. 20 is particularly useful for determining F when channel porosity is measured.

4.3.5 The ϕ - R/R_w Relationship Re-defined in Three Porosity Regions

At very low porosities, there exists a porosity limit, known as the percolation threshold ϕ_p (Section 3.2.2), below which the pore space is no longer connected and the electrical resistivity approaches the mineral resistivity. Also, at porosities between 0.30 and 0.40, the range in critical porosities ϕ_c of sands and sphere packs (Wyllie and Gregory, 1953; Mavko et al, 1998), resistivity values in cemented and uncemented sands and glass spheres converge near the lower HS bound (Figure 4.8). The critical porosity and percolation threshold define three porosity regions (discussed in Section 3.3.1) in which the $F - \phi$ relationship is defined (Table 4.3 and Figure 4.10). Region I is defined for $\phi < \phi_p$ where the pore space is no longer connected ($\phi_{ch} = 0$) and the resistivity theoretically approaches the bulk mineral resistivity value; this region may be approximated by the upper HS bound (Eqn. 4.2), however we have not come across published data in this low porosity region. Region II is defined for $\phi_p \leq \phi \leq \phi_c$ where resistivity and porosity are linearly related on a log-log plot and where the pore space is connected but not all is available for flow (trapped porosity ϕ_{tr} exists). This region, where most data in sediments and rocks fall (Figure 4.8), can be modeled well by the Humble

equation (Eqn. 4.12) and is bounded by the lower HS bound and an empirical upper bound F_+ (Section 3.3.5 below). Region III is defined for $\phi > \phi_c$ where the mineral constituents are suspended and all of the pore space is available for flow ($\phi_{tr} = 0$); resistivity in this region is approximated by the lower HS bound (Figures 4.1, 4.3 and 4.8).

For $\phi_p < \phi < \phi_c$, we suggest that ϕ - R/R_w data converge at ϕ_c because ϕ_{tr} decreases and ϕ_{ch} increases as ϕ increases within this porosity region, making it easier for electrical currents to flow through the pore space. At $\phi > \phi_c$, we suggest that ϕ - R/R_w data fall along a single curve because all of the pore space is available for flow ($m = 1$, so $\phi_{ch} = \phi$) and the tortuosity is low ($a_H \approx 1$) in this porosity region.

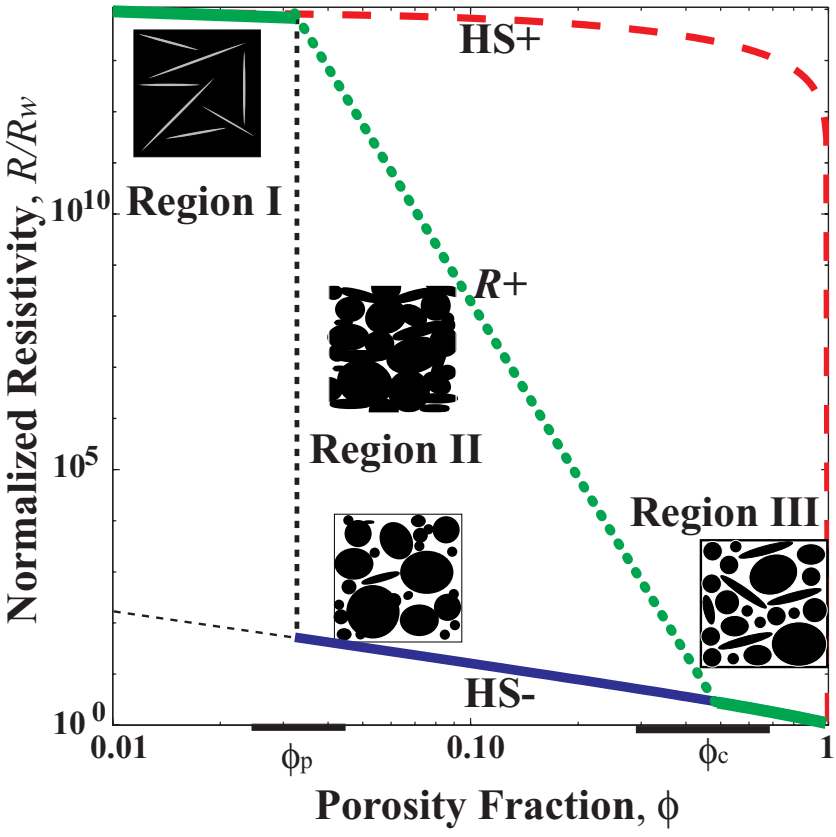

Figure 4.10: Three regions of the ϕ - R/R_w relationship defined by the percolation threshold ϕ_p and critical porosity ϕ_c. The ϕ - R/R_w relationship is defined by (1) the upper HS bound for $\phi < \phi_p$, (2) the Humble equation for $\phi_p \leq \phi \leq \phi_c$, and (3) the lower HS bound for $\phi > \phi_c$.

Region	Porosity Range	Total Porosity	Channel Porosity	Normalized Resistivity
I	$0 < \phi < \phi_p$	$\phi = \phi_{tr}$	$\phi_{ch} = 0$	R_{HS+}/R_w (Eqn. 2)
II	$\phi_p \le \phi \le \phi_c$	$\phi = \phi_{ch} + \phi_{tr}$	$\phi_{ch} = A(\phi - \phi_p)^m$	$a_H / (\phi - \phi_p)^m$ (Eqn. 4.13)
III	$\phi_c < \phi \le 1$	$\phi = \phi_{ch}$	$\phi_{ch} = \phi$	R_{HS-}/R_w (Eqn. 1)

Table 4.3: Regions of the ϕ - R/R_w relationship defined by the percolation threshold ϕ_p and critical porosity ϕ_c.

4.3.6 New Upper ϕ - R/R_w Bound

The upper HS bound immediately approaches the bulk mineral constituent resistivity at the onset of adding resistive minerals to a fluid (Figure 4.10). This behavior is not observed in granular media; in fact, data in granular media do not plot near the upper HS bound regardless of the pore space characteristics. Perhaps, this is because the upper HS bound represents isolated conductive spheres covered by a resistive shell (Figure 4.1), a valid scenario in few rocks (i.e. basalts where the pore space is defined by trapped air bubbles). It is an unlikely scenario in sediments where the resistive grains make up the ellipsoidal component of the system. The upper HS bound therefore is of limited use in sediments and most rocks.

We define an empirical upper bound R_+ that is lower than the upper HS bound and is defined by a line that connects the points (ϕ_p, R^*_{HS+}/R_w) and (ϕ_c, R^*_{HS-}/R_w) on a log-log plot. The first point corresponds to the upper HS bound evaluated at the percolation threshold ϕ_p; the second point corresponds to the lower HS bound evaluated at the critical porosity ϕ_c. This idea stems from work done by Nur et al (1995) on modifying the upper bound for the acoustic velocity – porosity relationship. This linear upper bound corresponds to the Humble equation (Eqn. 4.12), where

$$\frac{R_+}{R_w} = \frac{a_+}{(\phi - \phi_p)^{m_+}} \tag{4.21}$$

where $\phi_p \le \phi \le \phi_c$ and

$$m_+ = \frac{\ln\left(R^*_{HS+}/R^*_{HS-}\right)}{\ln\left(\phi_c/\phi_p\right)} \tag{4.22}$$

$$a_+ = \exp\left[\ln\left(R^*_{HS-}/R_w\right) + m_+ \ln\left(\phi_c - \phi_p\right)\right] \tag{4.23}$$

The empirical upper bound and lower HS bound are narrow for porosities near ϕ_c and wide for porosities near ϕ_p (Figure 4.10). ϕ - R/R_w data in unconsolidated glass sphere packs fall just above the lower HS bound for $\phi < \phi_c$ and on the lower HS bound for $\phi > \phi_c$ (Figures 4.8 and 4.11). Data in artificially cemented glass spheres plot just below the empirical upper ϕ - R/R_w bound (Figure 4.11).

The maximum a_+ is 1.5, the a_H of the lower bound for $\phi < \phi_c$, since one end member is defined by the lower HS bound. Small variations in ϕ_p and ϕ_c significantly influence the log intercept a_+ and slightly influence the slope -m of the empirical upper bound. For example, for $R_m = 10^{14}$ Ω-m and $R_w = 1$ Ω-m, $\phi_p = 0.035 \pm 0.01$ (28% uncertainty) and $\phi_c = 0.40 \pm 0.05$ (28% uncertainty) leads to $a_+ = 2.75 \cdot 10^{-5} \pm 2.31 \cdot 10^{-4}$ (843% uncertainty) and $m_+ = 12.75 \pm 0.73$ (5.7% uncertainty). The uncertainty of a_+ is statistically very significant because of the log dependence of a_H, however, as seen in Figure 4.10, it has nominal influence on the upper bound on a log-log plot.

A modified upper HS bound R_{MHS+} (Figure 4.11) can be defined by evaluating the upper HS bound for $\phi^* = \phi/\phi_c$, where $0 \le \phi^* \le 1$ and $0 \le \phi \le \phi_c$ and the end members are defined by $(0, R_m/R_w)$ and $(\phi_c, R^*_{HS-}/R_w)$. However, like the upper HS bound, the modified upper HS bound immediately approaches the mineral resistivity at the onset of adding the resistive mineral constituent to the fluid constituent. As shown in Figure 4.11, data do not plot near the modified upper HS bound, regardless of the pore space characteristics.

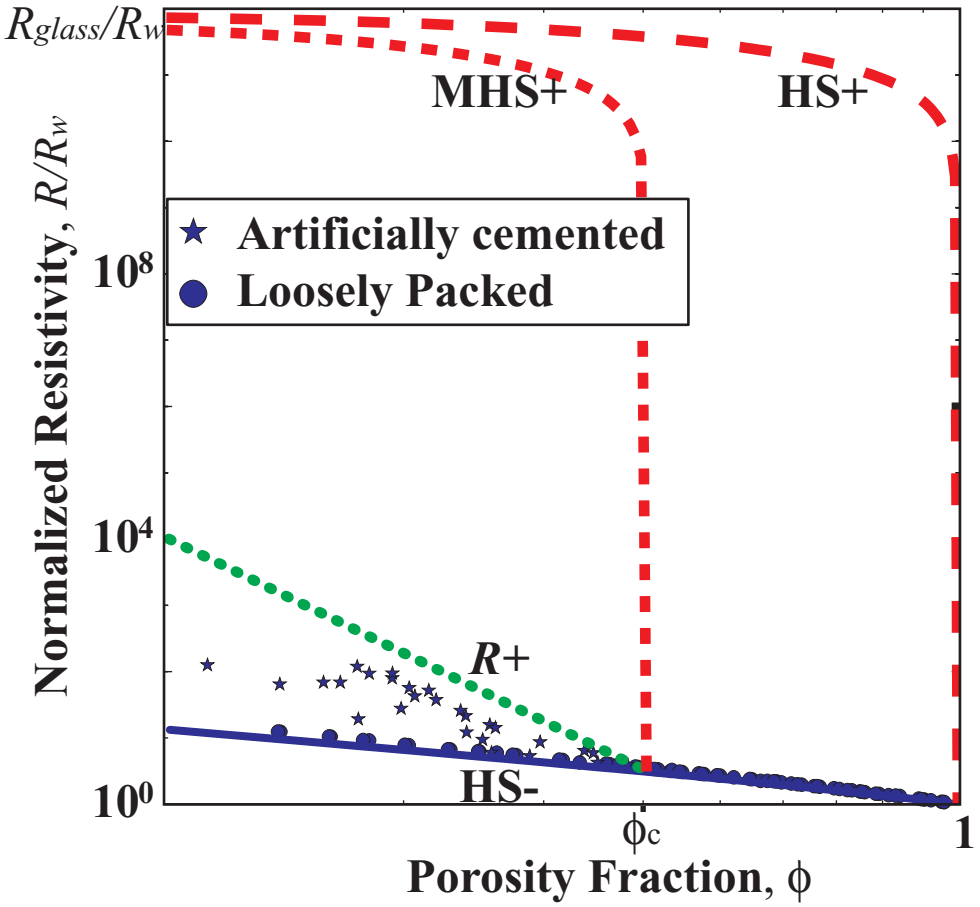

Figure 4.11: The empirical upper ϕ - R/R_w bound. R/R_w – ϕ lab data for loose glass spheres (circles) and artificially cemented glass spheres (stars) from Wyllie and Gregory (1953); the HS bounds (solid and dashed lines), the modified upper HS bound (short dashed line), and the empirical upper bound (dotted line), where $\phi_c = 0.40$, $\phi_p = 0.035$, $R_m = 10^{14}$ Ω - m and $R_w = 1$ Ω - m. Data is also plotted in Figure 4.8.

4.4 Conclusions

- F values published as $F = R/R_w$ do not describe the material's flow characteristics unless in a clay-free and fully saturated systems.

- Increasing clay content increases F, however there are two competing effects on R: (1) the conductivity effect: the high conductivity of clays decreases the bulk

mineral resistivity (Eqn. 4.8), which contributes to a decrease in R, and (2) the tortuosity effect: the presence of dispersed clays increases F, which contributes to an increase in R.

- The lower Hashin-Shtrikman bound is independent of the mineral resistivities and volume fractions if R_m/R_w is greater than approximately 10^3.

- In systems of resistive and conductive constituents, it is the conductive constituent's resistivity and volume, not the resistive constituent's resistivity and volume, that define the behavior of the lower HS bound, the MG equation, and the empirical relationships.

- In a given formation, the formation resistivity factor may increase and porosity may decrease from an increase in clay content, compaction, or cementation or a decrease in grain ellipticity or sorting; the data trends (a_H and m) on a $F - \phi$ plot can help diagnose the property causing the change.

- According to MG theory, grain ellipticity influences a_H significantly and m insignificantly in grain-supported unconsolidated composites ($\phi < 0.20$).

- Adding clay to the pore space of a sand system will result in an increased formation factor and decreased porosity, regardless of the clay structure; however, depending on the clay structure and the ratio R_{cl}/R_w, it will result in either an increase or decrease in the measured resistivity.

- $F - \phi$ data in unconsolidated glass sphere packs fall just above the lower HS bound for $\phi < \phi_c$ and on the lower HS bound for $\phi > \phi_c$.

- The HS bounds and MG theory are approximately linear for $\phi < 0.20$.

- SC theory predicts that resistivity converges at $\phi \approx 0.70$, regardless of the pore shape and constituent resistivity in a two-component system.

- The ϕ R/R_w data in sands and sphere packs tend to converge near the lower HS bound at porosities between approximately 0.30 and 0.40, which correspond to the critical porosities of sands and spheres.

- The ϕ - R/R_w relationship can be defined by three regions: (1) for $\phi \leq \phi_p$, $R/R_w \approx R_{HS+}/R_w$, (2) for $\phi_p < \phi < \phi_c$, $R/R_w = a/\phi^m$, and (3) for $\phi \geq \phi_c$, $R/R_w \approx R_{HS-}/R_w$.

- For $\phi_p < \phi < \phi_c$, ϕ - R/R_w data converge at the critical porosity because ϕ_{tr} decreases and ϕ_{ch} increases as ϕ increases within this porosity region.

- At $\phi > \phi_c$, ϕ - R/R_w data fall along a single curve because all of the pore space is available for flow (m = 1, so $\phi_{ch} = \phi$) and the tortuosity is low ($a_H \approx 1$) in this porosity region.

- An empirical upper bound on the R/R_w relationship can be defined by the line $F_+ = a_+ / \phi^{m_+}$, where a_+ and m_+ are the y-intercept and negative slope of a line that connects the points (ϕ_p, R^*_{HS+}/R_w) and (ϕ_c, R^*_{HS-}/R_w) on a log-log plot.

- The a_H – m relationship can be expressed as a function of the primary constituent's critical porosity and grain shape.

4.5 References

Archie, G.E., 1942. The electrical resistivity log as an aid in determining some reservoir characteristics. *Trans. Am. Inst. Mech. Eng.,* 146, 54-62.

Balderas-Joers, C., 1975. Estudio experimental del factor de resistivitidad y la porosidad en medios no consolidados de muy alta porosidad. Tesis profesional, Universidad Nacional Autonoma de Mexico.

Beard, D.C. and Weyl, P.K., 1973. Influence of texture on porosity and permeability of unconsolidated sand. *Bull., AAPG*, 57, 2, 349 – 369.

Bergman, D.J., 1978. The dielectric constant of a composite material – a problem in classical physics. *Phys. Reports*, 43, 377 – 407.

Berryman, J. G., 1995. Mixture theories for rock properties, in *Rock Physics and Phase Relations: A Handbook of Physical Constants*. T. J. Ahrens, ed., American Geophysical Union, Washington, D. C., 205-228.

Carothers, J.E., 1968. A statistical study of the formation factor relation. *The Log Analyst*, IX, Sept. – Oct.

Fricke, H., 1924. A mathematical treatment of the electric conductivity and capacity of disperse systems. *Phys. Rev*., 24, 575 – 587.

Gal, D., Dvorkin, J., and Nur, A., 1998. A physical model for the porosity reduction in sandstones. *Geophys*., 63, 454 – 459.

Gomez-Rivero, O., 1976. A practical method for determining cementation exponents and some other parameters as an aid in well log analysis. *The Log Analyst*, 27, 8 – 24.

Gueguen, Y., and Palciauskas V., 1994. *Introduction to the Physics of Rocks*. Princeton University Press, Princeton.

Herrick, D.C., 1988. Conductivity models, pore geometry, and conduction mechanisms. Ann. *SPWLA, 29th Ann. Log. Symp*., June, Paper D, 1-17.

Hashin, Z., and Shtrikman, S., 1962. A variational approach to the theory of effective magnetic permeability of multiphase materials. *J. Appl. Phys*., 33, 3125-3131.

Hoyer, W.A. and Spann, M.M., 1975. Comments on obtaining accurate electrical properties of cores. *Trans. SPWLA XVI*.

Klinkenberg, L.J., 1951. Analogy between diffusion and electrical conductivity in porous rocks. *Bull., GSA*, 62, 559 – 563.

Marion, D.P., 1990, Acoustical, Mechanical, and Transport Properties of Sediments and Granular Materials, Ph.D. thesis, Stanford University.

Mavko, G., and Nur, A., 1997. The effect of a percolation threshold in the Kozeny-Carman relation. *Geophys*., 1480 – 1482.

Mavko, G., Mukerji, T., and Dvorkin, J., 1998, *The Rock Physics Handbook: tools for seismic analysis in porous media*, Cambrige University Press.

Maxwell, J.C., 1960. Experiments on compaction and cementation of sand. *Rock deformation – A Symposium, Boulder, CO: Geological Society of America (GSA)*. Ed. D.T. Griggs. Ch. 5, 105 – 132.

Mendelson, K.S., and Cohen, M.H., 1982. The effect of grain anisotropy on the electrical properties of sedimentary rocks. *Geophys*., 47, 257 – 263.

Mendoza-Romero, G., and Perez-Rosales, C., 1985. New relationship between formation resistivity factor and primary and secondary porosities. *SPWLA, 26th Ann. Log. Symp*., June, 1-19.

Neustaedter, R.H., 1968. Log evaluation of deep Ellenberg gas zones. Paper SPE 2071, presented at *The Deep Drilling and Development Symposium – Deleware Basin of the SPE of AIME*, Monahans, Texas, Mar. 28.

Norris, A.N., Sheng, P., and Callegari, A.J., 1984. Effective-medium theories for two-phase dielectric media. *J. Appl. Phys*., 57, 1990 – 1996.

Nur, A., Mavko, G., Dvorkin, J., and Gal, D., 1995. Critical Porosity: The key to relating physical properties to porosity in rocks, in *Proc., 65th Ann. Int. Meeting, Soc. Expl. Geophys*., 878.

Parkhomenko, E. I., 1967, *Electrical Properties of Rocks*, Plenum Press, New York.

Perez-Rosales, C., 1982, On the Relationship Between Formation Resistivity Factor and Porosity, *Soc. Pet. Eng. J.*, 531-536.

Porter, C.R., and Carothers, J.E., Formation factor – porosity relation derived from well log data. *The Log Analyst*, Jan. – Feb., 16 – 26.

Rider, M.H., 1991. *The Geological Interpretation of Well Logs*; Revised Edition. Whittles Publishing.

Sanyal, S.K., Marsden, S.S., Jr., and Ramey, H.J., Jr., 1973. *The Log Analyst*, Mar. – Apr., 10 – 24.

Schlumberger, 1989, *Log Interpretation Principles/Applications*, Schlumberger Educational Services, Houston.

Sen, P.N., Scala, C., and Cohen, M.H., 1981. A self-similar model for sedimentary rocks with application to the dielectric constant of fused glass beads. *Geophys.*, V. 46, N. 5, 781 – 795.

Sethi, D.K., 1979. Some considerations about the formation resistivity factor – porosity relations. *Transactions of the SPWLA 20th Annual Logging Symposium*, Tulsa, Paper L.

Slawinski, A., 1926. Conductivilite d'un electrolyte contentant des spheres dielectriques, *J. Chim. Phys*., 23, 710 – 727.

Tiab, D. and Donladson, E. C., 1996, Petrophysics: Theory and Practice of Measuring Reservoir Rock and Fluid Transport Properties, Gulf Publishing Co., Houston Texas.

Waxman, M.H. and Smits, L.J.M., 1968. Electrical conductivities in oil-bearing shaly sands. *Soc. Pet. Engrs. J.*, 9, 107 – 122.

Winsauer, W.O., Shearin, H.M. Jr., Masson, P.H., and Williams, M., 1952. Resistivity of Brine-Saturated Sands in Relation to Pore Geometry. *Bull., AAPG*, 36, 2, 253-277.

Worthington, P.F., 1985. Evolution of shaley sand concepts in reservoir evaluation. *The Log Analyst*, 26, 23-40.

Wyllie, M.R.J., and Gardner, G.H.F, 1958. The generalized Koseny-Carman equation. *World Oil*, Mar.

Wyllie, M.R.J., and Gregory, A.R., 1953. Formation factors of unconsolidated porous media: Influence of particle shape and effect of cementation. *Trans. Am. Inst. Mech. Eng*., 198, 103-110.

Wyllie, M.R.J., and Rose, W.D., Some theoretical considerations related to the quantitative evaluation of the physical characteristics of reservoir rock from electrical log data. *Trans., AIME*, 189, 105 – 118.

Wyllie, M.R.J., and Spangler, M.B., 1952. Application of electrical resistivity measurements to problem of fluid flow in porous media. *Bull. AAPG*, 36, 359 – 403.

CHAPTER 5: Developments in the Electrical Resistivity – Acoustic Velocity Relationship

5.1 Introduction

Up until approximately 10 years ago, the use of seismic methods for environmental groundwater investigation had been nearly non-existent. The advantages of using seismic methods for delineating hydrostratigraphic units have been recently recognized by the environmental community and significant advances have been made in shallow seismic acquisition techniques and processing. Not only is the environmental community using compressional wave data more frequently, but also the geotechnical community is using surface and VSP shear wave data more frequently to study ground stability. Electrical resistivity techniques, on the other hand, have been used for decades to qualitatively interpret changes in fluid properties and locate clay-rich formations. For the most part, the environmental community *qualitatively* analyzes seismic and resistivity data *independently*.

As explained in Chapters 3 and 4, a system's percolation threshold ϕ_p and critical porosity ϕ_c together define three distinct porosity regions (Section 3.3.1), within which the formation resistivity factor – channel porosity and the moduli – total porosity relationships are defined. The porosities of most natural materials fall within the second porosity region (Region II), where $\phi_p \leq \phi \leq \phi_c$. In this region, the abilities for electrical currents and acoustic waves to be transmitted through the system are influenced by changes in various pore space characteristics, such as pore structure (amount, texture and content), grain contacts (shape, sorting and cement degree and type) and clays (amount, type and distribution). These pore space characteristics define the relationship between the channel porosity available for electrical flow and the total porosity through which a

seismic wave travels. Therefore, seismic and electrical techniques can be used jointly to constrain porosity, a required parameter for fluid flow modeling.

This chapter focuses on theoretically and empirically exploring the relationship between electrical resistivity and seismic velocity. The most significant contributions of this work are the development of resistivity – velocity bounds and insight into determining formation pore space characteristics using resistivity – velocity data. The real significance of these results, however, is the potential for using known relationships between resistivity and material properties to explain velocity trends and vice versa. Both the petroleum and environmental industries would benefit from these results because of the potential for using electrical logs to better constrain seismic interpretations and develop more accurate maps of flow properties.

5.2 Background

5.2.1 Theoretical Velocity Background

Elastic Properties

The compressional and shear velocities, V_p and V_s, at which an acoustic wave travels through an isotropic, homogeneous, elastic system, are functions of the system's bulk density ρ and elastic moduli K and μ (Mavko et al, 1998).

$$V_p = \left(\frac{K + \frac{4}{3}\mu}{\rho} \right)^{\frac{1}{2}} \tag{5.1}$$

$$V_s = \left(\frac{\mu}{\rho} \right)^{\frac{1}{2}} \tag{5.2}$$

The system's bulk density ρ is equal to the geometric mean of the individual constituent's densities ρ_i.

$$\rho = \sum_{i=1}^{N} f_i \rho_i \tag{5.3}$$

The system's effective bulk K and shear μ moduli are controlled by the system's pore space characteristics and the individual constituent's elastic properties and volume fractions. Most mineral constituents (excluding clay) are stiff and rigid, whereas clays and fluids (gas and/or liquid) are compressible (low K) and lack rigidity ($\mu = 0$) (Table 5.1). Because the moduli of minerals and fluids are so different, the amount of pore-filling fluid ϕ strongly influences the system's effective moduli and velocities. Changes in a system's pore space characteristics can cause changes in the constituent volume fractions and the type and number of granular contacts, thus changing the system's effective elastic moduli and density.

A system's Poisson's ratio ν is a function of the system's effective bulk and shear moduli, not of the density.

$$\nu = \frac{3K - 2\mu}{2(3K + \mu)} = \frac{V_p^2 - 2V_s^2}{2(V_p^2 - V_s^2)} \tag{5.4}$$

where $-1 \leq \nu \leq 0.5$. In fluids, $\nu = 0.5$ since $\mu = 0$ GPa. Therefore, materials with Poisson's ratios near 0.5 have fluid-like behavior. ν characterizes the ability for a composite to deform horizontally when compressed vertically. Most natural composites expand horizontally (positive ν) under vertical compression, as opposed to contracting (negative ν); therefore, it is safe to assume ν is between 0 and 0.5 in rocks and sediments (Table 5.1). ν is high in unconsolidated systems, regardless of the mineral constituents since the grains move freely when compressed; however, in cemented systems, ν depends on the system's mineral moduli and porosity.

Constituent	K (GPa)	μ (GPa)	ρ (g/cc)	V_p (km/s)	V_s (km/s)	ν
water	2.2	0	1	1.48	0	0.5
quartz	36.5 – 37.9	44.0 – 45.6	2.65	6.04 – 6.06	4.09 – 4.15	0.06 – 0.08
calcite	63.7 – 76.8	28.4 – 32.0	2.70 – 2.71	6.26 – 6.64	3.24 – 3.44	0.29 – 0.32
clay	1.5 – 25.0	1.4 – 9.0	1.58 – 2.60	1.44 – 4.32	0.93 – 2.54	0.14 – 0.35

Table 5.1: Elastic moduli and density of a few common constituents. Values from Mavko et al (1998).

Hashin-Shtrikman Bounds

The Hashin-Shtrikman (HS) bounds (Hashin and Shtrikman, 1963) are the narrowest theoretical moduli - porosity bounds that don't take the geometry of each constituent into account. For a two-constituent system, the bounds on bulk $K_{HS\pm}$ and shear $\mu_{HS\pm}$ moduli are

$$K_{HS\pm} = K_1 + \frac{f_2}{(K_2 - K_1)^{-1} + f_1(K_1 + \frac{4}{3}\mu_1)^{-1}} \tag{5.5}$$

$$\mu_{HS\pm} = \mu_1 + \frac{f_2}{(\mu_2 - \mu_1)^{-1} + \frac{2f_1(K_1+2\mu_1)}{5\mu_1(K_1+\frac{4}{3}\mu_1)}} \tag{5.6}$$

where f is the constituent fraction (Mavko et al, 1998). In a fluid – mineral system, the fraction of the fluid is equal to the total porosity ϕ and the fraction of the mineral is (1-ϕ). The upper bounds are typically found when the mineral is the first constituent and the fluid is the second, whereas the lower bounds are typically found when the fluid is the first constituent and the mineral is the second. The velocity – porosity bounds and Poisson's ratio – porosity bounds are found by evaluating Eqns. 5.5 & 5.6 at specific porosities and plugging the results into Eqns. 5.1 – 5.4, respectively. The bounds are wide when the constituent moduli are significantly different, such as a quartz – water system, and tight when the constituent moduli are similar, such as a clay – water system (Figure 5.1).

The upper HS bound corresponds to isolated soft spheres (pores) covered by a stiff and rigid shell (mineral), a likely scenario in pumice and some basalts, but an unlikely one for granular materials. The lower HS bound corresponds to isolated stiff and rigid spheres (mineral) covered by a soft shell (water and/or clay), a more likely model for sediments. This is schematically shown in Figure 5.1; the black regions represent the stiff constituent and the white region the compliant one. Like the resistivity lower HS bound, the elastic lower HS bounds are controlled by the fluid constituent, not the mineral constituent, therefore the lower bounds are nearly the same for clays and quartz systems.

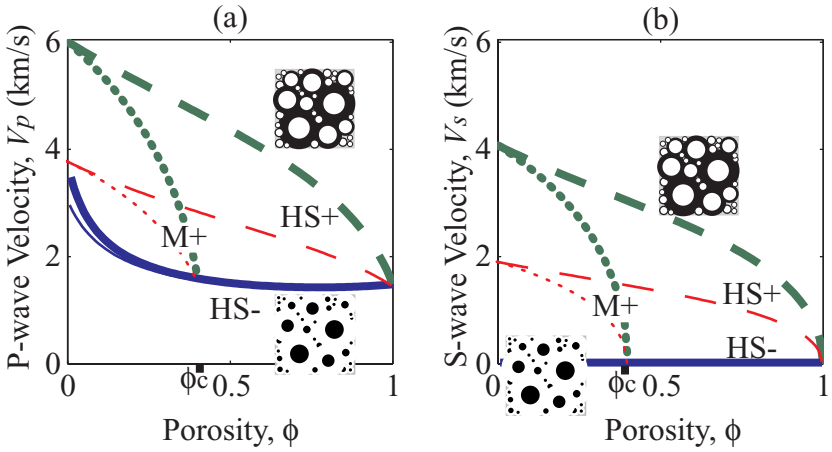

Figure 5.1: Upper and lower HS bounds for P-wave velocity V_p and S-wave velocity V_s. The upper (dashed lines) and lower (solid lines) HS bounds are found for two different saturated, two-constituent systems where the fluid constituent is water (K_w = 2.2 GPa, μ_w = 0 GPa, and ρ_w = 1 g/cc) and the mineral constituent is (1) quartz (K_{qz} = 37.0 GPa, μ_{qz} = 44.0 GPa, and ρ_{qz} = 2.65 g/cc) and (2) clay (K_{cl} = 25 GPa, μ_{cl} = 9 GPa, and ρ_{cl} = 2.55 g/cc). Also shown are empirical upper bounds (dotted lines) evaluated between $0 \le \phi \le \phi_c$; ϕ_c = 0.40. The black regions in the schematic packs represent the rigid and stiff constituent and the white represents the compressible and compliant one.

5.2.2 Empirical Velocity Background

Empirical Upper Moduli – Porosity Bounds

In granular materials, there is a critical porosity ϕ_c (discussed in Section 3.2.1) that separates both the mechanical and acoustical behaviors into two distinct domains (Nur et al, 1995). At $\phi < \phi_c$ the grain-supported material is rigid and stiff, whereas at $\phi > \phi_c$ the fluid-supported material is compliant and is highly compressible. Velocity – porosity data converge near the lower HS bound evaluated at the formation's ϕ_c. Nur et al (1995) defined empirical upper $K - \phi$ and $\mu - \phi$ bounds that are tighter than the upper HS bound by a line that connects the points (0, K_m) and (ϕ_c, K^*_{HS-}) and the points (0, μ_m) and (ϕ_c, μ^*_{HS-}), respectively. The first point corresponds to the mineral moduli (K_m and μ_m) when the mineral fraction is 100% ($\phi = 0$); the second point corresponds to the lower HS bound (K^*_{HS-} and μ^*_{HS-}) evaluated at the critical porosity ϕ_c. In a two-constituent fluid-mineral

system, the upper moduli bounds M_+ (Mavko et al, 1998) for the bulk and shear modulus are defined by

$$M_+ = \left(1 - \frac{\phi}{\phi_c}\right) M_m^* + \frac{\phi}{\phi_c} M_{HS-}^* \qquad (5.7)$$

where M_m^* is the mineral modulus and M_{HS-}^* is the modulus of the HS lower bound evaluate at the system's critical porosity. Eqn. 5.7 is essentially the Voigt upper bound of the modulus for porosities normalized by the critical porosity. Empirical upper bounds on $V_p - \phi$ and $V_s - \phi$ can be created using the empirical upper K_+ and μ_+ bounds (Figures 5.1). Since V_p and V_s are functions of the square root of the moduli, the upper bounds aren't linear on velocity – porosity plots.

Influence of Pore Space Characteristics on P-wave Velocity and Porosity

A formation's stiffness, rigidity, density and porosity can all change from changes in pore space characteristics (i.e. cementation, compaction, sorting, clay volume, and fluid saturation). The influences of pore space characteristics on total and channel porosities are discussed in Section 3.3.3. The influences of evolution of a formation's pore space on electrical resistivity - porosity data were discussed in Section 4.3.2. As shown in Figure 5.2, the observed influences on P-wave velocity – porosity data are quite similar; i.e. sorting influences the seismic response less than cementation does. Each pore space characteristic has a different effect on porosity and elastic moduli, therefore the location of P-wave velocity – porosity data with respect to the upper and lower bounds can provide insight into the formation's pore space characteristics (Figure 5.2). Since V_s data is collected less commonly than V_p data, the observed influences of pore space characteristics on V_s and ν are not as well known, therefore not discussed.

$V_p - \phi$ data values of loose, unconsolidated materials tend to fall along lower HS bounds (Figure 3) as a result of changes in sorting (Avseth et al, 1998). $V_p - \phi$ data values in rock and artificially consolidated materials plot near the empirical upper bound defined by Nur (1995) as a result of increased cementation (Dvorkin and Nur, 1996). Increased compaction (Mindlin, 1949) results in increased V_p and decreased ϕ. V_p increases and ϕ

decreases when dispersed clay (Han, 1986) is added to a sand matrix, whereas V_p decreases and ϕ increases when dispersed clay is added to a clay matrix (Marion, 1990). For a given formation, the velocity is higher if it is fully saturated than if it is partially saturated; the degree of influence is controlled by the pore-filling fluid properties and the distribution, uniform (Gassmann, 1951) or patchy (Hill, 1963).

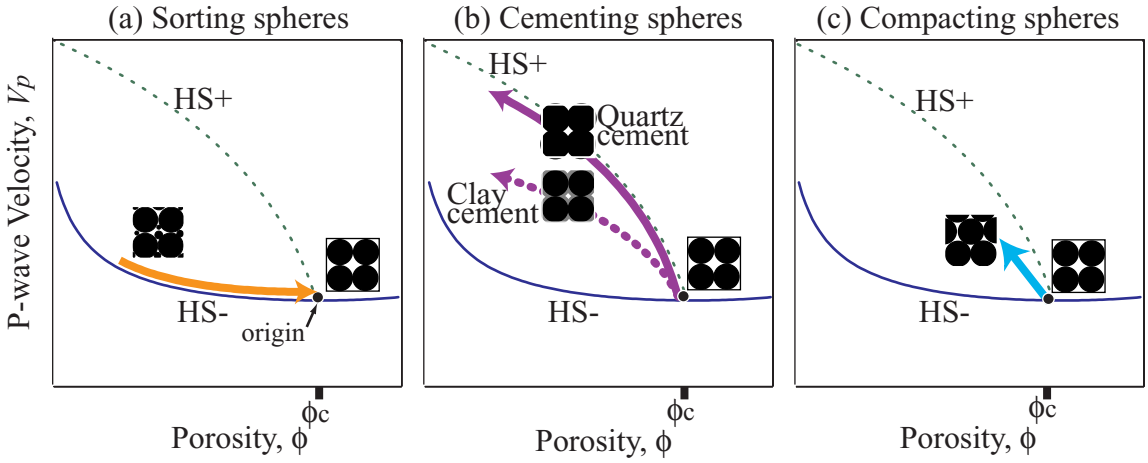

Figure 5.2: Schematic of the influence of pore space characteristics on V_p and ϕ. The arrows indicate direction of increased change in material property and the slopes indicate the degree of influence on V_p and ϕ. The solid lines are the upper and lower HS bounds and the dashed lines are the empirical upper bounds; $\phi_c = 0.40$.

5.3 New Developments on the Electrical Resistivity – Acoustic Velocity Relationship

5.3.1 New Concept of Creating Resistivity –Velocity Bounds

A formation's characteristic P-wave velocity V_p, S-wave velocity V_s, and normalized resistivity R/R_w increase with decreasing total porosity ϕ (Figures 5.1 a and b). For suspended granular systems ($\phi > \phi_c$), the $R/R_w - V$ relationships are all simply defined by the lower HS bounds for resistivity and moduli (Eqns. 4.2, 5.5 and 5.6; Figures 4.1 and 5.1). For grain-supported systems ($\phi < \phi_c$), the $R/R_w - V$ relationships are confined by upper and lower resistivity – moduli bounds (Figure 5.3). The $R/R_w - V_p$ bounds are

created by combining the lower HS bounds (Eqns. 4.2, 5.5 and 5.6) and the empirical upper bounds (Eqns. 4.20 and 5.7) for R and the moduli at equal porosities. The same concept can be used to create $V_s - \phi$ bounds (Figure 5.3 b). The following parameters need to be specified to create the bounds: each constituent's R, K, μ, and ρ and the system's porosity limits ϕ_p and ϕ_c.

The lines in Figure 5.3 are example bounds for a quartz-water system. The bold solid line results from combining the lower HS R/R_w and V_p bounds; the bold dotted line results from combining the empirical upper R/R_w and V_p bounds; the dashed lines result from combining the empirical upper R/R_w bound with the lower HS V_p bound and vice versa. Strictly speaking, $R/R_w - V_p$ data can fall anywhere between the dashed lines, however, these lines correspond to the special case of a material property influencing V_p and without influencing R at a given porosity and vice versa. Values along the bounds in Figure 5.3 represent porosity values in 0.1 increments: from 0% porosity at the upper limit and 100% porosity at the lower limit.

A significant observation in Figure 5.3a is that the upper and lower $R/R_w - V_p$ bound are very similar. If the elastic and electrical properties of a formation change in a similar manner from a change in porosity, then $R/R_w - V_p$ data is restricted to the narrow region between the bounds. If an $R/R_w - V_p$ data pair plots within the region between the upper and lower $R/R_w - \phi$ bounds (solid and dotted lines in Figure 5.3a), then the formation properties are electrically and elastically similar. However, if the elastic properties change without the electrical properties changing in a similar way, the $R/R_w - V_p$ data pair will plot outside the inner-most bounds, but still between the upper-lower bounds (dashed lines in Figure 5.3a).

The range in $R/R_w - V_p$ value pairs at a given porosity is restricted to the region defined by the box in Figure 5.4. The range in possible $R/R_w - V_p$ data pairs is narrow at porosities near ϕ_c since the bounds converge at ϕ_c. The $R/R_w - V_p$ data pairs are not uniquely defined for a given porosity; the range $R/R_w - V_p$ data defined by the box in Figure 5.4 can occur at porosities between ϕ_{min} and ϕ_{max}.

Even though an $R/R_w - V_p$ data pair plots as a single point on a $R/R_w - V_p$ plot, it is not defined uniquely by porosity; the data pair represents a range in possible porosities (Figure 5.5). For a given $R/R_w - V_p$ data pair, the porosity range is improved if the range limits are different for the $R - \phi$ bounds and the $V_p - \phi$ bounds.

A significant observation in Figure 5.5c is that the upper and lower $R/R_w - V_p$ bound are very similar. This means that the resistivity and velocity bounds have similar functional form. If the elastic and electrical properties of a formation change in a similar manner from a change in porosity, then $R/R_w - V_p$ data is restricted to the narrow region between the bounds. If an $R/R_w - V_p$ data pair plots within the region between the upper and lower $R/R_w - \phi$ bounds (solid and dotted lines in Figure 5.5c), then the formation properties are electrically and elastically similar. However, if the elastic properties change without the electrical properties changing in a similar way, the $R/R_w - V_p$ data pair will plot outside the inner-most bounds, but still between the upper-lower bounds (dashed lines in Figure 5.5c).

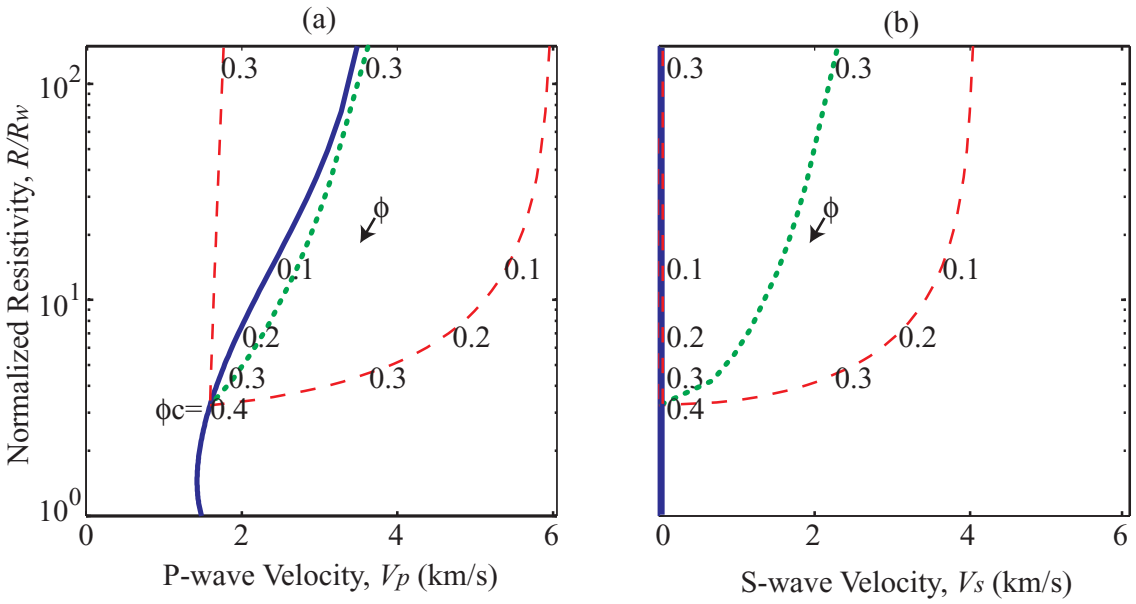

Figure 5.3: Bounds on the velocity – normalized resistivity. Upper and lower bounds in a water – quartz sand system for (a) $V_p - R/R_w$ and (b) $V_s - R/R_w$. The lower HS bound (solid lines), the empirical upper bound (dotted lines), the upper empirical and lower HS bounds (dashed lines); $\phi_c = 0.40$.

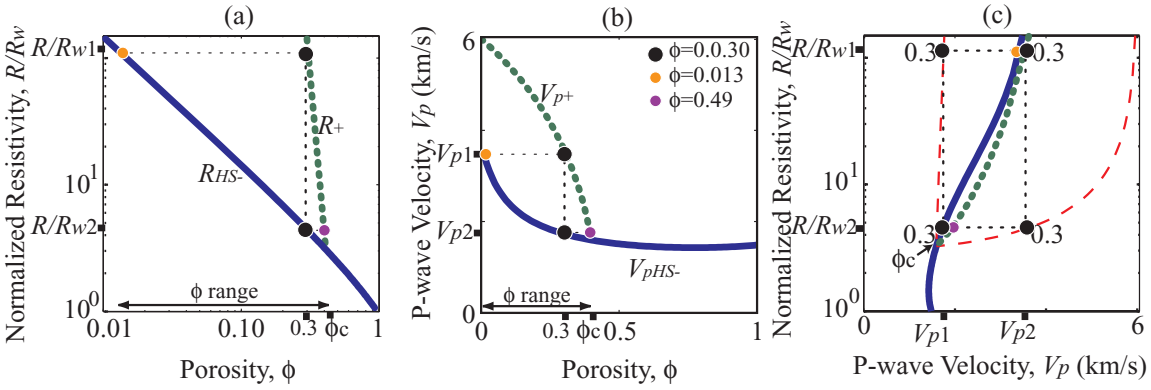

Figure 5.4: Constraining velocity – resistivity pairs using porosity data. Constraining porosity estimates using velocity – resistivity data. $\phi_c = 0.40$

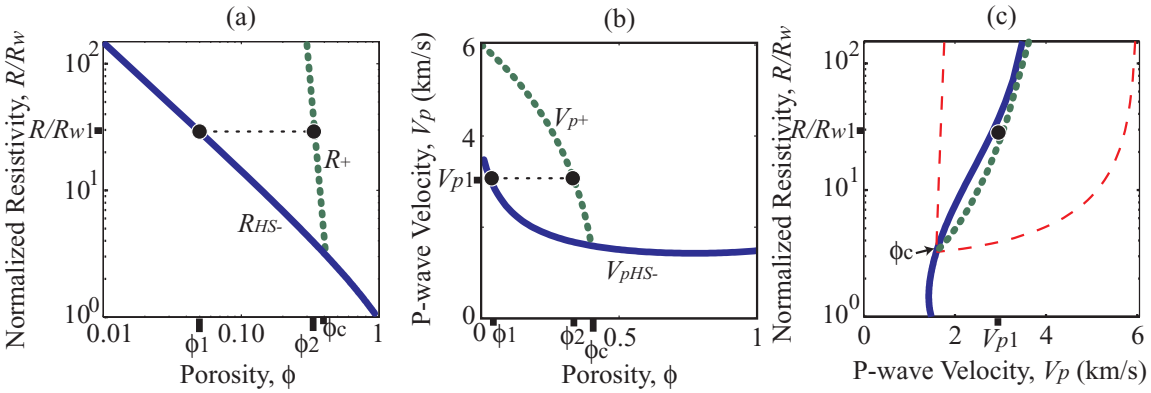

Figure 5.5: Constraining porosity estimates using velocity – resistivity data. $\phi_c = 0.40$

5.3.2 Evaluating Pore Space Characteristics using Velocity - Resistivity Data

Increasing the compaction, cementation, sorting or clay content in a formation increases both R and V_p and decreases porosity (Section 3.3.2 and 4.2.2). Trends in data on an $R/R_w - V_p$ plot differ because of changes in the pore space characteristics and/or the mineral constituents, which may or may not influence the pore space. Since electrical currents and acoustic waves are both influenced by similar pore space characteristics, location of data on an $R/R_w - V_p$ plot can be used to (1) identify changes in a formation's

properties and (2) delineate individual formations with different characteristic properties. Because the $R/R_w - V_p$ bounds are so narrow, it could be difficult to distinguish different formation properties (Figure 5.6a); however, since the $R/R_w - V_s$ bounds (Figure 5.6b) are wide, $R/R_w - V_s$ data might provide more insight into the formation pore space characteristics.

Strictly speaking, the upper and lower bounds are defined for a specific fluid-mineral system. However, R/R_w and V_p values in a particular formation can vary from changes in the volumes of mineral constituents as well as changes in pore space characteristics. For example, in a quartz sand system, the HS and empirical upper bound is lower for a clay-cemented system than a quartz-cemented one since $R_{cl} < R_{qz}$, $V_{p\text{-}cl} < V_{p\text{-}qz}$ and $\phi_{c\text{-}cl} > \phi_{c\text{-}qz\text{-}sa}$. The influence of mineral constituents is particularly important to understand when interpreting the location of $R/R_w - \phi$ and $V_p - \phi$ data with respect to the bounds since the bounds themselves must be adjusted for changes in mineralogy.

By adding a cementing mineral with similar electrical and elastic properties as the granular constituent, the system's stiffness increases and porosity decreases resulting in increased in V_p and R. Such cemented data tend to plot near the empirical upper $R/R_w - \phi$ and $V_p - \phi$ bounds, therefore plot near the upper $R/R_w - V_p$ bound (dotted line in Figure 5.6a).

The lower HS bounds on R/R_w and V_p characterize systems of resistive and stiff spheres in suspension, respectively, a likely model for many sediments. Consequently, data in clean sands and spheres fall on the lower HS R/R_w and V_p bounds when in suspension and just above when loosely packed. Therefore, data that plot near the lower HS bounds (bold dashed line in Figure 5.6a) are likely from unconsolidated and uncompacted sediments.

If the system's mineralogy doesn't change, decreasing the sorting (increasing the grain size distribution) decreases porosity and slightly increases the system's stiffness and tortuosity, leading to a slight increase in V_p and R. $R/R_w - V_p$ data should plot up the lower HS bound as a result of decreased sorting. In many clastic depositional

environments, however, sorting decreases from increasing clay content; the influence of sorting in such a case is the same as the clay influence.

The effects of clays on R and V_p are quite complex because of the unique electrical, elastic and pore space properties of clays. The influence of clays on the R and V_p of a system depends on the distribution of clays (dispersed, structural or cementing), the method of adding the clays to the system (replacing pore space or grains), the properties of the other constituents (R_w, K_m and μ_m), and the compaction history. For example, consider the case where dispersed clays are added to the pore space of brine-saturated sand. In such a case, total porosity decreases because it is replaced by the clay volume. R increases because the channel porosity decreases and the tortuosity effect dominates over the conductivity effect. V_p also increases because the clays stiffen the pore space.

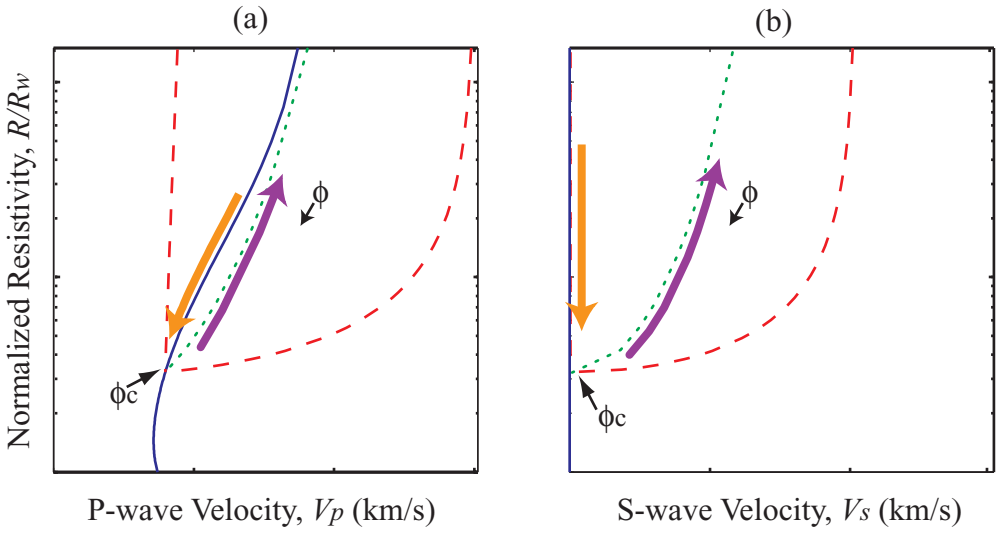

Figure 5.6: Using the velocity – resistivity bounds to evaluate formation properties. The arrows indicate the direction of increased change in pore space characteristic.

5.4 Conclusions

- For materials in suspension ($\phi > \phi_c$), the $R/R_w - V_p$ relationship is simply defined by the lower HS bounds on R and V_p.

- For grain-supported materials ($\phi < \phi_c$), the $R/R_w - V_p$ relationship is constrained by $R/R_w - V_p$ bounds, which are defined by the lower HS bounds for R and V_p and modified upper bounds for R/R_w and V_p.

- $R/R_w - V_p$ data in unconsolidated systems fall along the lower HS $R/R_w - V_p$ bound.

- $R/R_w - V_p$ data in cemented systems fall along the empirical upper $R/R_w - V_p$ bound.

- The $R/R_w - V_p$ bounds can be used to (1) constrain porosity estimates given $R/R_w - V_p$ data, (2) forward model $R/R_w - V_p$ data pairs given ϕ data.

- The trends of $R/R_w - V_s$ data with respect to the bounds may provide insight into changes in a formation's pore space characteristics.

5.5 References

Avseth, P., Mavko, G, Dvorkin, J., and Rykkje, Johannes, 1998. The effects of sorting on the rock physics properties of sands. *Stanford Rock Physics & Borehole Geophysics Project: Annual Report*, 68, Paper A3, 1-7.

Dvorkin, J., and Nur, A., 1996. Elasticity of high-porosity sandstones: Theory for two North Sea datasets. *Geophys*., 61, 1363-1370.

Han, D.H., 1986. *Effects of Porosity and Clay Content on Acoustic Properties of Sandstones and Unconsolidated Sediments*. Ph.D. dissertation, Stanford University.

Hashin, Z., and Shtrikman, S., 1963. A variational approach to the theory of the elastic behavior of multiphase materials. *J. Mech. Phys. Solids*, 11, 127-140.

Mavko, G., Mukerji, T., and Dvorkin, J., 1998, *The Rock Physics Handbook: tools for seismic analysis in porous media*, Cambrige University Press.

Mindlin, R.D., 1949. Compliance of elastic bodies in contact. *J. Appl. Mech.*, 16, 259-268.

Nur, A., Mavko, G., Dvorkin, J., and Gal, D., 1995. Critical Porosity: The key to relating physical properties to porosity in rocks, in *Proc., 65th Ann. Int. Meeting, Soc. Expl. Geophys*., 878.